IOWA STATE UNIVERSITY
Digital Repository

Graduate Theses and Dissertations

Iowa State University Capstones, Theses and Dissertations

2015

A new formulation for delayed detached eddy simulation based on the Smagorinsky LES model

Karthik Rudra Reddy
Iowa State University

Follow this and additional works at: https://lib.dr.iastate.edu/etd

Part of the Aerospace Engineering Commons

Recommended Citation

Rudra Reddy, Karthik, "A new formulation for delayed detached eddy simulation based on the Smagorinsky LES model" (2015). *Graduate Theses and Dissertations*. 14505.
https://lib.dr.iastate.edu/etd/14505

This Dissertation is brought to you for free and open access by the Iowa State University Capstones, Theses and Dissertations at Iowa State University Digital Repository. It has been accepted for inclusion in Graduate Theses and Dissertations by an authorized administrator of Iowa State University Digital Repository. For more information, please contact digirep@iastate.edu.

A new formulation for delayed detached eddy simulation based on the Smagorinsky LES model

by

Karthik Rudra Reddy

A dissertation submitted to the graduate faculty
in partial fulfillment of the requirements for the degree of
DOCTOR OF PHILOSOPHY

Major: Aerospace Engineering

Program of Study Committee:
Paul Durbin, Major Professor
Alric Rothmayer
Anupam Sharma
Shankar Subramaniam
James Hill

Iowa State University
Ames, Iowa
2015

Copyright © Karthik Rudra Reddy, 2015. All rights reserved.

DEDICATION

To my parents Vijayalakshmi and Rudra Reddy,
my sister Gayathri, and my wife Rajalakshmi.

TABLE OF CONTENTS

LIST OF TABLES vi

LIST OF FIGURES vii

ACKNOWLEDGEMENTS x

ABSTRACT xi

CHAPTER 1. INTRODUCTION 1

  1.1 Background 1

    1.1.1 Motivation for hybrid RANS/LES methods 1

    1.1.2 Detached eddy simulation 2

  1.2 Governing Equations 11

    1.2.1 Conservation equations 11

    1.2.2 Turbulence model description 13

  1.3 Numerical Modeling 16

    1.3.1 Spatial discretization 18

    1.3.2 Temporal discretization 21

    1.3.3 The pressure equation 22

CHAPTER 2. A DDES MODEL WITH A SMAGORINSKY-TYPE EDDY VISCOSITY FORMULATION AND LOG-LAYER MISMATCH CORRECTION 26

  2.1 Introduction 26

  2.2 Model Formulation 28

  2.3 Test Cases 34

    2.3.1 Channel flow 34

2.3.2 Flow over backward facing step 38

2.3.3 Flow over 2D periodic hills 42

2.3.4 Flow through an air blast atomizer 44

2.4 Conclusion 49

2.5 Acknowledgements 49

CHAPTER 3. AN $\ell^2\omega$ FORMULATION OF DELAYED DETACHED EDDY SIMULATION 50

3.1 Introduction 50

3.2 Model Formulation 52

3.3 Test Cases 54

3.3.1 Channel flow 54

3.3.2 Flow over a backward facing step 54

3.3.3 Flow over 2D periodic hills 55

3.3.4 Flow through an air blast atomizer 56

3.4 Implementation of Dynamic Procedure 58

3.4.1 Model formulation 60

3.4.2 Test case - flow through a 3D diffuser 62

3.5 Conclusions 64

3.6 Acknowledgments 65

CHAPTER 4. ON THE DYNAMIC COMPUTATION OF THE MODEL CONSTANT IN DELAYED DETACHED EDDY SIMULATION 66

4.1 Introduction 66

4.2 Model Formulation 68

4.3 Test Cases 74

4.3.1 Channel flow 74

4.3.2 Backward facing step 76

4.3.3 Periodic hills 78

4.3.4 3D diffuser 79

للاستشارات المنارة

4.3.5 Rotating channel 81
4.3.6 Fundamental aero investigates the hill (FAITH) geometry 84
4.4 Conclusion 87
4.5 Acknowledgements 87
CHAPTER 5. CONCLUSION 88
5.1 Summary of Results 88
5.2 Prospects for Future Work 93
APPENDIX A. DERIVATION OF THE MEAN AND TURBULENT KINETIC ENERGY EQUATIONS 95
BIBLIOGRAPHY 98

LIST OF TABLES

Table 2.1 Measured mass flow rates for PIV and CFD simulations. 47

Table 3.1 Measured mass flow rates for PIV and CFD simulations. 57

Table 4.1 Grid resolution for channel flow cases with different Reynolds numbers 74

Table 4.2 Predicted Re_τ for different Ro values. 83

LIST OF FIGURES

Figure 1.1 Flow over a circular cylinder using SA-URANS 4

Figure 1.2 Flow over a circular cylinder using SA-DES 4

Figure 1.3 Instantaneous vorticity magnitude using SA-URANS 5

Figure 1.4 Instantaneous vorticity magnitude using SA-DES 6

Figure 1.5 Flow over a delta wing 7

Figure 1.6 U^+ vs. y^+ from DES of channel flow 10

Figure 2.1 Distribution of C_f for flat plate 33

Figure 2.2 Comparison of shielding function for different models 34

Figure 2.3 Channel flow: effect of C_{DES} 35

Figure 2.4 Channel flow: U^+ and shear stress profiles. 36

Figure 2.5 Channel flow: U^+ profiles at different Re_τ 37

Figure 2.6 Channel flow: vorticity contours along XZ plane 38

Figure 2.7 Channel flow: ${u'}^+$, ${v'}^+$ and ${w'}^+$ profiles 38

Figure 2.8 Comparison of production and dissipation limited DDES 39

Figure 2.9 Backward facing step: contours 39

Figure 2.10 Backward facing step: velocity profiles 40

Figure 2.11 Backward facing step: $k - \omega$ SST based DDES 40

Figure 2.12 2D periodic hills: velocity profiles 43

Figure 2.13 Atomizer: geometry 43

Figure 2.14 Atomizer: contour of f_d . . . 44

Figure 2.15 Atomizer: iso-surface of Q . . . 45

Figure 2.16 Atomizer: Q contours from RANS . . . 46

Figure 2.17 Atomizer: velocity contours along the axial plane . . . 46

Figure 2.18 Atomizer: velocity contours along a radial plane . . . 47

Figure 2.19 Atomizer: velocity profiles along a radial plane . . . 48

Figure 3.1 Channel flow: U^+ and shear stress profiles. . . . 54

Figure 3.2 Backward facing step: Iso-surface of Q . . . 55

Figure 3.3 Backward facing step: C_f distribution . . . 55

Figure 3.4 2D periodic hills: C_f distribution . . . 56

Figure 3.5 Atomizer: Iso-surface of Q . . . 57

Figure 3.6 Atomizer: velocity contours along the axial plane . . . 58

Figure 3.7 Atomizer: velocity contours along a radial plane . . . 58

Figure 3.8 Atomizer: velocity profiles along a radial plane . . . 59

Figure 3.9 Dynamic DDES with no check for mesh quality . . . 61

Figure 3.10 3D diffuser: velocity contours . . . 62

Figure 3.11 3D diffuser: velocity profiles from DDES . . . 63

Figure 3.12 3D diffuser: velocity profiles from dynamic DDES . . . 64

Figure 4.1 Dynamic DDES on a coarse grid . . . 70

Figure 4.2 Dynamic DDES with no check for mesh quality . . . 71

Figure 4.3 Dynamic DDES: limiting function . . . 73

Figure 4.4 Channel flow: U^+ profiles at different Re_τ . . . 75

Figure 4.5 Channel flow: comparison of DDES and dynamic DDES. . . . 76

Figure 4.6 Backward facing step: dynamic DDES results 77

Figure 4.7 Backward facing step: C_{lim} contours 78

Figure 4.8 2D periodic hills: dynamic DDES results 79

Figure 4.9 3D diffuser: velocity contours 80

Figure 4.10 3D diffuser: velocity profiles from DDES 81

Figure 4.11 3D diffuser: velocity profiles from dynamic DDES 81

Figure 4.12 Rotating channel: velocity profiles at different Ro 82

Figure 4.13 FAITH: C_f contours and velocity profiles 85

Figure 4.14 FAITH: contours of velocity, k, u_{rms} and $\overline{u'v'}$ 85

Figure 4.15 FAITH: contours of k_m, k_r, f_d and C_{DES} 86

Figure 5.1 Comparison of production and dissipation limited DDES 89

Figure 5.2 Dynamic DDES with no check for mesh quality 90

Figure 5.3 3D diffuser: velocity profiles from DDES 90

Figure 5.4 3D diffuser: velocity profiles from dynamic DDES 90

Figure 5.5 Channel flow: U^+ profiles at different Re_τ 91

Figure 5.6 Channel flow: comparison of DDES and dynamic DDES 92

Figure 5.7 Rotating channel: velocity profiles at different Ro 92

ACKNOWLEDGEMENTS

My heartfelt thanks to Dr. Paul Durbin for guiding me these past three years. His insights and approach to research have been a source of inspiration, and I feel honored to have learnt from him.

I would also like to thank Dr. Alric Rothmayer, Dr. Anupam Sharma, Dr. James Hill and Dr. Shankar Subramaniam for kindly serving on the POS Committee. Special thanks to Dr. Alberto Passalacqua for the discussions I had with him regarding OpenFOAM.

The financial support from NASA Grant NNX12AJ74A and Pratt & Whitney is gratefully acknowledged, without which my PhD dreams would've never materialized.

The learning curve I experienced with OpenFOAM would've been steeper if it weren't for Sunil. I've had several discussions with him regarding the code, which definitely saved me a lot of time. Special thanks to Elbert and Varun — I learnt a lot from the many technical and not-so-technical discussions we've had. I'd also like to thank my colleagues Xuan, Zifei, Rikhi, Farid and Umair, who've shared conversations and office space with me over the past three years.

My time in Ames and at Iowa State University has been quite pleasant, thanks to my friends Kannan, Suganthi, Subbu, Avinaash, Monalisa, Bharat and everyone else. I've also had many memorable trips with my friends from Georgia Tech — Manu, Aditya, Sangeetha, Ravi, Mahaadevi, Deepa, Vidisha, Ketaki, Apurva, Preethi, Ranjini and so many others — I'll never forget our time together, and how much fun we had.

Finally, my pillars of support — my family. Words won't suffice to acknowledge their role. To my parents and sister, for their constant encouragement and motivation which was instrumental in my decision to pursue a PhD, and to my wife, for her support, patience, and faith in me — thank you.

ABSTRACT

This dissertation describes an alternate formulation for Delayed Detached Eddy Simulation or DDES. Detached Eddy Simulation (DES) falls under the category of hybrid RANS/LES models where a single turbulence model functions as either a RANS (Reynolds-Averaged Navier-Stokes) or an LES (Large Eddy Simulation) model. Certain fundamental issues were identified in the original DES formulation, which led to revised formulations such as the Delayed DES (DDES) and Improved DDES (IDDES) with increasing complexity, which negatively impacted the readability of the model.

This is the motivation to explore an alternate formulation for DES which aims to correct the issues found in the original DES, while at the same time being simple and easy to understand. Towards this end, the eddy viscosity formulation in a given RANS model is modified such that it mimics the Smagorinsky LES subgrid viscosity expression when the model is in eddy simulation mode. The resemblance of the resulting DES formulation to the Smagorinsky model allows the implementation of a dynamic procedure to compute the model constant, similar to the dynamic Smagorinsky model. This was found to improve the model performance in several cases. The description of this alternate DES formulation and the implementation of a dynamic procedure in this model will be the major focus of this dissertation.

CHAPTER 1. INTRODUCTION

1.1 Background

1.1.1 Motivation for hybrid RANS/LES methods

Turbulence is commonly encountered in practical fluid flows. It results in much larger skin friction, heat transfer rates and species mixing, compared to laminar flows, which makes accurate prediction of turbulent flows practically important. Hence, turbulence modeling is an inevitable portion of any Computational Fluid Dynamics (CFD) code which hopes to simulate any real-world geometry.

A common view of turbulent flows is that they consist of a range of scales, with the size of the large scales determined by the geometry, and the size of the small scales determined by the fluid viscosity. The broad range of spatial and temporal scales observed in a turbulent flow make it impossible to capture the details of all those scales. Resolving the smallest scales would require very small cell spacing and time steps. This led to the idea of resolving only a certain range of scales, typically the larger ones, while modeling the effect of the smaller scales. Two of the most popular turbulence modeling approaches are Large Eddy Simulation (LES) and Reynolds-Averaged Navier Stokes (RANS) methods.

The LES method models only the smallest scales while resolving all the larger scales. Hence, in general, it is able to produce accurate results for a wide range of flow configurations. However, as the Reynolds number *Re* of the flow increases, the range of scales to be resolved also increases. This leads to increased computational cost when using LES models for high *Re* flows, which is usually the case for practical engineering configurations. The computational resources required to simulate such a flow using an LES model are prohibitive (Spalart (2000)).

RANS methods on the other hand capture only the mean flow (or sometimes only the largest scales) while modeling the effect of all the fluctuations. Since a much larger portion of the scales are now being modeled, this leads to a larger error in the computed solution (in general). RANS models are usually calibrated based on attached flows such as flow over a flat plate or channel flow, and hence they work well for such cases. However, for cases involving a separation region, they may be inaccurate (Spalart (2000); Hunt (1990)).

The computational expense of LES and the inaccuracies of RANS for more complex flows motivated the development of hybrid RANS/LES methods. In wall bounded flows, much of the expense of LES arises due to a requirement for small cell spacing in the boundary layer. Hence the idea of using a RANS method to compute the attached boundary layer region and an LES method to compute the flow past the separation point is an attractive proposition cost-wise. Hybrid models are relatively new in the field of turbulence modeling, and have garnered the interest of many researchers.

1.1.2 Detached eddy simulation

Hybrid RANS/LES methods can be broadly classified into 2 categories: zonal and non-zonal. Possibly the most obvious approach of concocting a hybrid model is to take a RANS model, and an LES model, and use them simultaneously in separate, user-defined regions within the flow domain - this is the zonal approach. A concern with such in approach is the interface between the RANS and LES regions, where some kind of interpolation needs to be used in order to provide seamless transition between the 2 regions, and is the focus of several investigations (Schluter et al. (2004); Batten et al. (2004)). Another, more obvious, concern lies in the determination, by the user, of which regions should be simulated with RANS or LES methods. This process is likely to be error-prone and based on a trial-and-error approach, especially for complex geometries.

The non-zonal approach, as the name suggests, is one where the user is not required to specify the RANS and LES regions. One of the most popular non-zonal hybrid RANS/LES methods is Detached Eddy Simulation (DES), which was first proposed by Spalart et al. (1997). The original DES formulation was based on the Spalart-Allmaras (SA) RANS model (Spalart and Allmaras (1994)) and it introduced a modified length scale definition

$$\tilde{d} = \min(d, C_{DES}\Delta), \tag{1.1}$$

where

$$\begin{aligned} C_{DES} &= 0.65, \\ \Delta = h_{max} &= \max(dx, dy, dz). \end{aligned}$$

d is the distance from the wall, Δ is the maximum cell spacing and C_{DES} is a model constant. Substituting $\tilde{d}$ for d in the SA-RANS model is the only change required to obtain the SA-DES formulation. In the near-wall region, equation (1.1) yields $\tilde{d} = d$ which makes the DES formulation behave like the base SA-RANS model. As we move away from the wall, eventually $\tilde{d} = C_{DES}\Delta$. Using this reduced value for $\tilde{d}$ instead of d enhances the dissipation term in the effective eddy viscosity equation of the SA-RANS model, leading to a reduction in the eddy viscosity value. This allows the model to sustain/generate fluctuations, thus behaving like an LES model.

Another approach similar to DES is the Scale-Adaptive Simulation (SAS) by Menter and Egorov (2010). SAS also switches between a pure RANS and an LES-like behaviour. Here, the switch is independent of the grid spacing and instead relies on the local flow physics. However, this approach fails to sustain turbulent fluctuations in a channel flow.

A classic example of a case with a large separation region is the flow over a circular cylinder. Indeed, the prediction of such cases with massive separation was one of the main goals of DES. Figure 1.1 shows the vorticity isosurface obtained using the Spalart-Allmaras URANS model. As expected, the 2D URANS fails to predict the three-dimensionality in the solution. The 3D URANS solution is relatively better in this aspect, although the three-dimensionality is still coarse. The same geometry and flow configuration was simulated with the SA-DES model

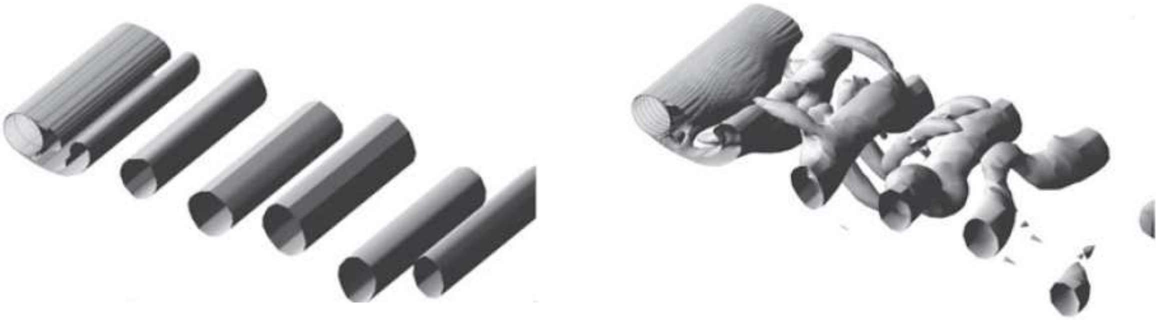

(a) 2D URANS

(b) 3D URANS

Figure 1.1: Flow over a circular cylinder using the SA-URANS model. Figure reproduced from Spalart (2009).

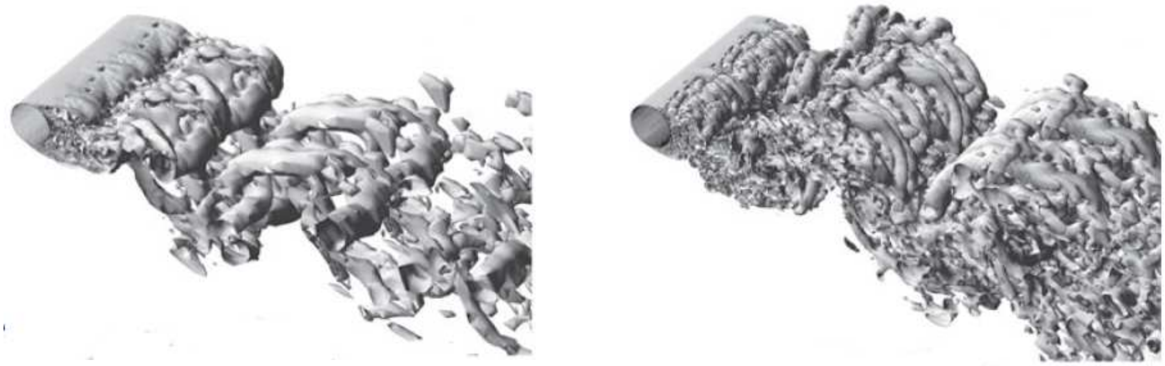

(a) Grid 1

(b) Grid 2

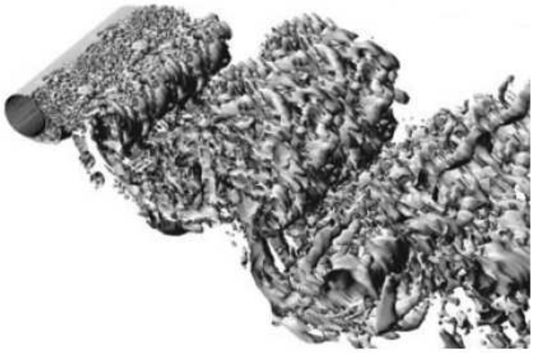

(c) Grid 3

Figure 1.2: Flow over a circular cylinder using the SA-DES model for 3 different grids. Figure reproduced from Spalart (2009).

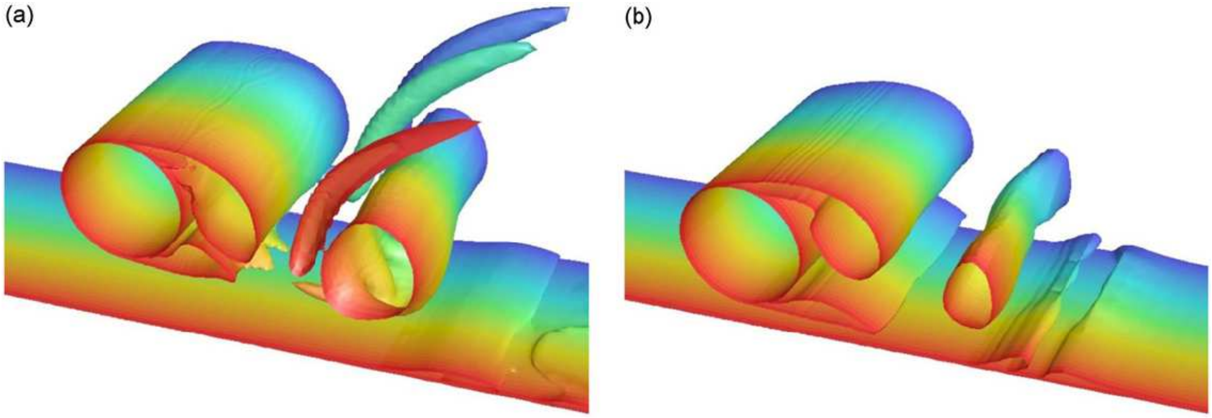

Figure 1.3: Iso-surfaces of the instantaneous vorticity magnitude using SA-URANS. a) $H/D = 0.6$ b) $H/D = 0.2$. Reprinted from Nishino et al. (2008) with permission from Elsevier.

using 3 different grids, with the results shown in figure 1.2. Among the 3 grids, grid 1 is the coarsest while grid 3 is the finest. The DES model is able to resolve the three-dimensionality of the flow. As the mesh resolution improves, more and more small scale structures are resolved. Contrary to the behaviour of the DES model, the RANS model did not show any improvement with grid refinement.

Another similar study comparing the behaviour of URANS and DES was carried out by Nishino et al. (2008). Here, the flow over a circular cylinder adjacent to a solid wall was simulated. 2 geometric parameters of importance here are the cylinder diameter D, and the distance between the cylinder and the ground H. Several simulations were carried out using both SA-URANS and SA-DES for different values of the gap ratio H/D. The cessation of vortex shedding occurs when the gap ratio H/D is reduced below a certain threshold value. This had been observed experimentally by Nishino and Roberts (2008). Specifically, the vortex shedding was no longer observed for $H/D = 0.2$. This behaviour, however, was not observed in the URANS simulation. Figure 1.3 shows vortex shedding occurring even for the $H/D = 0.2$ case. On the other hand, DES was able to reproduce the correct behaviour. Figure 1.4 shows the cessation of vortex shedding for $H/D = 0.2$.

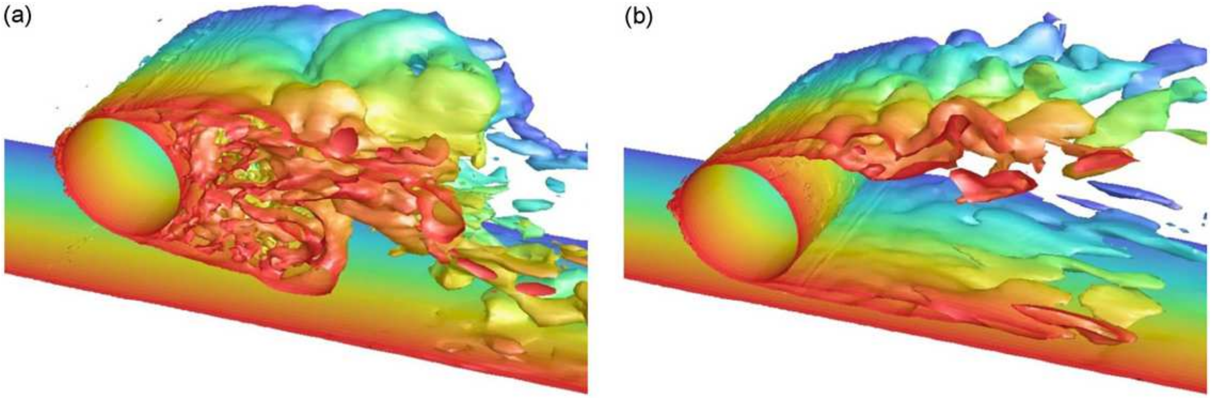

Figure 1.4: Iso-surfaces of the instantaneous vorticity magnitude using SA-DES. a) $H/D = 0.6$ b) $H/D = 0.2$. Reprinted from Nishino et al. (2008) with permission from Elsevier.

The flow over a delta wing at high angle of attack was studied by Morton (2003) using the SA-DES model. The wing is at an angle of attack $\alpha = 27^\circ$, a flow Mach number $M = 0.069$ and Reynolds number (based on the chord) $Re_c = 1.56 \times 10^6$. The simulation was carried out on 4 different grids. Figure 1.5 shows the vorticity iso-surfaces and the turbulent kinetic energy measured along the core of the vortex. DES is able to capture the unsteadiness well, and the results improve as the mesh is refined, both qualitatively (more small scale structures resolved) and quantitatively (more accurate turbulent kinetic energy prediction).

Besides the cases described thus far, the SA-DES model was shown to produce good results for several different flow configurations such as a landing-gear truck (Hedges et al. (2002)), ground vehicles (Kapadia et al. (2003); Maddox et al. (2004); Roy et al. (2004); Spalart and Squires (2004); Sreenivas et al. (2006)), active flow control by suction/blowing (Spalart et al. (2003); Krishnan et al. (2004)) and aerodynamic noise (Mockett et al. (2008); Greschner et al. (2008)) among others.

Additionally, it was also shown that the DES formulation is not exclusive to the SA-RANS model, but is applicable to other RANS models as well. Strelets (2001) applied the DES formulation to the $k-\omega$ SST RANS model of Menter (1993). The wall distance d was replaced

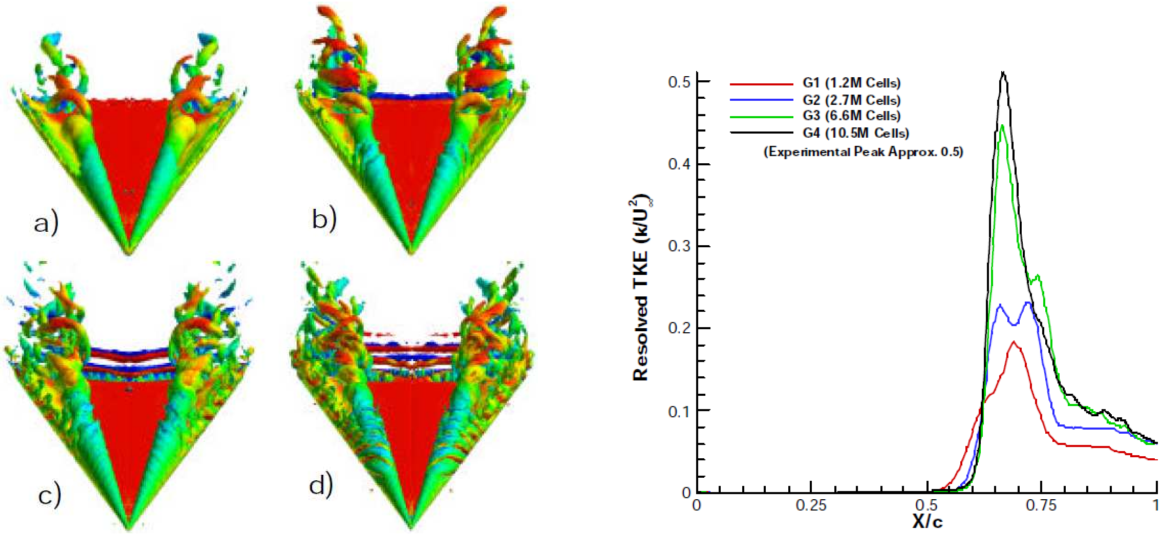

(a) Instantaneous vorticity iso-surfaces colored by the spanwise component of vorticity a) G1 (1.2M cells), b) G2 (2.7M cells), c) G3 (6.7M cells) d) G4 (10.7M cells)

(b) Normalized resolved turbulent kinetic energy for the four grids

Figure 1.5: Flow over a delta wing at $\alpha = 27°$, $M = 0.069$ and $Re_c = 1.56 \times 10^6$. Reproduced from Morton (2003).

by a RANS length scale $\ell_{k-\omega}$ such that

$$\ell_{k-\omega} = \frac{\sqrt{k}}{\beta^* \omega}, \qquad \beta^* = 0.09,$$
$$\tilde{\ell} = \min(\ell_{k-\omega}, C_{DES}\Delta).$$

$\tilde{\ell}$ was used (instead of $\tilde{d}$) to enhance the dissipation term in the $k - \omega$ SST RANS model. The performance of this DES formulation based on the SST RANS model was shown to be similar to the SA-DES model, which demonstrates that the concept of DES is not exclusive to the SA-RANS model.

However, despite the promising performance of DES, a couple of fundamental issues were identified.

The first issue is related to how the DES formulation switches between RANS and LES behaviour. From equation (1.1), we observe that the switch is dependent only on d and Δ, the latter of which is a grid parameter, making the switching criterion entirely dependent on the grid (for stationary meshes). This means that it is possible to generate a grid such that when the model switches from RANS to LES, the cell spacing is not fine enough to reproduce LES content, leading to an underprediction of the resolved Reynolds stresses. This was termed Modeled Stress Depletion (MSD) by Spalart et al. (2006). In severe cases, this could lead to premature flow separation due to underprediction of the local wall shear stress. This was demonstrated by Menter and Kuntz (2002), who used a DES formulation based on the $k-\omega$ SST RANS model (Strelets (2001)), for the case of a flow over an airfoil, where a local near-wall grid refinement led to premature flow separation and was termed Grid-Induced Separation (GIS). The separation here is determined by the grid, rather than the flow physics. Menter and Kuntz (2002) corrected this behaviour by utilizing the blending functions of the $k-\omega$ SST model to prevent the DES model from switching to LES behaviour within the boundary layer. A similar, more generic, approach was taken by Spalart et al. (2006) to prevent premature switching of the model behaviour. Rather than using the blending functions of the $k-\omega$ SST model (which are exclusive to that model), a more generic "shielding" function f_d, was introduced as shown below:

$$\tilde{d} = d - f_d \max(0, d - C_{DES}\Delta), \tag{1.2}$$

$$f_d = 1 - \tanh([8r_d]^3), \tag{1.3}$$

$$r_d = \frac{\nu_T + \nu}{\kappa^2 d^2 \sqrt{U_{i,j}U_{i,j}}}, \tag{1.4}$$

where ν_T is the eddy viscosity, ν the kinematic viscosity, κ the Von Kármán constant, and $U_{i,j}$ the velocity gradient tensor. The shielding function f_d is formulated such that within the boundary layer $f_d = 0$, and outside the boundary layer $f_d = 1$, with f_d transitioning from 0 to 1 towards the edge of the boundary layer. Hence $\tilde{d} = d$ within the boundary layer, and the DES model always exhibits RANS behaviour. This prevents MSD from occurring, which also avoids GIS. Outside the boundary layer equation (1.2) yields the original DES behaviour (equation 1.1). This formulation was termed Delayed DES or DDES (Spalart et al. (2006)). Like the DES formulation, DDES is not exclusive to the SA-RANS model, and can be applied to other RANS models as well. This is achieved by rewriting equation (1.2) as

$$l_{DDES} = l_{RANS} - f_d \max(0, l_{RANS} - l_{LES}), \tag{1.5}$$

where l_{RANS} and l_{LES} are the RANS and LES length scales respectively, defined based on the RANS model used. For the SA-RANS model, $l_{RANS} = d$ and $l_{LES} = C_{DES}\Delta$ yielding $l_{DDES} = \tilde{d}$. The generic DDES formulation has been applied to the $k - \omega$ SST RANS model by Gritskevich et al. (2012).

Application of DES to simulate turbulent channel flows led to the exposure of a second issue. Channel flow simulations by Nikitin et al. (2000) and Piomelli et al. (2003) resulted in 2 log-layers in the non-dimensional mean velocity profiles, each corresponding to the RANS and LES regions. Figure 1.6 shows the non-dimensional velocity profiles obtained for several channel flow cases, corresponding to a wide range of Reynolds numbers Re_τ (based on the friction velocity u_τ) and grid resolutions. All the profiles show that the log-layer computed by the LES region is offset from that computed by the RANS region by $\approx 3U^+$. This was termed Log-Layer Mismatch (LLM), and it was observed even in the DDES formulation (Spalart et al. (2006)). This led to another formulation known as Improved DDES or IDDES, by Shur et al. (2008), which aimed to alleviate LLM in addition to MSD. The IDDES formulation is partially reproduced below:

$$
\begin{aligned}
l_{IDDES} &= \tilde{f}_d(1+f_e)l_{RANS} + (1-\tilde{f}_d)l_{LES},\\
l_{LES} &= C_{DES}\Delta, \quad \Delta = \min[\max(C_w d_w, C_w h_{max}, h_{wn}), h_{max}],\\
\tilde{f}_d &= \max[(1-f_{dt}), f_B], \quad f_{dt} = 1 - \tanh[(8r_{dt})^3],\\
f_B &= \min[2\exp(-9\alpha^2), 1], \quad \alpha = 0.25 - d_w/h_{max},\\
f_e &= f_{e2}\max[(f_{e1}-1), 0],\\
f_{e1} &= \begin{cases} 2\exp\left(-11.09\alpha^2\right), & \text{if } \alpha \geq 0,\\ 2\exp\left(-9.0\alpha^2\right), & \text{if } \alpha < 0, \end{cases}\\
f_{e2} &= 1 - \max(f_t, f_l),\\
f_t &= \tanh[(c_t^2 r_{dt})^3], \quad f_l = \tanh[(c_l^2 r_{dl})^{10}],\\
r_{dt} &= \frac{\nu_T}{\kappa^2 d_w^2\sqrt{U_{i,j}U_{i,j}}}, \quad r_{dl} = \frac{\nu}{\kappa^2 d_w^2\sqrt{U_{i,j}U_{i,j}}}.
\end{aligned}
$$

More details regarding the IDDES formulation can be found in Shur et al. (2008).

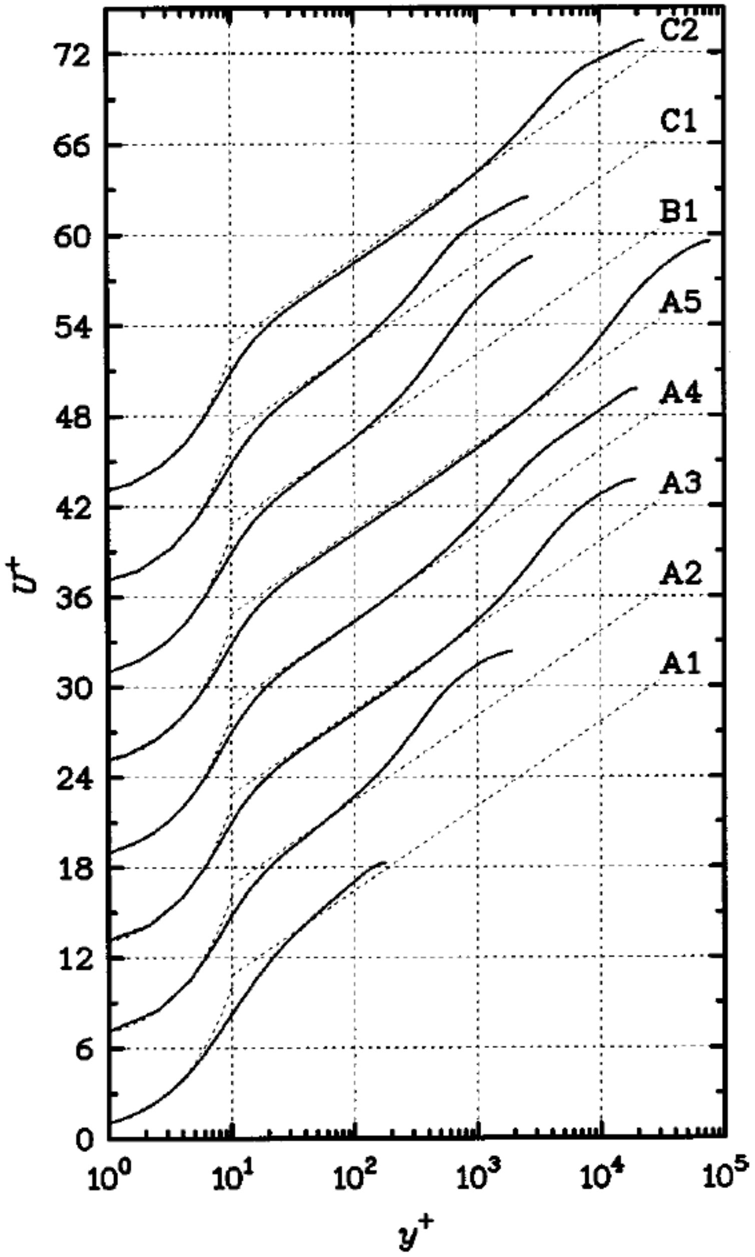

Figure 1.6: U^+ vs. y^+ profiles in channel flow for several Re_τ values and grids. Velocity profiles have been shifted by $5U^+$ units for the sake of clarity. Reprinted with permission from Nikitin et al. (2000). Copyright 2000, AIP Publishing LLC.

Clearly, the IDDES formulation is more involved than the DDES formulation. Several new functions have been introduced, some of which are empirical in nature. This makes the formulation seem ad hoc, and hard to understand. This additional complexity of the IDDES formulation was acknowledged by the original authors (Shur et al. (2008)).

The complexity and empiricism of the IDDES formulation is the motivation to explore an alternate, simpler DES formulation which can overcome both MSD and LLM, and will be the major focus of this dissertation. We expect a DES model to behave like a RANS model in the near-wall region, and switch to eddy simulation behaviour away from the wall. Hence one possible approach to come up with a new DES formulation is to start with a RANS model, and modify its formulation such that it behaves like a known LES model away from the walls. This can be accomplished by modifying the RANS eddy viscosity such that it mimics (for example) the Smagorinsky subgrid viscosity in the eddy simulation region. This approach will be detailed in Chapter 2, following a brief description of the governing equations and numerical modeling in the following sections.

1.2 Governing Equations

1.2.1 Conservation equations

For all cases/simulations considered in this dissertation, an incompressible flow assumption is made. Additionally, the fluid stresses are assumed to be Newtonian, with constant kinematic viscosity ν. With these assumptions, the governing fluid flow equations, in tensor notation, are:

$$\frac{\partial U_i}{\partial x_i} = 0, \tag{1.6}$$

$$\frac{DU_i}{Dt} = -\frac{1}{\rho}\frac{\partial P}{\partial x_i} + \frac{\partial \tau_{ij}}{\partial x_j}, \tag{1.7}$$

$$\tau_{ij} = \nu\left(\frac{\partial U_i}{\partial x_j} + \frac{\partial U_j}{\partial x_i}\right) = 2\nu S_{ij}, \tag{1.8}$$

where U_i is the velocity vector, ρ the fluid density, P the pressure and S_{ij} the strain rate tensor. $\frac{D}{Dt}$ represents the total derivative.

Equations (1.6) and (1.7) are the mass and momentum conservation equations respectively. In the case of a turbulent flow, these equations would represent the action of all fluid scales. However, when using a turbulence model, only a certain range of the larger scales are resolved, with the effect of the smaller scales being modeled. A common approach of separating the resolved and unresolved scales by using a filter is shown below:

$$U_i = \overline{U}_i + u_i.$$

$\overline{U}_i$ represents the filtered (or resolved) portion of the velocity, while u_i is the residual (or unresolved) portion. If the filtering operation is applied to the governing equations, it leads to a set of equations for the filtered variables as shown:

$$\frac{\partial \overline{U}_i}{\partial x_i} = 0, \tag{1.9}$$

$$\frac{\partial \overline{U}_i}{\partial t} + \frac{\partial \overline{U_i U_j}}{\partial x_j} = -\frac{1}{\rho}\frac{\partial \overline{P}}{\partial x_i} + \frac{\partial}{\partial x_j}[2\nu \overline{S}_{ij}]. \tag{1.10}$$

Here, it is assumed that differentiation and filtering commute. Details of the filtering operation can be found in several standard references such as Pope (2000).

In general, $\overline{U_i U_j} \neq \overline{U}_i \overline{U}_j$ which makes equation (1.10) different from the momentum equation (1.7). Defining

$$\tau^s_{ij} = \overline{U_i U_j} - \overline{U}_i \overline{U}_j,$$

equation (1.10) can be rewritten as

$$\frac{D\overline{U}_i}{Dt} = -\frac{1}{\rho}\frac{\partial \overline{P}}{\partial x_i} + \frac{\partial}{\partial x_j}[2\nu \overline{S}_{ij}] - \frac{\partial \tau^s_{ij}}{\partial x_j}. \tag{1.11}$$

The term τ^s_{ij} represents the effect of the unresolved scales on the filtered velocity field. Since only the larger scales are being resolved, the value of τ^s_{ij} is not known explicitly and needs to be modeled. The type of filter used determines the modeling approach (RANS or LES). For RANS models, the filtering operation represents an ensemble average such that

$$\bar{u}_i = 0,$$

$$\Rightarrow \overline{U_i U_j} = \overline{U}_i \overline{U}_j + \overline{u_i u_j}.$$

This is known as Reynolds-averaging. Following this equation (1.11) can be written as

$$\frac{D\bar{U}_i}{Dt} = -\frac{1}{\rho}\frac{\partial \bar{P}}{\partial x_i} + \frac{\partial}{\partial x_j}[2\nu\bar{S}_{ij}] - \frac{\partial \overline{u_i u_j}}{\partial x_j}. \tag{1.12}$$

Equation (1.12) is the governing equation for the average/mean velocity. $\overline{u_i u_j}$ is known as the Reynolds stress tensor and needs to be modeled to obtain closure. One of the most common modeling approaches is to express the anisotropic portion of the Reynolds stresses as being proportional to the filtered strain rate tensor, such that

$$\overline{u_i u_j} = \frac{2}{3}k\delta_{ij} - 2\nu_T\bar{S}_{ij}. \tag{1.13}$$

This is popularly known as the Boussinesq approximation. $k = \frac{1}{2}\overline{u_i u_i}$ is known as the turbulent kinetic energy. Using equation (1.13), the filtered momentum equation (1.12) now becomes

$$\begin{aligned} \frac{D\bar{U}_i}{Dt} &= -\frac{1}{\rho}\frac{\partial}{\partial x_i}(\bar{P} + \frac{2}{3}\rho k) + \frac{\partial}{\partial x_j}[2(\nu + \nu_T)\bar{S}_{ij}], \\ \Rightarrow \frac{D\bar{U}_i}{Dt} &= -\frac{1}{\rho}\frac{\partial \tilde{P}}{\partial x_i} + \frac{\partial}{\partial x_j}[2(\nu + \nu_T)\bar{S}_{ij}]. \end{aligned} \tag{1.14}$$

The isotropic portion of the Reynolds stress tensor is absorbed into the pressure to yield a modified mean pressure term $\tilde{P}$. The effect of the modeled scales is represented by ν_T, which acts like the molecular viscosity, and results in a mixing action.

Equations (1.9) and (1.14) are the final forms of the filtered mass and momentum conservation equations which need to be solved. The mass conservation equation is usually not solved explicitly, but is instead satisfied by solving a pressure equation. Details regarding the pressure equation and it's solution will be presented in section 1.3.

1.2.2 Turbulence model description

The momentum equation (1.14) remains unclosed since ν_T is yet to be defined. There are a plethora of methods available to define ν_T, with each method corresponding to a different turbulence model. In this dissertation however, we will be focusing on the $k-\omega$ RANS model of Wilcox (1993), which is described as:

$$\frac{\overline{D}k}{Dt} = \underbrace{2\nu_T|S|^2}_{\text{P}} - C_\mu k\omega + \nabla\cdot[(\nu+\sigma_k\nu_T)\nabla k], \tag{1.15}$$

$$\frac{\overline{D}\omega}{Dt} = 2C_{\omega1}|S|^2 - C_{\omega2}\omega^2 + \nabla\cdot[(\nu+\sigma_\omega\nu_T)\nabla\omega], \tag{1.16}$$

$$\nu_T = \frac{k}{\omega}, \tag{1.17}$$

where

$$\frac{\overline{D}}{Dt} = \frac{\partial}{\partial t} + \overline{U}_j\frac{\partial}{\partial x_j},$$

$$|S| = \sqrt{2S_{ij}S_{ij}}.$$

Equation (1.15) describes the evolution of $k = \frac{1}{2}\overline{u_i u_i}$, which is the turbulent kinetic energy (TKE). It is possible to formally derive an equation for k by subtracting the mean velocity equation (1.12) from the instantaneous velocity equation (1.7), which would yield a governing equation for the fluctuating velocity u_i. Multiplying this equation by u_i and taking the Reynolds average of the entire equation then results in the TKE equation (see Appendix A for details). Equation (1.15) is based on this TKE equation.

However, the TKE equation and equation (1.15) are not exactly the same. The mean velocity momentum equation has an unclosed Reynolds stress term, which leads to additional unclosed terms in the TKE equation (some of which are of higher order than the Reynolds stress tensor). Some of these terms can be closed by the Boussinesq assumption, while additional approximation would be required to close the remaining terms. The production term in the TKE equation has been closed via the Boussinesq approximation which yields term P. The dissipation and transport terms have been closed using additional approximations, with the final result being equation (1.15).

$k = \frac{1}{2}\overline{u_i u_i}$ is the turbulent kinetic energy. In the RANS formulation, only the mean flow is resolved, with the effect of all the fluctuations being modeled. Hence k here is better known as the modeled turbulent kinetic energy.

Broadly, we can think of k as representing the portion of the turbulent kinetic energy due to the unresolved scales. When the DES formulation is introduced into the RANS model, some of the smaller scales which were previously modeled are now resolved. k would then represent the remaining unresolved scales, and it's value would change from the RANS value to reflect this.

The second equation (1.16) in the model describes the evolution of ω ($\propto \frac{\epsilon}{k}$), which is known as the specific dissipation rate and has the units of $(\text{time})^{-1}$. ϵ is the rate of dissipation of k. Unlike k and the k-equation (1.15), there is no compelling physical meaning behind the definition of ω and the ω-equation (1.16). In 2-equation models, the first variable of choice is almost always k, given that it describes real physical processes. The choice of the second variable/equation however is not as clear. Several models have been proposed which use different variables (besides ω), such as a turbulence length scale ℓ (Rotta (1951, 1968)), a turbulence dissipation time τ (Zeierman and Wolfshtein (1986); Speziale et al. (1990)), the turbulent kinetic energy dissipation rate ϵ (Jones and Launder (1972); Launder and Sharma (1974)) and the enstrophy ζ (Robinson et al. (1995)) where $\zeta \sim \omega^2$. A discussion/comparison of the pros and cons of all these different models (not to mention algebraic and one-equation models) is beyond the scope of this dissertation. However, it is worth stating that the $k - \omega$ RANS model exhibits very good near-wall behaviour (Wilcox (1993)) compared to other RANS models. In the DES formulation, the RANS model is active only in the near-wall region. Hence it is quite natural to choose $k - \omega$ as the base RANS model.

The values of the constants used are

$$C_\mu = 0.09, \quad \sigma_k = \sigma_\omega = 0.5, \quad C_{\omega 1} = 5/9, \quad C_{\omega 2} = 3/40.$$

These values were determined by calibrating the model to perform adequately for several canonical flows such as channel flow, decay of grid turbulence etc.

Solving equations (1.15) and (1.16) to obtain ν_T would require the specification of boundary conditions for k and ω. Of prime importance are the wall boundary conditions. For a simulation where the wall-normal cell spacing is fine enough such that the viscous sublayer and the buffer layer are resolved, the following boundary conditions are used:

$$
\begin{aligned}
k_{wall} &= 0, \\
\omega_{wall} &\rightarrow \frac{6\nu}{\beta d^2} \qquad \text{as } d \rightarrow 0.
\end{aligned}
$$

The specification of k_{wall} is straight-forward — all velocity values become 0 at the wall and hence $k = 0$ at the wall. The ω_{wall} specification however becomes complicated since theoretically, $\omega_{wall} = \infty$ due to $k_{wall} = 0$, and the TKE dissipation (defined by velocity gradients) at the wall $\epsilon_{wall} \neq 0$. Thus the wall boundary condition for ω instead describes an asymptotic behaviour. Here $\beta = 0.075$ and d is the wall distance at the cell adjacent to the wall.

For simulations where the near-wall region is not well resolved, wall functions would need to be used to mimic the behaviour of the unresolved viscous and buffer layers. Details regarding such wall functions can be found in Esch and Menter (2003). All the simulations presented in this dissertation use fine wall normal cell spacing to resolve the viscous and buffer layers.

Equations (1.15) and (1.16) are now solved to obtain the value of the eddy viscosity ν_T from equation (1.17). This is in turn used to attain closure of the filtered momentum equation (1.14). This completes the description of the $k - \omega$ RANS model.

The DES formulation described in this dissertation will be based on the $k - \omega$ RANS model described thus far, where the eddy viscosity equation (1.17) will be modified and used to limit the production term (with the details presented in Chapter 2).

1.3 Numerical Modeling

To solve the governing equations, the open-source code OpenFOAM (*http://www.openfoam.org*) was utilized. A description of the basic structure of the code and the algorithms used can be found in Weller et al. (1998). OpenFOAM is an unstructured, Finite Volume (FV) solver, capable of solving an arbitrary number of coupled partial differential equations. A major advantage of using a FV solver is that unstructured meshes can be used easily. This is especially convenient when simulating complex geometries.

In the FV method, the spatial domain is sub-divided into several smaller control volumes (CV). The values of the dependent variables such as $\overline{U}$ and $\overline{P}$ are stored at the centroid of each CV in a collocated arrangement. Another option is to store the scalar variables in the cell centroids, while the velocities are stored at the cell faces. This is a staggered arrangement. In OpenFOAM, the collocated arrangement is used.

The governing equations (1.9) and (1.14) expressed in vector form are

$$\nabla \cdot \overline{U} = 0, \tag{1.18}$$

$$\frac{\partial \overline{U}}{\partial t} + \nabla \cdot (\bar{U}\bar{U}) = -\frac{1}{\rho}\nabla \tilde{P} + \nabla \cdot ((\nu + \nu_T)(\nabla \overline{U} + \nabla \overline{U}^T)). \tag{1.19}$$

$\overline{U}$ is the filtered velocity vector. In the FV approach, equations (1.18) and (1.19) are integrated over the CV which yields

$$\int_V (\nabla \cdot \overline{U}) dV = 0, \tag{1.20}$$

$$\frac{d}{dt}\int_V \bar{U} dV + \int_V \nabla \cdot (\bar{U}\bar{U}) dV = -\frac{1}{\rho}\int_V (\nabla \tilde{P}) dV + \int_V \nabla \cdot (\nu_e(\nabla \overline{U} + \nabla \overline{U}^T)) dV, \tag{1.21}$$

where $\nu_e = \nu + \nu_T$ is the effective viscosity. The value of the eddy viscosity ν_T is obtained by solving the $k - \omega$ RANS equations (1.15-1.17). Similar to the momentum equation (1.21), the RANS equations (1.15, 1.16) are also solved using the FV approach, with the equations being integrated over a control volume and in time. The discretization of the individual terms in the RANS equations is done in a similar manner as in the momentum equation. Hence only the discretization of the momentum equation will be described in detail, with the same procedure being followed for the RANS equations. The discretization techniques used to approximate these integrals will be explained in section 1.3.1.

In addition to the volume integrals, equation (1.21) also has a time derivative which needs to be solved. This can be solved by employing a temporal discretization, where the solution is marched forward in time, over a time step Δt, starting from an initial condition. Details regarding the temporal discretization will be presented in section 1.3.2.

1.3.1 Spatial discretization

In the 2^{nd} order FV approach, the values of the variables stored at the centroid of the CV are assumed to be constant over the entire CV. Thus the volume integral within the time derivative becomes

$$\int_{V_c} \overline{U} dV \approx \overline{U}_c V_c, \tag{1.22}$$

where V_c is the cell volume and $\overline{U}_c$ is the value of the velocity vector stored at its centroid.

In OpenFOAM, some of the volume integrals in equation (1.21) are converted to surface integrals via Gauss's divergence theorem which states that

$$\int_V \nabla \cdot \phi dV = \oint_S \phi \cdot \boldsymbol{dS}, \tag{1.23}$$

where ϕ is an arbitrary tensor field of at least 1^{st} order, S the bounding surface of the volume V, and $\boldsymbol{dS}$ the infinitesimal area vector pointing outward. The surface integrals are in turn approximated as the sum of the fluxes across the cell faces.

$$\oint_S \phi \cdot \boldsymbol{dS} \approx \sum_f \boldsymbol{S_f} \cdot \phi_f. \tag{1.24}$$

The summation here is over all the cell faces. $\boldsymbol{S_f}$ is the face area vector. ϕ_f is the value of ϕ at the face f and is assumed to be constant over the entire face. Since the variable values are stored at the cell centers, some kind of interpolation needs to be performed to estimate ϕ_f.

The requirements of the interpolation scheme to be used varies depending on whether we are using a RANS model or an LES model. An LES model aims to capture small scale fluctuations. This means that if the scheme being used is diffusive, it will reduce the amplitude of the fluctuations, and in the worst case, it could completely dampen them. An example of such a dissipative scheme is the Upwind Difference scheme which can be of either first order or second order (Warming and Beam (1976)). Hence although such schemes would be compatible with RANS models, they cannot be used in conjunction with LES or hybrid RANS/LES methods.

Hence it is quite clear that a non-dissipative scheme needs to be used for spatial discretization. A viable option in this case is the Central Difference (CD) method, which is 2^{nd} order accurate (Ferziger and Peric (2002)), and assumes linear variation of the solution between 2 control volumes such that,

$$\phi_f = d\phi_C + (1 - d)\phi_N. \tag{1.25}$$

ϕ_C represents the variable value at the current cell, and ϕ_N is that at a neighbouring cell for which f is the common face. d here is a distance factor such that $d = |\overrightarrow{fN}|/|\overrightarrow{CN}|$. $|\overrightarrow{fN}|$ is the distance between the centroid of neighbour N and face f. Likewise, $|\overrightarrow{CN}|$ is the distance between the current cell C and neighbour N.

Given that a DES method (which is hybrid RANS/LES) will be used for all the simulations presented in this dissertation, unless otherwise stated explicitly, the Central Difference scheme is the method of choice for the spatial interpolation/discretization of all the terms in the governing equations, in order to minimize errors due to numerical dissipation.

The non-dissipative nature of the CD scheme can be a double-edged sword depending on the application, since it is known to become unstable. A cell Reynolds number Re_c can be defined as

$$Re_c = \frac{\bar{U}\Delta}{\nu_\phi},$$

where Δ is a measure of the cell dimension and ν_ϕ is the diffusion coefficient of the variable ϕ for which the CD interpolation is being used ($\nu_\phi = \nu$ for $\phi = \bar{U}$). For $Re_c > 2$, the CD method is likely to become unstable (de Villiers (2006)), in which case the mesh would have to be refined to obtain a stable solution.

The convection term in equation (1.21) is simplified using equations (1.23) and (1.24) as follows

$$\begin{aligned}
\int_{V_c} \nabla \cdot (\bar{U}\bar{U}) dV &= \oint_{S_c} \boldsymbol{dS} \cdot (\bar{U}\bar{U}), \\
&\approx \sum_f \boldsymbol{S_f} \cdot (\bar{U}_f \bar{U}_f), \\
&= \sum_f (\boldsymbol{S_f} \cdot \bar{U}_f)\bar{U}_f.
\end{aligned} \tag{1.26}$$

Here both the flux ($\boldsymbol{S_f}\cdot\bar{U}_f$) and the convected variable ($\bar{U}_f$) are unknown resulting in a quadratic function for velocity. In order to simplify this, the flux term is computed using velocity values from a previous iteration/time step. Equation (1.26) then becomes

$$\int_{V_c} \nabla \cdot (\bar{U}\bar{U})dV \approx \sum_f (\boldsymbol{S_f} \cdot \bar{U}_f^{n-1})\bar{U}_f^{n}. \tag{1.27}$$

Here the superscript n refers to the current iteration for which the variables values need to be computed, while $n-1$ refers to values from a previous iteration/time step which are known. Typically, the momentum equation is solved iteratively until the velocity values do not change significantly between successive iterations. This ensures that $\bar{U}_f^{n-1} = \bar{U}_f^{n}$ towards the end of the iteration (within a specified tolerance). This will be explained later in section 1.3.3.

Gauss's theorem is also used to simplify the diffusion term in equation (1.21). This yields, for a generic diffusion term,

$$\begin{aligned}\int_{V_c} \nabla \cdot (\nu_\phi \nabla\phi)dV &\approx \sum_f \boldsymbol{S_f} \cdot (\nu_\phi \nabla\phi)_f,\\ &= \sum_f (\nu_\phi)_f \boldsymbol{S_f} \cdot (\nabla\phi)_f. \end{aligned}\tag{1.28}$$

Equation (1.28) represents the discretization for the diffusion of a generic variable ϕ. The diffusion coefficient $(\nu_\phi)_f$ is calculated via the CD method (equation 1.25). The face gradient $(\nabla\phi)_f$ is found using

$$\boldsymbol{S_f} \cdot (\nabla\phi)_f = |\boldsymbol{S_f}|\frac{\phi_N - \phi_C}{|\overrightarrow{CN}|}. \tag{1.29}$$

The above equation works only if $\boldsymbol{S_f}$ and $\overrightarrow{CN}$ are parallel, i.e. the mesh is orthogonal. For non-orthogonal meshes, the following relation is used

$$\boldsymbol{S_f} \cdot (\nabla\phi)_f = \underbrace{|\boldsymbol{S_{f_{CN}}}|\frac{\phi_N - \phi_C}{|\overrightarrow{CN}|}}_{\text{orthogonal}} + \underbrace{\boldsymbol{S_{f_d}} \cdot (\widetilde{\nabla\phi})_f}_{\text{non-orthogonal}}, \tag{1.30}$$

$$(\widetilde{\nabla\phi})_f = d(\nabla\phi)_C + (1-d)(\nabla\phi)_N, \tag{1.31}$$

$$(\nabla\phi)_C = \frac{1}{V_c}\sum_f \boldsymbol{S}_f\phi_f, \tag{1.32}$$

where $\boldsymbol{S_{f_{CN}}}$ represents the component of $\boldsymbol{S_f}$ parallel to $\overrightarrow{CN}$, and $\boldsymbol{S_{f_d}} = \boldsymbol{S_f} - \boldsymbol{S_{f_{CN}}}$. Equation (1.31) is analogous to equation (1.25).

Equation (1.30) results in a larger stencil to compute the face gradients when the mesh is non-orthogonal. In order to retain the same stencil as the orthogonal case, the non-orthogonal term is computed explicitly using ϕ values from the previous iteration/time step.

The non-orthogonal correction term could lead to solution instability when the mesh non-orthogonality is high (de Villiers (2006)). Hence the grid used must be constructed such that the non-orthogonality is kept to a minimum.

The discretization described above is applied to the diffusion term in equation (1.21) as follows

$$\begin{aligned}\int_{V_c} \nabla \cdot (\nu_e(\nabla\overline{U} + \nabla\overline{U}^T))dV &= \int_{V_c} \nabla \cdot (\nu_e(\nabla\overline{U}))dV + \int_{V_c} \nabla \cdot (\nu_e(\nabla\overline{U}^T))dV, \\ &\approx \sum_f (\nu_e)_f \boldsymbol{S_f} \cdot (\nabla\overline{U})_f + \nabla \cdot [\nu_e \nabla(\overline{U}^{n-1})^T]V_c. \qquad (1.33)\end{aligned}$$

In OpenFOAM, the diffusion term is split into 2 terms — one containing $\nabla\overline{U}$ and the other with its transpose $\nabla\overline{U}^T$. Treating the transpose term as a diffusion term as well would result in the value of each velocity component become dependent on the other components (since each row in $\nabla\overline{U}^T$ contains u, v and w gradients) resulting in a linked system of equations which would increase the computation cost. Therefore, the transpose term is computed explicitly using values from the previous iteration/time step, while the gradient term is treated in a similar manner as the generic diffusion term.

1.3.2 Temporal discretization

The temporal discretization scheme used in OpenFOAM is now described.

In order to obtain 2^{nd} order accurate solutions, both the spatial and temporal discretizations need to be 2^{nd} order accurate. If f^n represents the solution at the current time step, then f^{n-1}, f^{n+1} are the solutions at the previous and next time step respectively. f^{n-1} and f^n are known, while f^{n+1} needs to be calculated. A simple 2^{nd} order accurate implicit scheme for approximating the temporal derivative can be obtained using Taylor series expansion for f^{n-1} and f^n around f^{n+1} as follows:

$$f^{n-1} = f^{n+1} - 2f_t^{n+1}\Delta t + 2f_{tt}^{n+1}\Delta t^2 + O(\Delta t^3), \tag{1.34}$$

$$f^n = f^{n+1} - f_t^{n+1}\Delta t + 0.5f_{tt}^{n+1}\Delta t^2 + O(\Delta t^3), \tag{1.35}$$

$$\Rightarrow 2f^n - \frac{1}{2}f^{n-1} = \frac{3}{2}f^{n+1} - f_t^{n+1}\Delta t + O(\Delta t^3), \tag{1.36}$$

$$\Rightarrow f_t^{n+1} = \frac{1}{\Delta t}\left(\frac{3}{2}f^{n+1} - 2f^n + \frac{1}{2}f^{n-1}\right) + O(\Delta t^2). \tag{1.37}$$

The subscripts t and tt represent first and second order differentiation with respect to time. Hence equation (1.37) represents the implicit discretization for the first order time derivative term, which can be used to discretize the temporal derivative in equation (1.21). As can be observed, the discretization is 2^{nd} order accurate in time. Since the spatial discretization is also 2^{nd} order accurate (CD method), the overall accuracy would be of 2^{nd} order.

1.3.3 The pressure equation

The spatial and temporal discretization of all the terms in the integral form of the momentum equation (1.21) have been dealt with in sections 1.3.1 and 1.3.2 except for the pressure gradient term.

Thus far we have 2 governing equations (1.20, 1.21) and 2 unknowns - the velocity $\overline{U}$ and pressure $\tilde{P}$. However, $\tilde{P}$ only appears in 1 equation. In compressible flows, a state equation relating pressure to density is normally used to compute the pressure. For incompressible flows (as is the case in this dissertation), this is no longer possible and a different equation for pressure is required. The pressure is solved for using the PISO (Pressure Implicit with Splitting of Operators) algorithm of Issa (1986). Once the discretization techniques described in sections 1.3.1 and 1.3.2 are applied to the momentum equation (1.21), a system of equations are obtained

$$A\overline{U} = -\nabla\tilde{P}. \tag{1.38}$$

The pressure gradient term $\nabla\tilde{P}$ is yet to be discretized. A represents the coefficient matrix obtained after discretization (which is known). The A matrix is now split as

$$A\bar{U} = A_c\bar{U} - \boldsymbol{H}, \tag{1.39}$$

$$\Rightarrow A_c\bar{U} = \boldsymbol{H} - \nabla\tilde{P}. \tag{1.40}$$

A_c is the diagonal of A which contains the current cell coefficients. $-\boldsymbol{H}$ contains the off-diagonal terms which represent the neighbour coefficients multiplied by their respective velocities. Then equation (1.40) can be written as

$$\bar{U} = (A_c)^{-1}\boldsymbol{H} - (A_c)^{-1}\nabla\tilde{P}. \tag{1.41}$$

Applying mass conservation, we get

$$\nabla\cdot\bar{U} = \nabla\cdot[(A_c)^{-1}\boldsymbol{H} - (A_c)^{-1}\nabla\tilde{P}],$$

$$\Rightarrow \nabla\cdot[(A_c)^{-1}\nabla\tilde{P}] = \nabla\cdot[(A_c)^{-1}\boldsymbol{H}]. \tag{1.42}$$

Since A_c is a diagonal matrix, computing $(A_c)^{-1}$ is straight-forward. Equation (1.42) is the Pressure Poisson equation which can be used to solve for pressure. Since mass conservation was employed in the derivation, solving the pressure equation obviates the need to solve the mass conservation equation separately.

Equation (1.42) is written for a single CV as

$$\nabla\cdot\left[\frac{\nabla\tilde{P}_c}{a_c}\right] = \nabla\cdot\left[\frac{\boldsymbol{h}}{a_c}\right]. \tag{1.43}$$

a_c and $\boldsymbol{h}$ are the coefficients for the current cell and its neighbours respectively ($\boldsymbol{h}$ contains the velocities as well). Similarly, equation (1.41) is written for a single CV and face values as

$$\bar{U}_c = \left(\frac{\boldsymbol{h}}{a_c}\right) - \left(\frac{\nabla\tilde{P}_c}{a_c}\right), \tag{1.44}$$

$$(\bar{U}_c)_f = \left(\frac{\boldsymbol{h}}{a_c}\right)_f - \left(\frac{\nabla\tilde{P}_c}{a_c}\right)_f. \tag{1.45}$$

Equation (1.44) is used to compute the velocities at the cell centers once the pressure is known. Likewise, the face values are updated using equation (1.45) to compute the fluxes.

Gauss's divergence theorem is applied to equation (1.43) which, for a single CV, yields the following

$$\sum_f \boldsymbol{S_f} \cdot \left(\frac{1}{a_c}\right)_f (\nabla \tilde{P}_c)_f = \sum_f \boldsymbol{S_f} \cdot \left(\frac{\boldsymbol{h}}{a_c}\right)_f, \tag{1.46}$$

where the pressure Laplacian is treated in a similar manner to the generic diffusion term.

The PISO algorithm can now be described:

1. The turbulence variables (k, ω, ν_T) are first computed using the velocity, pressure and flux values from the previous iteration/time step or the initial conditions. The individual terms in the turbulence equations are treated in the same manner as those in the momentum equation.

2. The momentum equation is solved using the previous iteration/time step values for $\tilde{P}$ and the fluxes. The matrix system is solved using the Preconditioned BiConjugate Gradient algorithm, with the simplified, diagonal-based, incomplete-LU preconditioner (Ferziger and Peric (2002)). The iterations are repeated until the velocity values between 2 successive iterations do not differ by a value larger than a specified tolerance. The resulting velocity field is $\overline{U}^*$. In general, $\overline{U}^*$ does not satisfy the continuity equation since the pressure equation is yet to be solved. This is the predictor step.

3. $\overline{U}^*$ is used to update the $\boldsymbol{H}$ matrix and the pressure equation is now solved using the Preconditioned Conjugate Gradient algorithm, with the diagonal incomplete Cholesky preconditioner (Ferziger and Peric (2002)). This is the corrector step.

4. For non-orthogonal meshes, the pressure equation is solved again in order to converge the non-orthogonal component. Depending on the mesh non-orthogonality, 1-2 corrector steps might be required.

5. Once the pressure is known, the velocities at the cell centers and the fluxes at the cell faces are updated using equations (1.44) and (1.45).

6. Steps 3-5 are repeated until the solution variables do not change significantly (based on a user-specified tolerance) between successive iterations.
7. The algorithm now proceeds to the next time step, with the current values used as initial guesses, and the entire solution procedure is repeated. This goes on until either the solution variables do not change significantly between successive time steps, or a certain no: of time steps have passed (depends on user-input).

CHAPTER 2. A DDES MODEL WITH A SMAGORINSKY-TYPE EDDY VISCOSITY FORMULATION AND LOG-LAYER MISMATCH CORRECTION

K. R. Reddy, J. A. Ryon, P. A. Durbin, (2014)

International Journal of Heat and Fluid Flow, 50, 103-113

The current work develops a variant of delayed detached eddy simulation (DDES) that could be characterized as limiting the production term. Previous formulations have been based on limiting the dissipation rate (Spalart et al. (2006)). A clipped length scale is applied directly to the eddy viscosity, yielding a Smagorinsky-like formulation when the model is on the eddy simulation branch. That clipped eddy viscosity limits the production rate. The length scale is modified in order to account for the log-layer mismatch (a well-known issue with DDES), without using additional blending functions. Another view of our approach is that the subgrid eddy-viscosity is represented by a mixing length formula $l^2\omega$; in the eddy field ω acts like a filtered rate of strain. Our model is validated for channel flow as well as separated flows (backward-facing step, 2D periodic hills) and illustrated via an air-blast atomizer.

2.1 Introduction

Hybrid RANS/LES models are considered to have promise for industrial CFD applications, where the idea is to employ RANS in the near wall part of attached boundary layers, and eddy resolving simulation in regions away from the surface. Detached Eddy Simulation (DES) falls under this category of hybrid methods. DES was first proposed by Spalart et al. (1997) and since then, the method has undergone considerable revision. Menter and Kuntz (2002) pointed out that artificial Grid Induced Separation (GIS) could occur if, when the switch from RANS to Eddy Simulation took place, the reduction of eddy viscosity was not balanced by resolved turbulent content. This effect was termed Modeled Stress Depletion (MSD). Towards this end, the blending functions of the $k - \omega$ SST model were used as a "shield" to prevent the model from switching to eddy simulation within the lower part of the boundary layer. Following this, Spalart et al. (2006) introduced a generic shielding function, applicable to any RANS model, and the resulting formulation was termed Delayed DES (DDES) — although it might better be called shielded DES.

Another perspective on DES is that it has an ability to function as a type of Wall-Modeled LES (WMLES). Initial attempts to use the original DES as a WMLES formulation in a channel flow (Nikitin et al. (2000); Piomelli et al. (2003)) resulted in two, mismatched log-layers — one from the RANS branch, and the other from the eddy resolving branch. This anamoly was termed Log-Layer Mismatch (LLM) — an issue which is present in the DDES formulation as well.

Breuer et al. (2003) noted that $h_{max} = \max(dx, dy, dz)$ may not be a suitable length scale to use in the eddying regions of DES, and that using $V^{1/3}$ instead, where V is the cell volume, produced better results. The fact that a different length scale definition is required was also implied in a formulation termed Improved DDES (IDDES) (Shur et al. (2008)), which required the modification of the length scale definition to be used in the eddying region. In addition to revised length scales, more complex blending functions were introduced in order to ensure that the model performed adequately as a WMLES formulation. The blending functions in the IDDES formulation are responsible for allowing the LES functionality within the boundary layer in the presence of turbulent fluctuations, provided the grid is fine enough. And along with a modified length scale definition, they alleviate LLM seen in the channel flow. This is the key difference between DDES and IDDES.

Yet another variation of DES, known as Zonal DES (ZDES) (Deck (2012)) also employs $V^{1/3}$ (or Δ_ω, which depends on the orientation of the vorticity ω as well as the local cell spacing) in the eddying region. However, as the name would suggest, ZDES requires the user to specify the RANS and eddying regions.

In the present article, a different variant of DDES is developed and applied to the $k-\omega$ model (Wilcox (1993)). The motive for the present approach is to make DES more similar to LES in the eddying region. It has been observed (Spalart (2009); Breuer et al. (2003)) that LES often produces more accurate results than DES. Hence, our objective is to make use of DES to reduce near-wall grid requirements (Spalart et al. (2006)) and, simultaneously, to make the eddy viscosity similar to the Smagorinsky formula far from the surface.

Rather than utilizing the length scale in the dissipation term of the k-equation, it is used to define the subgrid eddy viscosity, which is then used to define the production term. This definition of the eddy viscosity makes it a function of the length scale, similar to the definition used for the subgrid eddy viscosity in the Smagorinsky model. This definition additionally provides a method to estimate the value of the model constant by comparing it to the Smagorinsky eddy viscosity formulation. Hence the model can be viewed as a Smagorinsky DES model with $k-\omega$ as the underlying RANS model.

Additionally, the length scale is redefined to ameliorate the issue of LLM without requiring the blending functions of IDDES. The absence of any blending functions (as described in Shur et al. (2008)) in the current formulation would indicate that the near wall behaviour of the current model is more similar to DDES than IDDES. This will be dealt with in more detail in §2.3.1.

The open source code OpenFOAM (Weller et al. (1998)) was used for all the present computer simulations. Gaussian finite volume integration with central differencing for interpolation, was selected for spatial discretization of equations. Time integration was by the 2^{nd} order, backward difference method. The resulting matrix system was solved using the Pre-conditioned Bi-conjugate gradient algorithm, with the simplified, diagonal-based, incomplete-LU preconditioner. Solution for the matrix system at each time step was obtained by solving iteratively, by specifying an appropriate tolerance for the residual norm.

2.2 Model Formulation

The eddy viscosity can be understood as the product of turbulence length-scale times velocity-scale. The DES method is to clip the length scale; but, alternatively, the velocity scale — or both velocity and length scales — could be clipped. This leads to our proposed method.

Let ℓ be a length scale, to be defined. In DES the RANS length scale is clipped by the grid dimension. For $k-\omega$, the RANS length scale is $\sqrt{k}/\omega$ and a length scale, ℓ, clipped for DES is defined as (Spalart et al. (1997))

$$\ell = \min\left[\sqrt{k}/\omega, C_{DES}\,\Delta\right], \tag{2.1}$$

where C_{DES} is an empirical constant, and Δ is an appropriate measure of grid size, *e.g.*, $\max[\Delta_x, \Delta_y, \Delta_z]$. $C_{DES}\Delta$ is a measure of whether the grid can capture the dominant turbulent eddies. One could alternatively use equation (2.1) to define a clipped velocity u_ℓ. Multiplying through by ω,

$$u_\ell = \min\left[\sqrt{k}, \omega\, C_{DES}\Delta\right]. \tag{2.2}$$

The eddy viscosity k/ω could be represented as $\ell^2\omega$ or as u_ℓ^2/ω; they lead to the same result: before clipping, either one is k/ω. After the clip is in effect

$$\nu_T = \ell^2\omega \rightarrow (C_{DES}\Delta)^2\omega, \tag{2.3}$$

similar to the Smagorinsky model.

The $k-\omega$ equations are (Wilcox (1993))

$$\begin{aligned} \frac{Dk}{Dt} &= 2\nu_T|\boldsymbol{S}|^2 - C_\mu k\omega + \partial_j\left[(\nu + \sigma_k\nu_T)\,\partial_j k\right], \\ \frac{D\omega}{Dt} &= 2C_{\omega 1}|\boldsymbol{S}|^2 - C_{\omega 2}\omega^2 + \partial_j\left[(\nu + \sigma_\omega\nu_T)\,\partial_j\omega\right], \\ \nu_T &= \frac{k}{\omega}. \end{aligned} \tag{2.4}$$

The clip (2.2) preempts the first of these; in the eddying region it, rather than the k-equation, defines the velocity scale. If the transport terms were dropped from the second of equations (2.4) it would become

$$\omega^2 = \frac{2C_{\omega 1}}{C_{\omega 2}}|\boldsymbol{S}|^2 = \frac{400}{27}\,|\boldsymbol{S}|^2.$$

The standard constants (Wilcox (1993)) $C_{\omega 1} = 5/9$, $C_{\omega 2} = 3/40$ were inserted. Then equation (2.3) becomes

$$\nu_T = (C_{DES}\Delta)^2\frac{20}{3\sqrt{3}}\sqrt{|\boldsymbol{S}|^2}.$$

The constant C_{DES} can be estimated by equating this to $(C_s\Delta)^2\sqrt{2\,|\boldsymbol{S}|^2}$, where C_s is the Smagorinsky constant (≈ 0.2). This estimate is $C_{DES} \approx 0.12$, which was found to be satisfactory in validation studies (discussed towards the end of the section).

Dropping transport terms from eqn. (2.4) is not legitimate, so one can view the proposed 2-equation DES model as equation (2.4), the clip (2.1 or 2.2) and the eddy viscosity definition

$$\nu_T = \ell^2\omega. \tag{2.5}$$

Away from the wall, the ω-transport equation (2.4) is a diffusive smoother of the rate-of-strain field. In that sense, it is a *filter* of the resolved eddy field. Equation (2.5) is analogous to the Smagorinsky model, in which this 'filtered' variable substitutes for the rate of strain. Near the wall, boundary conditions are dominant, and this interpretation of the ω-equation fails; but that is the RANS region.

The DDES modification introduces the shielding function f_d (Spalart et al. (2006))

$$\begin{aligned} f_d &= 1 - \tanh\left([C_{d1}r_d]^{C_{d2}}\right) \qquad [C_{d1} = 8, \quad C_{d2} = 3], \\ r_d &= \frac{k/\omega + \nu}{\kappa^2 d_w^2\sqrt{U_{i,j}U_{i,j}}}, \end{aligned} \tag{2.6}$$

into equation (2.1), where k/ω is the RANS eddy viscosity, ν the molecular viscosity, κ the von Kármán constant, d_w the distance to the wall, and $U_{i,j}$ is the velocity gradient tensor.

The DDES length scale is defined as

$$\begin{aligned} l_{DDES} &= l_{RANS} - f_d\max(0, l_{RANS} - l_{LES}), \\ l_{RANS} &= \frac{\sqrt{k}}{\omega}, \\ l_{LES} &= C_{DES}\Delta. \end{aligned} \tag{2.7}$$

The length scale l_{DDES} is then used to define the eddy viscosity ν_T as

$$\nu_T = l_{DDES}^2\,\omega, \tag{2.8}$$

so that when $f_d = 0$ the eddy viscosity formula gives $\nu_T = k/\omega$ and the model operates in RANS mode. Alternatively, when $f_d = 1$ and $l_{LES} < l_{RANS}$ the eddy viscosity formula gives $\nu_T = (C_{DES}\Delta)^2\omega$ and the model is fully in eddy simulation mode.

This definition of ν_T is used in the turbulent kinetic energy production term, leaving all the other terms unaltered.

$$\begin{aligned}\frac{Dk}{Dt} &= \boldsymbol{2\nu_T|S|^2} - C_\mu k\omega + \nabla\cdot[(\nu+\sigma_k(k/\omega))\nabla k],\\ \frac{D\omega}{Dt} &= 2C_{\omega 1}|S|^2 - C_{\omega 2}\omega^2 + \nabla\cdot[(\nu+\sigma_\omega(k/\omega))\nabla\omega].\end{aligned} \tag{2.9}$$

The standard constants are invoked,

$$C_\mu = 0.09, \qquad \sigma_k = 0.5, \qquad \sigma_\omega = 0.5,$$

$$C_{\omega 1} = 5/9, \qquad C_{\omega 2} = 3/40.$$

By using the same eddy viscosity (equation 2.8) in the momentum equation and the production term, the latter retains its usual meaning of energy transfer from the resolved field to k.

So, another interpretation of the present approach is that the *production rate* is clipped, rather than the original DES approach of clipping the *dissipation rate*. To highlight this, the $k-\omega$ SST based DDES formulation (Gritskevich et al. (2012)) is shown below:

$$\frac{Dk}{Dt} = P_k - \boldsymbol{\sqrt{k^3}/l_{DDES}} + \nabla\cdot[(\nu+\sigma_k\nu_{T_{RANS}})\nabla k], \tag{2.10}$$

$$\begin{aligned}\frac{D\omega}{Dt} &= \frac{\alpha P_k}{\nu_{T_{RANS}}} - \beta\omega^2 + \nabla\cdot[(\nu+\sigma_\omega\nu_{T_{RANS}})\nabla\omega]\\ &\quad + 2(1-F_1)\sigma_{\omega_2}\frac{\nabla k\cdot\nabla\omega}{\omega},\end{aligned} \tag{2.11}$$

where

$$\nu_{T_{RANS}} = \frac{a_1 k}{\max(a_1\omega, F_2 S)}.$$

The definitions of the several variables involved such as P_k, F_1 etc can be found in Gritskevich et al. (2012). We note that the DDES length scale l_{DDES} is used to clip the dissipation term of the $k-$equation with the eddy viscosity retaining the RANS definition, whereas in the current approach, l_{DDES} is used to define the eddy viscosity, which in turn clips the production term of the $k-$equation.

From a modeling perspective, limiting either the dissipation term or the production term achieves similar objectives. If we consider a flowfield resulting from a RANS simulation, the entire eddy viscosity field would be the modeled effect of all the turbulent scales. DES limits this modeled component, which allows for unsteadiness to develop as part of the flow solution (either due to a flow instability or due to initial/boundary conditions). This was achieved by enhancing the destruction term of the model equations, based on the DES clip. In the current formulation, this is achieved by limiting the production term instead. A comparison between these two approaches is dealt with in §2.3.1.

In the original DDES formulation

$$\Delta = h_{max} \equiv \max[\Delta_x, \Delta_y, \Delta_z].$$

However, based on previous studies (Breuer et al. (2003); Shur et al. (2008); Deck (2012)) it is clear that a different length scale definition needs to be used in the eddying region. We have found that the LLM issue (§2.3.1) is alleviated by redefining Δ as

$$\Delta = f_d V^{1/3} + (1 - f_d) h_{max}, \tag{2.12}$$

where V is the cell volume. In the eddy simulation region $f_d = 1$ and this gives $V^{1/3}$ — as is used in LES. Switching from h_{max} near the wall to $V^{1/3}$ farther out reduces ℓ_{DDES} and hence the eddy viscosity. That allows the resolved eddies to develop at small scales. This is the definition of Δ used for all the cases presented herein.
Rather than equation (2.12), if we simply used

$$\Delta = V^{1/3}, \tag{2.13}$$

we would still achieve our goal, in the sense that the model will be using $V^{1/3}$ as the length scale in the eddying region, for $f_d = 1$. The difference between equations (2.12) and (2.13) lies in the region where $0 < f_d < 1$, which lies towards the edge of the boundary layer. In this region, eqn. (2.12) uses a blend of h_{max} and $V^{1/3}$, resulting in a larger value of Δ than when using eqn. (2.13), which leads to a larger value for ν_T. Hence in the absence of turbulent velocity fluctuations to balance this reduction in the eddy viscosity, eqn. (2.13) would lead to lower ν_T values, and consequently, lower skin-friction.

A prime example of such a scenario would be the flow over a flat plate. Figure 2.1 shows the C_f distribution obtained using both equations (2.12) and (2.13), compared with the RANS

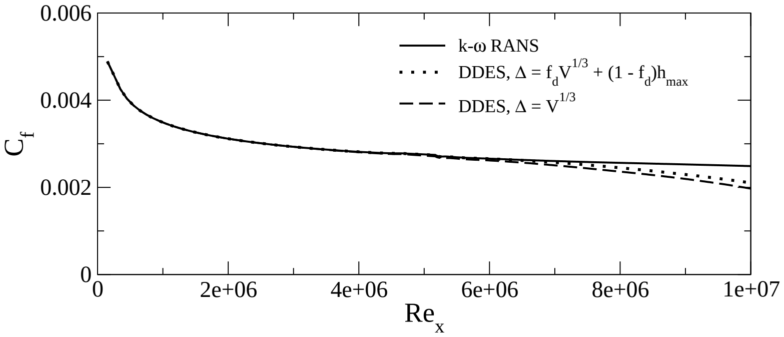

Figure 2.1: Distribution of the skin-friction co-efficient C_f for a flat plate: Solid line - $k-\omega$ RANS (Wilcox (1993)), Dotted line - current DDES with eqn. (2.12), Dashed line - current DDES with eqn. (2.13)

prediction. The mesh used here was constructed such that $h_{max} \approx \delta$ (δ being the boundary layer thickness at $Re_x = 10^7$) upto $Re_x = 5 \times 10^6$, after which the cell spacing was changed such that $h_{max} \approx 0.2\delta$. This corresponds to an "ambiguous" grid spacing (Spalart et al. (2006)), where MSD (and consequently GIS) could occur. It has been noted (Gritskevich et al. (2012)) that the shielding function f_d does not completely eliminate the issue of MSD. This leads to lower ν_T and hence, lower C_f. Hence eqn. (2.12) is used for all the cases presented here. To reiterate, the difference between using equations (2.12) and (2.13) arises only in the absence of turbulent fluctuations. For cases with unsteady flow fields (such as channel flow), they would both yield identical results.

The C_f prediction for the flat plate can be improved by increasing the extent of the shielded region (Gritskevich et al. (2012)). However tests on a flat plate boundary layer (fig. 2.2) show that values of 8 and 3 for the constants C_{d1} and C_{d2} in equation (2.6) provide adequate shielding, and hence those values were retained.

One final aspect related to the model formulation that needs to be explored is the sensitivity of the model to the value of the model constant C_{DES}. Using the length scale definition (2.12), simulations of channel flow were carried out for a range of values of the model constant C_{DES}. The results are summarized in fig. 2.3. This figure shows limited sensitivity to the exact value of C_{DES} used. Values within 50% of 0.12 produce similar mean velocities. Values as low as

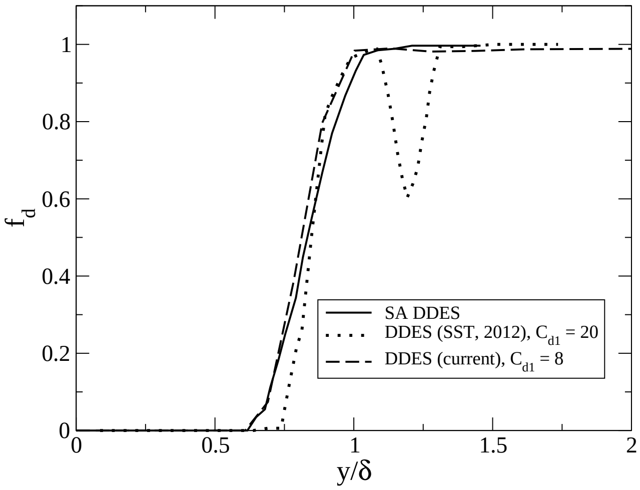

Figure 2.2: Comparison of the f_d shielding function for different models: Solid line - Spalart-Allmaras DDES (Spalart et al. (2006)), Dotted line - $k-\omega$ SST based DDES (Gritskevich et al. (2012)), Dashed line - current DDES based on $k-\omega$ model (Wilcox (1993))

0.03 and as high as 0.3 produce erroneous mean flow profiles because the RANS-to-eddying switch occurs too near, or too far from the wall.

2.3 Test Cases

2.3.1 Channel flow

Nikitin et al. (2000) attempted WMLES with the original DES in a channel flow with mixed results. Although it was shown that DES was capable of sustaining LES content, the resulting velocity profile contained two log-layers. Spalart et al. (2006) noted that the DDES formulation also exhibits LLM. Not surprisingly, when that same length scale formulation (except for a changed value of C_{DES}) is adopted for the present model, the same log-layer mismatch (LLM) is seen, as shown by the dashed line in fig. 2.4a; although, the mismatch is not as severe as was observed for other DDES models (Shur et al. (2008)). The solid line in that figure is the mean velocity profile obtained upon using equation (2.12); it is more consistent with the RANS profile. This length scale definition also exhibits better usage of the grid by the LES branch of the model, as shown in fig. 2.4b, where a larger portion of the Reynolds stress has been resolved, compared to the case with $\Delta = h_{max}$.

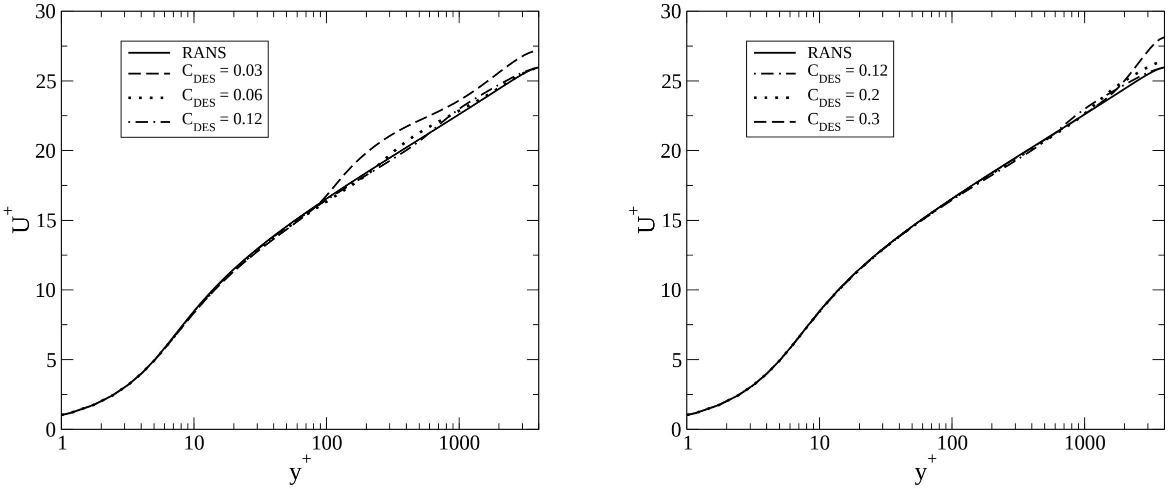

Figure 2.3: Velocity profiles obtained for different C_{DES} values in channel flow ($Re_\tau = 4,000$)

Further simulations of channel flow at different values of Re_τ were done with equation (2.12) and are shown in fig. 2.5. The velocity profiles are compared to the $k - \omega$ RANS model, and the agreement is quite good for all the cases.

In addition to correcting LLM, IDDES differs from DDES in the behaviour of the near-wall regions. Shur et al. (2008) noted that DDES tends to dampen the turbulent content at the RANS-LES interface, which IDDES corrected. In this regard, the current model is more akin to DDES rather than IDDES. Fig. 2.6a represents a wall-parallel plane just before the model switches from the RANS branch to the LES branch and it highlights the dampening effect of DDES at the RANS-LES interface. Fig. 2.6b represents a plane well inside the LES branch, where the turbulent content is better resolved. This region represents a location at which both DDES and IDDES are known to behave similarly (Shur et al. (2008)). The dampening effect of DDES can be seen in the variation of the RMS of velocity fluctuations (fig. 2.7), where the resolved velocity fluctuations obtained with the current DDES model for the case $Re_\tau = 2250$ have been compared to DNS data (Hoyas and Jiménez, (2006)) corresponding to $Re_\tau = 2003$. Overall, the resolved fluctuations are dampened near the RANS-LES interface (at $y/h \approx 0.1$), although the streamwise fluctuations slightly overshoots the DNS values locally. The near-wall peaks are not resolved since the model is in RANS mode, and the major contribution to the Reynolds stress would be due to the modeled component (i.e. the eddy viscosity).

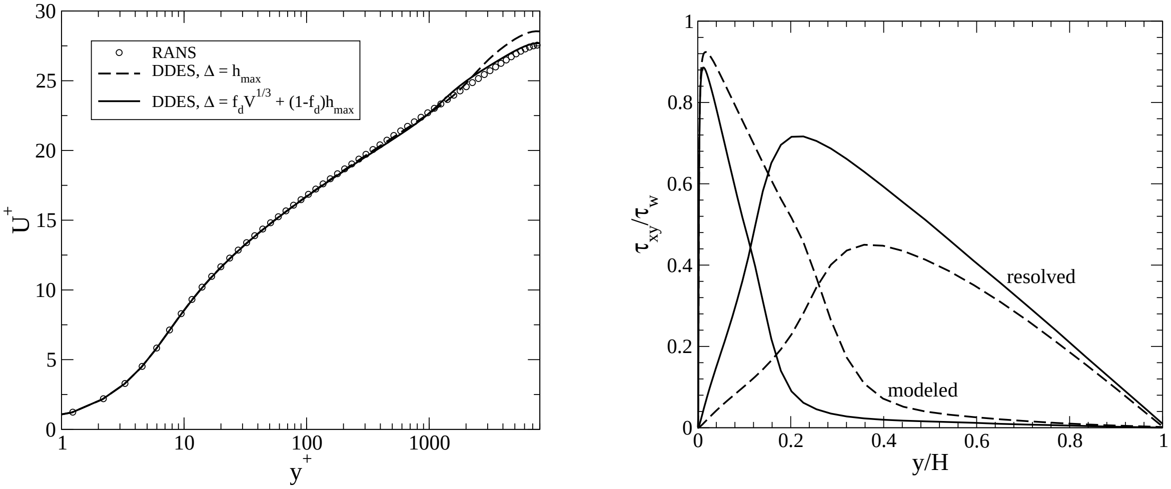

(a) Non-dimensionalized mean velocity profiles

(b) Modeled and resolved shear stress variation

Figure 2.4: Dashed line - $\Delta = h_{max}$; Solid line - $\Delta = f_d V^{1/3} + (1 - f_d)h_{max}$; H - channel half-width, $Re_\tau = 8000$

It was stated in the previous section that using the DES clip to limit either the production or the dissipation term achieves similar objectives. Towards this end, an additional channel flow simulation was carried out such that l_{DDES} now clips the dissipation term, leading to the model formulation shown below (similar to Gritskevich et al. (2012)):

$$\frac{Dk}{Dt} = 2\nu_T|S|^2 - \frac{\sqrt{k^3}}{l_{DDES}} + \nabla \cdot [(\nu + \sigma_k(k/\omega))\nabla k].$$

Accordingly, l_{RANS}, ν_T and C_{DES} were redefined

$$l_{RANS} = \frac{\sqrt{k}}{C_\mu \omega},$$
$$\nu_T = \frac{k}{\omega},$$
$$C_{DES} = 0.65,$$

with the other variable definitions (Δ, l_{LES} etc.) and the $\omega-$equation remaining unaltered. $C_{DES} = 0.65$ was chosen based on the original DES recommendations (Spalart et al. (1997)). This formulation yields similar results as the current production-limited DDES, as can be seen from a comparison of the velocity profiles obtained using both approaches (fig. 2.8). Additionally, the instantaneous vorticity field, as in fig. (2.6), obtained (not shown here) is also similar to the production-limited case.

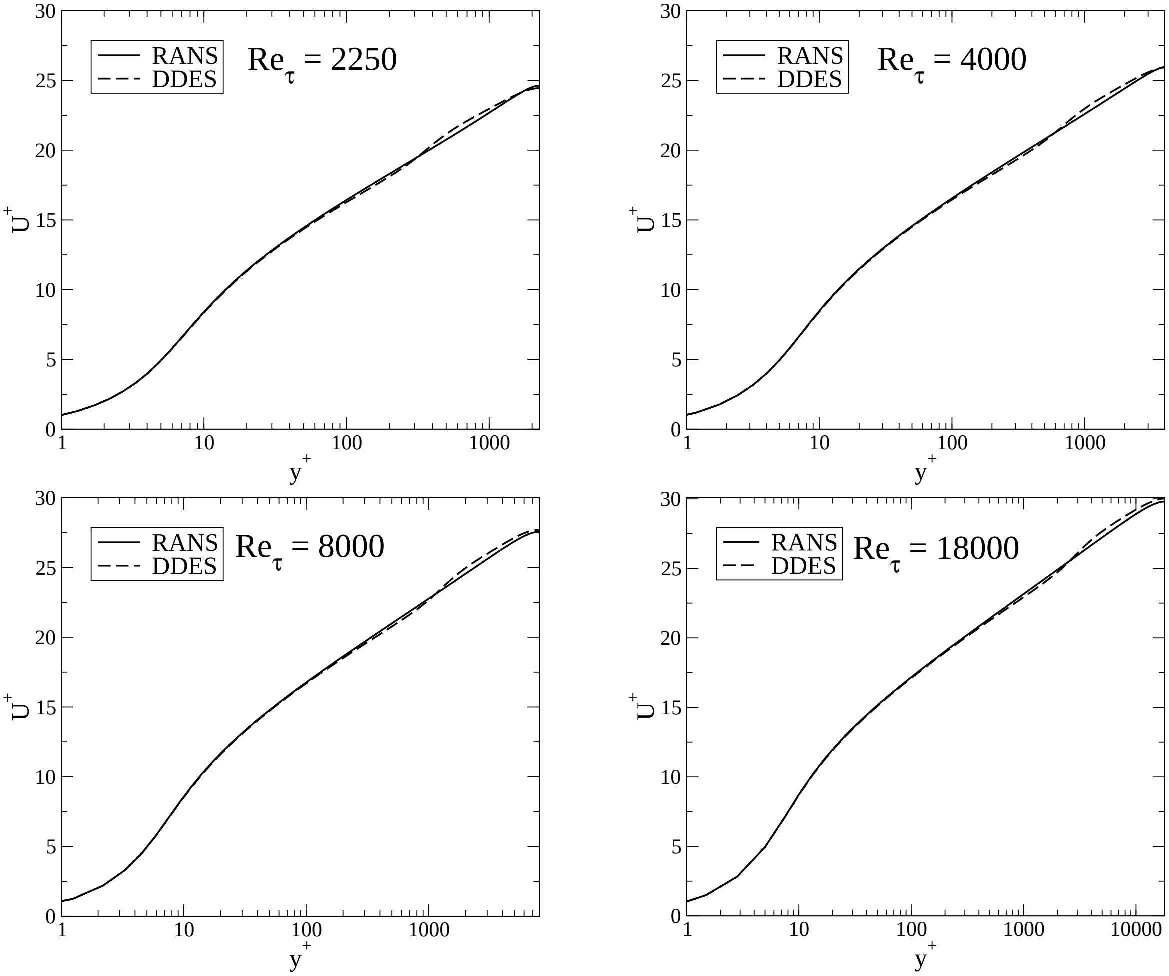

Figure 2.5: U^+ profiles for channel flow at different Re_τ

Overall, the current production-limited approach produces similar results as the original dissipation-limited approach. Hence our current approach can be viewed as an alternate formulation for DES.

The grid used for all the above simulations had $(\Delta x/H, \Delta z/H) = (0.1, 0.05)$ with about $750,000$ grid points. The extent of the computational domain is same as that described in Shur et al. (2008). The streamwise and spanwise cell spacing was kept the same for all simulations. In wall units, this corresponds to $(\Delta x^+, \Delta z^+) = (225, 112.5)$ for $Re_\tau = 2250$, $(\Delta x^+, \Delta z^+) = (400, 200)$ for $Re_\tau = 4000$, $(\Delta x^+, \Delta z^+) = (800, 400)$ for $Re_\tau = 8000$, and $(\Delta x^+, \Delta z^+) =$

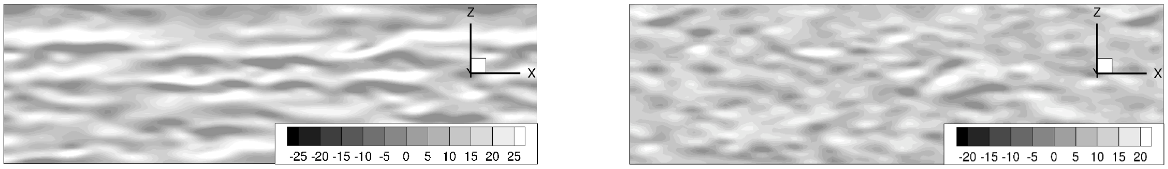

(a) $y/H = 0.1$ (b) $y/H = 0.8$

Figure 2.6: Contours of y-component of vorticity along XZ planes in the channel; $Re_\tau = 4000$

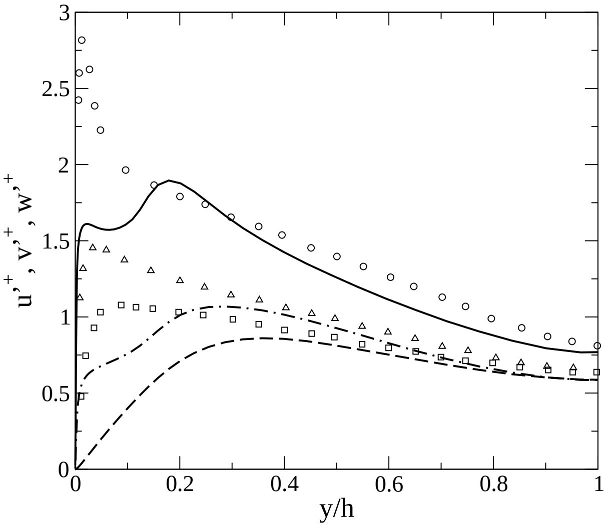

Figure 2.7: Profiles of resolved u'^+, v'^+ and w'^+ for channel flow. Symbols - DNS data: $Re_\tau = 2003$, ○ - u'^+, □ - v'^+, △ - w'^+. Lines - current DDES: $Re_\tau = 2250$, Solid line - u'^+, dashed line - v'^+, dot-dashed - w'^+.

$(1800, 900)$ for $Re_\tau = 18000$. The wall-normal grid spacing was adjusted such that $\Delta y^+ < 1$ at the wall for each simulation. The maximum local CFL number over the entire domain was ≈ 0.5

2.3.2 Flow over backward facing step

For the model developed herein to predict separated turbulent shear layers, the switch from the RANS branch to the Eddy Simulation branch must trigger eddying abruptly. Flow over a backward facing step is a critical test case. The attached boundary layer prior to the step and the boundary layer on the entire opposite wall should be in RANS mode, and the model should switch to eddying mode immediately after the flow separates. Here, the experiment of Vogel and Eaton (1985) has been simulated. The inflow Reynolds number based on the bulk

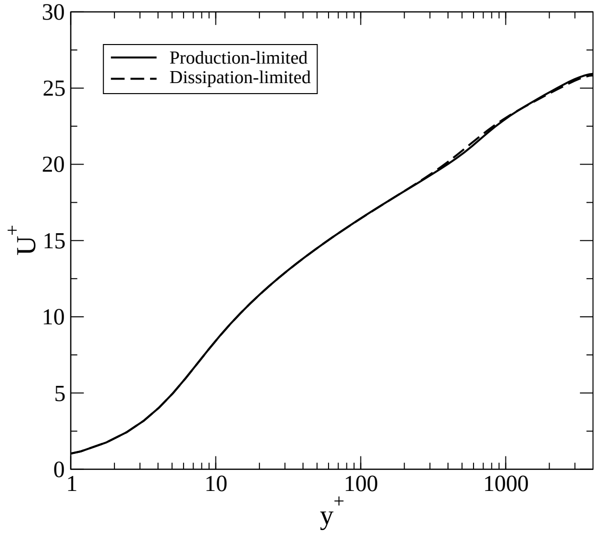

Figure 2.8: Comparison of U^+ for production-limited and dissipation-limited DDES: $Re_\tau = 4000$

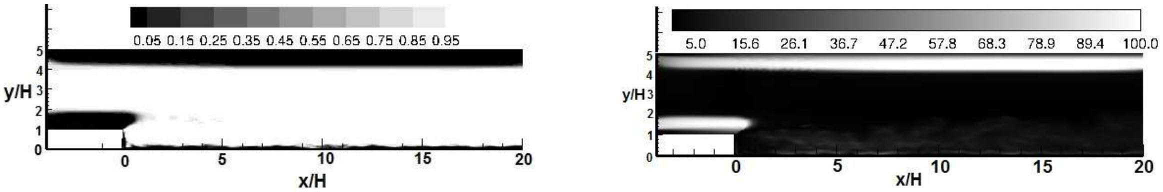

(a) f_d function contour

(b) ν_t/ν contour

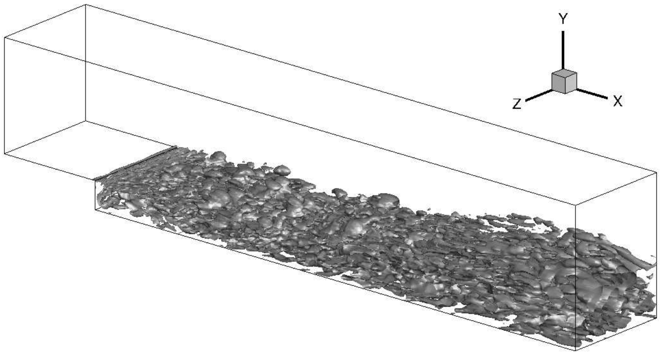

(c) Iso-surface of Q-criterion = $2500[s^{-2}]$

Figure 2.9: Flow over backward-facing step: Model switches to eddying mode at step and eddies are formed.

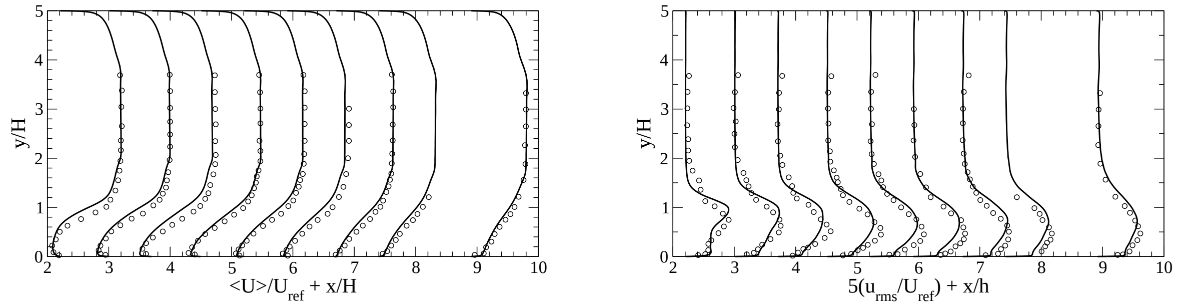

(a) Normalized $< U >$ profiles

(b) Normalized u_{rms} profiles

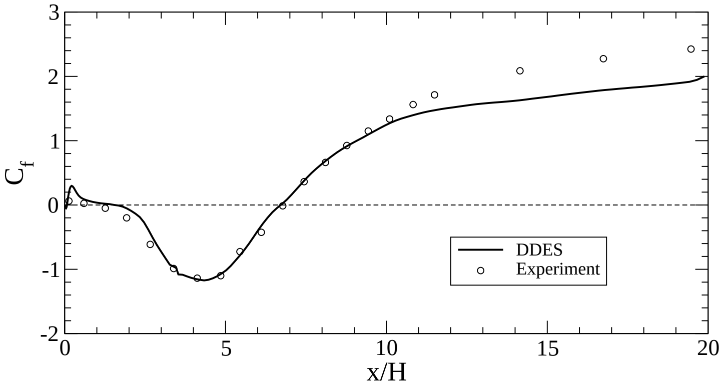

(c) Post-step $C_f \times 1000$ distribution along the bottom wall

Figure 2.10: Flow over backward-facing step: Comparison with experimental data. Profiles taken at x/H = 2.2, 3, 3.7, 4.5, 5.2, 5.9, 6.7, 7.4, 8.9

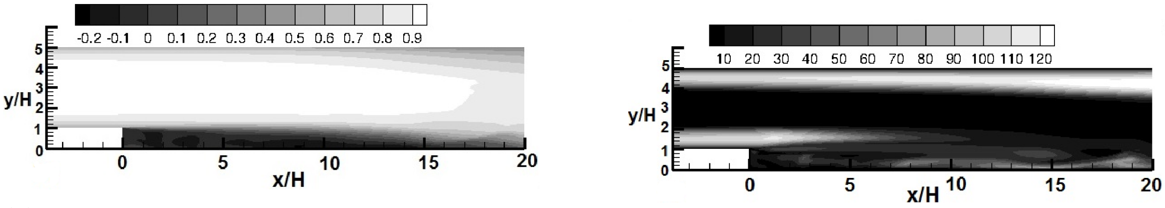

(a) Contours of instantaneous streamwise velocity normalized by U_{ref}

(b) Contours of ν_t/ν

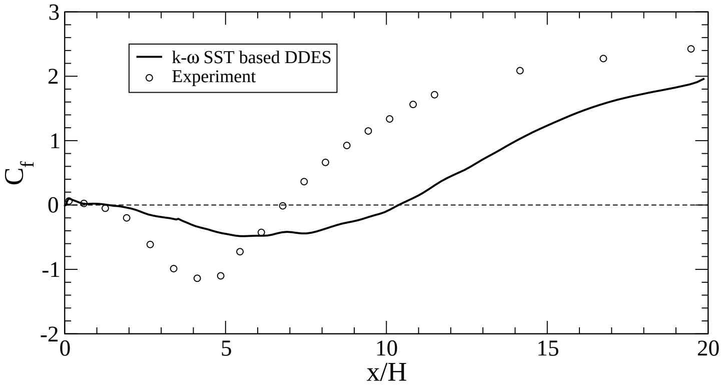

(c) Post-step $C_f \times 1000$ distribution along the bottom wall

Figure 2.11: Flow over backward-facing step: Simulation data from $k - \omega$ SST based DDES (Gritskevich et al. (2012))

velocity and step-height H is 28,000. As in previous simulations of this case (Spalart et al. (2006); Gritskevich et al. (2012)), the channel height and length before the step are 4H and 3.8H respectively. Post-step, the channel length is 20H. The spanwise domain size is 4H. The mesh consists of 1.1 million cells with 40 cells spaced uniformly along the spanwise direction. Grid points are clustered near the walls and also near the step, with about $40 - 50$ points distributed (in the wall-normal direction) over the post-step shear layer region alone. The CFL number over the entire domain was less than one, with a maximum local value of CFL ≈ 0.7 occurring at the vicinity of the step, where the streamwise cell spacing is minimum. RANS profiles of velocity, k and ω, obtained from a boundary layer calculation, were specified at the inlet. A constant pressure was specified at the outflow, and periodicity was enforced across the span. No perturbations were added to the inlet profiles, so unsteadiness arises due to the inherent shear-layer instability after the step.

Fig. 2.9a, which is a contour of the f_d variable, shows that the model stays in RANS mode for the attached boundary layers before the step ($x/H < 0$, $y/H = 1$) and along the entire opposite wall ($y/H = 5$) and switches to eddying immediately after the flow separates. The dark contours delimit the RANS regions.

The unsteadiness after the step is apparent in both the eddy viscosity field (fig. 2.9b) and Q-criterion (fig. 2.9c). In the eddying region, the subgrid viscosity drops to values on the order of 20 or less, similar to well-resolved LES.

The simulation data are in good agreement with the experimental results, as shown in fig. 2.10a, 2.10b and 2.10c, where the mean velocity, the rms velocity profiles at various streamwise locations and the C_f distribution along the bottom wall are plotted.

For the same grid and flow conditions, a simulation was carried out using the $k-\omega$-SST based DDES model (Gritskevich et al. (2012)). Fig. 2.11a shows the instantaneous velocity contours, which reveals that there are no turbulent eddies being formed after the step. Therefore, there is too little turbulent transport of momentum in the wall-normal direction, thus resulting in the flow remaining separated for a longer distance, as shown in fig. 2.11c. One possible reason as to why no eddies are forming can be gleaned from fig. 2.11b, which shows that, in the post-step shear layer, the eddy viscosity is quite high — comparable to the value seen in the pre-step boundary layer and along the top wall. This relatively high value of ν_T (compared to fig. 2.9b) would damp out any eddies that might form after the flow separates at the step. Thus, for a relatively coarse LES mesh where a significant portion of the turbulent scales in the inertial range would be filtered out, using $\Delta = h_{max}$ tends to overestimate the eddy viscosity value, leading to a damping of the large scale eddies which should've been resolved.

To further corroborate this view, a simulation was done with the $k-\omega$-SST based DDES model (Gritskevich et al. (2012)) while using Δ from equation (2.12) rather than h_{max} (results not shown here). That was found to produce eddies after the step, which suggests that the definition of Δ plays an important role. However, the Gritskevich *et al.* model might additionally require some recalibration for a different length scale definition, which is not our present purpose.

2.3.3 Flow over 2D periodic hills

This case consists of flow separation from a smooth surface unlike the backward-facing step. The geometry and flow conditions are described in the LES setup of Froehlich et al. (2005). The computational domain is 9H along the streamwise direction and 4.5H along the spanwise direction, where H is the hill height. The Reynolds number based on the hill height H and the bulk velocity measured at the crest of the hill is $10,595$. Periodic boundary conditions are specified along streamwise and spanwise directions, and the no-slip condition is imposed on the top and bottom walls. The mesh used for the simulation consists of 1.5 million cells. The cell spacing is uniform in both the streamwise and spanwise directions. A maximum local CFL number < 0.5 was maintained over the entire domain.

Results from the simulation are compared with the LES data of Froehlich et al. (2005). The skin-friction distribution along the bottom wall, and normalized mean velocity and fluctuation profiles are shown in fig. 2.12a, 2.12b and 2.12c respectively. Overall, the agreement with the LES data is quite good. An exception occurs very near $x = 0$, where the present C_f is higher than the data. This local discrepancy might be attributable to the uniform cell spacing that we used in the streamwise direction: in a recent LES study, Breuer et al. (2009) suggests using a finer streamwise spacing near the hill crests, relative to the cell spacing at the trough.

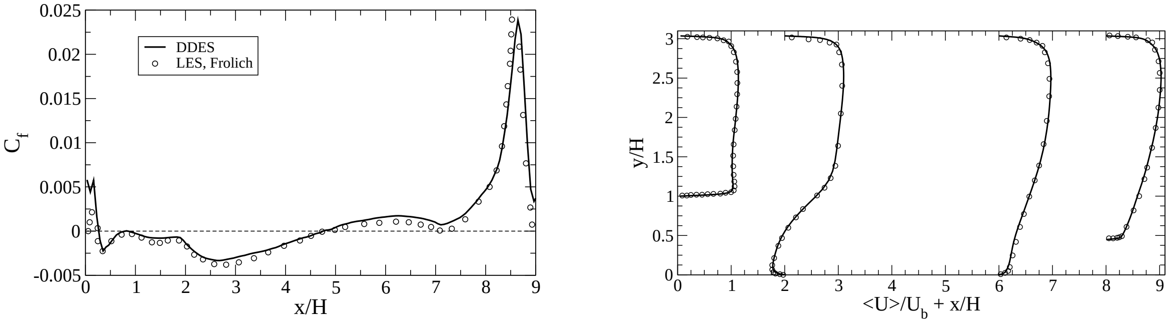

(a) Variation of the skin-friction coefficient along the bottom wall

(b) Normalized mean velocity profiles

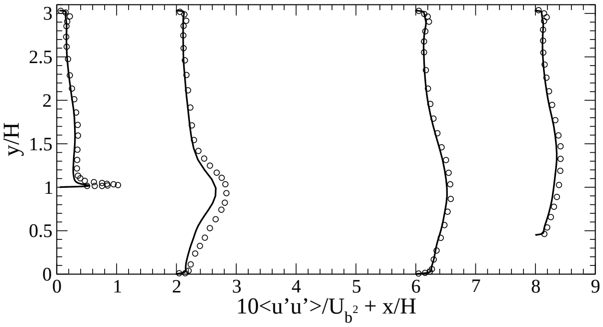

(c) Normalized $< u'^2 >$ profiles

Figure 2.12: Flow over 2D periodic hills: Velocity profiles taken at x/H = 0.05, 2, 6, 8

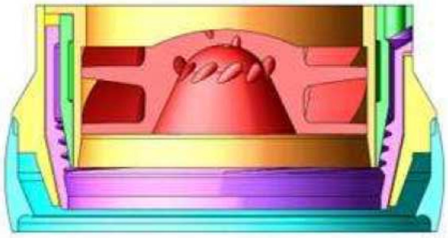

Figure 2.13: Atomizer geometry. Swirl is created by angled entrance slots near the center; slots at the side inject air without swirl.

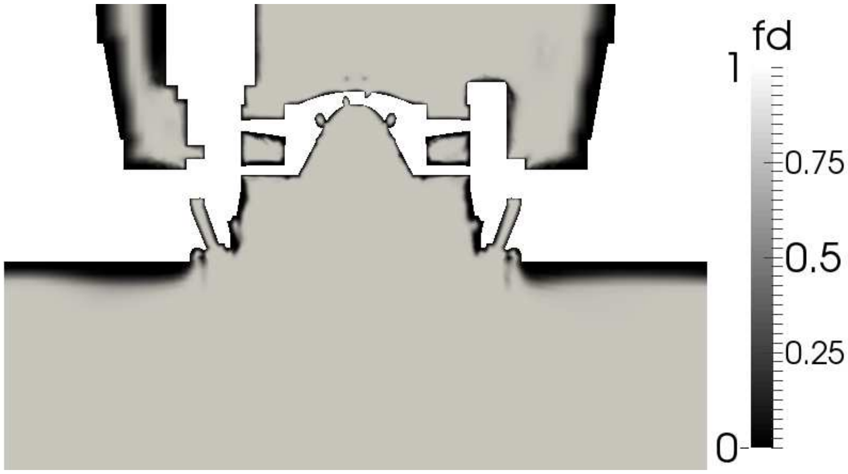

Figure 2.14: Contour of f_d obtained with the current DDES model. Model is in RANS mode near walls, and in LES mode away from walls.

2.3.4 Flow through an air blast atomizer

As an instance of the type of geometries commonly encountered in practical engineering applications, we consider the air pathways through a pure air-blast fuel injector for jet engines. The atomizer geometry is that of Pack et al. (2013). The nozzle is shown in fig. (2.13). A coaxial jet is created with a swirling central stream and a non-swirling outer stream. 40% of the flow goes through the angled guide vanes at the center, while 60% enters through slots near the outer radius. The flow downstream is a co-axial jet with a swirling core.

This case provides a complex, three-dimensional geometry to test the overall robustness of the current DDES model. It provides many complex flow characteristics, including abrupt flow separations and wakes, swirl-stabilized recirculation zones, and regions of high shear with eddying structures.

Pack et al. (2013) compared PIV measurements of air flow through the atomizer to RANS predictions of the $k-\omega$ SST and the RNG $k-\epsilon$ models. The flow fields predicted by these models were in reasonable agreement with the data, but closer comparisons are desired.

For the present simulations, an unstructured, 12 million cell mesh was created, with the extent of the computational domain as in Pack et al. (2013). The mesh is primarily hexahedral. Grid points were clustered within and immediately following the nozzle passages, with

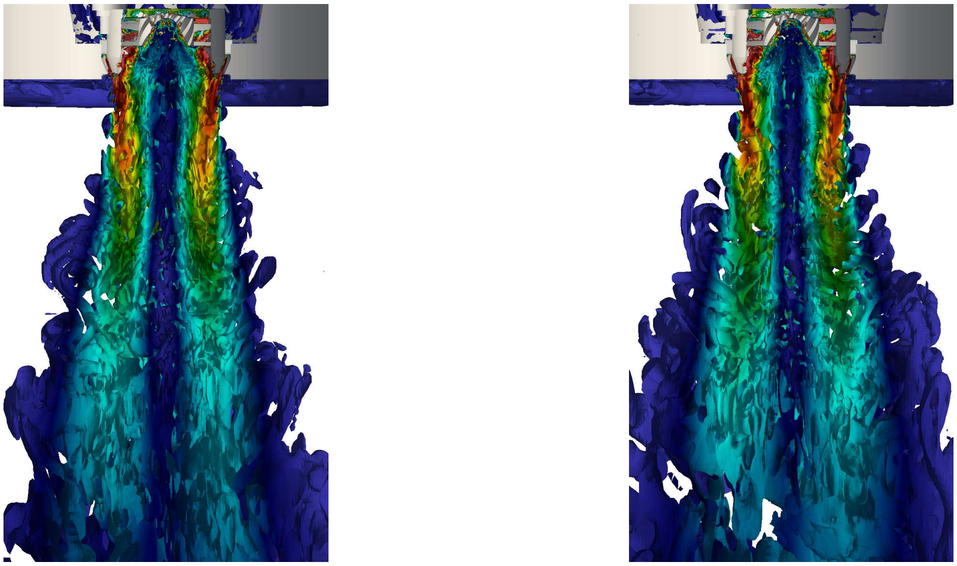

Figure 2.15: Iso-surface of Q-contours colored by velocity magnitude, comparing dynamic Smagorinsky LES (left) and current DDES (right).

256 points along the circumference of the nozzle. CFD simulations were carried out using the current DDES model, the standard Smagorinsky LES model (with Van Driest damping) and the dynamic Smagorinsky LES model (Lilly (1992)), as implemented by Jeyapaul (2011). The flow configuration here corresponds to the 4% ΔP pressure configuration in Pack et al. (2013).

Figure 2.14 shows the variation of f_d along a central plane. $f_d = 1$ immediately after the flow exits the nozzle, which allows the model to switch to LES, and subsequently generate unsteady flow content. Figure (2.15) consists of Q-surfaces colored by mean velocity magnitude comparing dynamic Smagorinsky LES to DDES. These images show how the DDES is producing as much small scale structure as an LES on the same grid. A plenum of low speed air feeds the nozzle from the top of the image shown in fig. 2.15. Within the internal passages of the nozzle, where the nearby walls influence the flow, the DES model is in RANS mode. In the jet, it is in eddy simulation mode.

The swirler vane passages imprint lobes on the velocity field, that rotate with downstream distance, due to the swirl. Fig. (2.16) illustrates this by Q contours of the steady, RANS solution. The lobes can be seen at the left side of the figure, about at the radius of the nozzle.

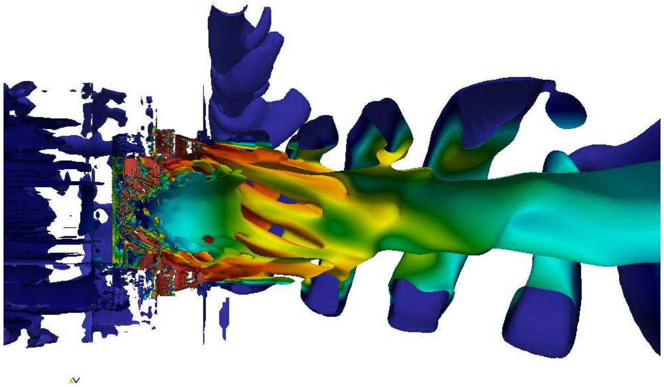

Figure 2.16: Swirling jet portrayed by Q-contours of the RANS computation.

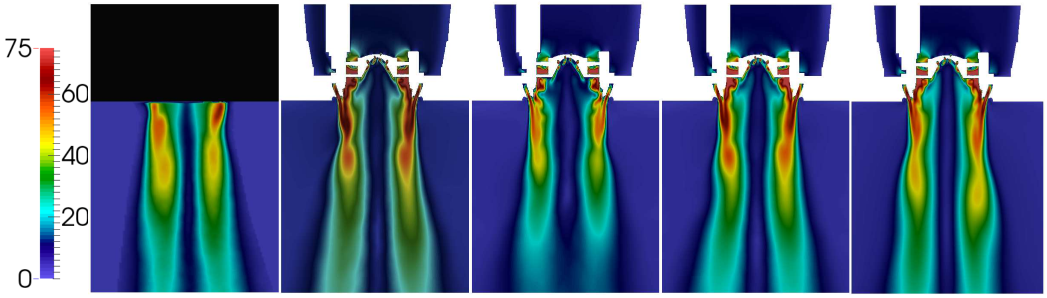

Figure 2.17: Contours of velocity magnitude along the axial plane of the atomizer. *Left to right:* PIV, current DDES, Smagorinsky LES, dynamic Smagorinsky and $k-\omega$ SST RANS. (Top of the PIV plane is within $1mm$ from atomizer tip)

A Q surface at larger radius swirls around the downstream jet. It has been cut to create this view, but it encircles the entire central contour.

Fig. (2.17) shows an axial slice through center plane of the nozzle. It extends from $1mm$ to $51mm$ below the tip. The PIV measurements at left are followed by the current DDES, Smagorinsky LES, the dynamic Smagorinsky model, and the SST RANS model. It is interesting to note that the DDES and dynamic Smagorinsky models actually seem to be closer to the PIV data than the Smagorinsky LES model; the high velocity contours extend further from the nozzle and are in better agreement with the PIV contours.

In this view the steady RANS prediction is quite good. In fig. (2.18) it will be seen to be a bit too diffusive.

Fig. (2.18) is a cross section perpendicular to the nozzle axis, located $12.5mm$ downstream of the nozzle exit. The PIV contours contain 8 lobes which correspond to the 8 slots of the

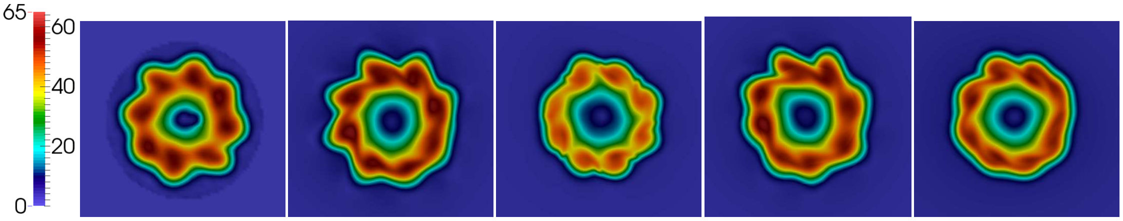

Figure 2.18: Contours of velocity magnitude along a radial plane located 12.5mm from the tip of the atomizer. *Left to right*: PIV, current DDES, Smagorinsky LES, dynamic Smagorinsky and $k-\omega$ SST RANS.

outer air passages. The velocity contours predicted by RANS show the lobes are dissipated, while the LES and DES results resolve them. However, the maximum velocity contour level for the Smagorinsky LES is noticeably lower than the PIV. The DDES and dynamic Smagorinsky are producing about the same maximum velocity as the PIV.

In some cases RANS shows 9 or 10 lobes, instead of 8, which incorrectly corresponds to the 10 slots of the inner air swirler – or a combination of the inner and outer air passages. Figure 2.19 shows the velocity profiles computed for the different CFD simulations, compared with the PIV data. Clearly, the Smagorinsky LES predicts a lower velocity than DDES or dynamic Smagorinsky (fig. 2.19a). Table 1 shows the computed mass flow rates for the PIV and all the CFD simulations. The Smagorinsky LES produces a significantly lower mass flow, leading to the lower velocity predictions seen in figure 2.19. The poor prediction by Smagorinsky LES is likely an indirect effect of coarseness of the mesh in the internal passages, and the validity of the Van Driest damping function in these regions.

Table 2.1: Measured mass flow rates for PIV and CFD simulations

	$\dot{m}$ (kg/s)	Error %
PIV	0.010422	
DDES	0.010267	1.49
Smagorinsky LES	0.008456	18.9
dynamic Smagorinsky	0.010119	2.9
$k-\omega$ SST RANS	0.01022	1.9

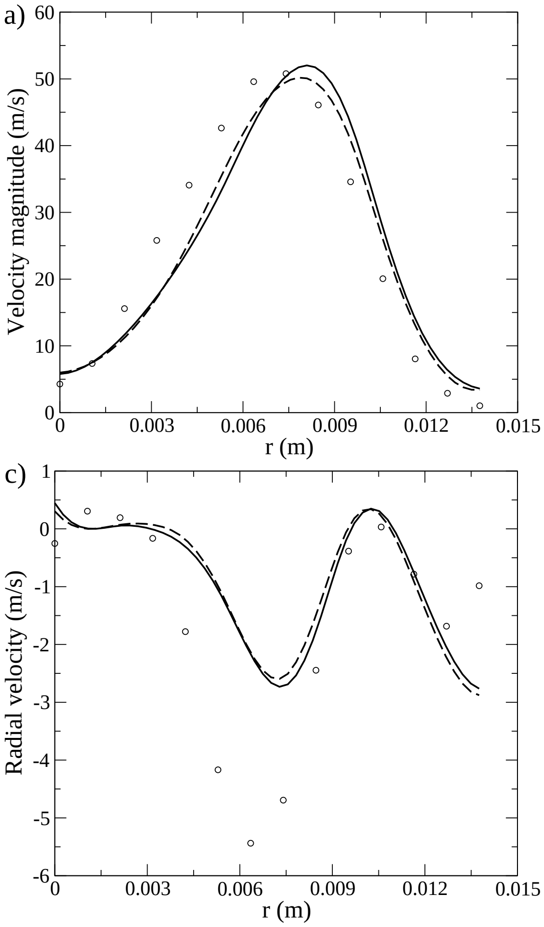

Figure 2.19: Velocity profiles along a radial plane 12.5mm downstream of atomizer tip. Circle - PIV, solid line - current DDES, dotted line - Smagorinsky LES, dashed line - dynamic Smagorinsky LES, dot-dashed line - $k-\omega$ SST RANS. (a) Total velocity magnitude, (b) Axial velocity component, (c) Radial velocity component, (d) Tangential velocity component.

Although the prediction of the total velocity magnitude by DDES and dynamic Smagorinsky is close to the PIV data (fig. 2.19a), there is some error in the location of the peak velocity along the radial direction. This would be primarily due to the under-prediction of the radial velocity component (fig. 2.19c), leading to a "thicker" jet in the CFD simulations than in the experiment.

Hence overall, the DDES results agree with data in terms of flow structure and velocity magnitudes. Additionally, a key observation to be made here is that DDES produces results as accurate as the dynamic Smagorinsky LES. The strength of the present DDES model is illustrated in this complex engineering flow, in that it has resolved the flow field more accurately than RANS, and as accurately as the dynamic Smagorinsky LES.

2.4 Conclusion

The present approach is a variation on the DDES theme: the DDES length scale used for the dissipative term in previous models was adopted for the $\ell^2\omega$ eddy viscosity, with the model constant C_{DES} being recalibrated. This led to a formulation based on limiting the production term, rather than the original DES approach of enhancing the dissipation term. Preliminary tests on a channel flow seem to suggest that both formulations are equivalent. The shielding function f_d from the original DDES formulation (Spalart et al. (2006)) was found to provide adequate shielding and thus the same function was used herein. Redefining the grid dimension Δ, helps to overcome the LLM issue, without having to use any additional empirical functions (as is used in IDDES). The current DDES model tends to dampen out fluctuations near the RANS-LES interface, which was observed in the original DDES as well (Shur et al. (2008)). In light of this, the current model needs to be tested on cases where flow separation is strongly dependent on the dynamics of the incoming boundary layer.

Simulations of flows over a backward-facing step, and over periodic hills showed that the model is capable of handling separation well. Specifically, the simulation of a flow over a backward facing step showed that the model was capable of switching between RANS and LES seamlessly and producing unsteady content after separation. Results obtained using the DDES model for flow through an atomizer indicate that the model is robust enough to be applicable to complex 3D geometries.

2.5 Acknowledgements

Computing resources were provided by Extreme Science and Engineering Discovery Environment (XSEDE), which is supported by National Science Foundation grant number OCI-1053575. Funding was provided by NASA grant NNX12AJ74A and by Pratt & Whitney. Reddy would like to thank Dr. S.K. Arolla for helpful OpenFOAM-related discussions.

CHAPTER 3. AN $\ell^2\omega$ FORMULATION OF DELAYED DETACHED EDDY SIMULATION

K. R. Reddy, J. A. Ryon, P. A. Durbin

Presented at the 10^{th} International ERCOFTAC Symposium on Engineering Turbulence Modelling and Measurements (ETMM-10)
Marbella, Spain, September 17-19, 2014

3.1 Introduction

Hybrid RANS/LES models are considered to have promise for industrial CFD applications, where the idea is to employ RANS in the near wall part of attached boundary layers, and eddy resolving simulation in regions away from the surface. Detached Eddy Simulation (DES) falls under this category of hybrid methods. DES was first proposed by Spalart et al. (1997) and since then, the method has undergone considerable revision. Menter and Kuntz (2002) pointed out that artificial Grid Induced Separation (GIS) could occur if, when the switch from RANS to Eddy Simulation took place, the reduction of eddy viscosity was not balanced by resolved turbulent content. This effect was termed Modeled Stress Depletion (MSD). Towards this end, the blending functions of the $k-\omega$ SST model were used as a "shield" to prevent the model from switching to eddy simulation within the lower part of the boundary layer. Following this, Spalart et al. (2006) introduced a generic shielding function, applicable to any RANS model, and the resulting formulation was termed Delayed DES (DDES) — although it might better be called shielded DES.

Another perspective on DES is that it has an ability to function as a type of Wall-Modeled LES (WMLES). Initial attempts to use the original DES as a WMLES formulation in a channel flow (Nikitin et al. (2000); Piomelli et al. (2003)) resulted in two, mismatched log-layers — one from the RANS branch, and the other from the eddy resolving branch. This anamoly was termed Log-Layer Mismatch (LLM) — an issue which is present in the DDES formulation as well.

Breuer et al. (2003) noted that $h_{max} = \max(dx, dy, dz)$ may not be a suitable length scale to use in the eddying regions of DES, and that using $V^{1/3}$ instead, where V is the cell volume, produced better results. The fact that a different length scale definition is required was also implied in a formulation termed Improved DDES (IDDES) (Shur et al. (2008)), which required the modification of the length scale definition to be used in the eddying region. In addition to revised length scales, more complex blending functions were introduced in order to ensure that the model performed adequately as a WMLES formulation. The blending functions in the IDDES formulation are responsible for allowing the LES functionality within the boundary layer in the presence of turbulent fluctuations, provided the grid is fine enough. And along with a modified length scale definition, they alleviate LLM seen in the channel flow. This is the key difference between DDES and IDDES.

Yet another variation of DES, known as Zonal DES or ZDES (Deck (2012)) also employs $V^{1/3}$ (or Δ_ω, which depends on the orientation of the vorticity ω as well as the local cell spacing) in the eddying region. However, as the name would suggest, ZDES requires the user to specify the RANS and eddying regions.

In the present article, a different variant of DDES is developed and applied to the $k-\omega$ model (Wilcox (1993)). The motive for the present approach is to make DES more similar to LES in the eddying region. It has been observed that LES often produces more accurate results than DES. Hence, our objective is to make use of DES to reduce near-wall grid requirements and, simultaneously, to make the eddy viscosity similar to the Smagorinsky formula far from the surface.

Rather than utilizing the length scale in the dissipation term of the k-equation, it is used to define the subgrid eddy viscosity, which is then used to define the production term. This definition of the eddy viscosity makes it a function of the length scale, similar to the definition used for the subgrid eddy viscosity in the Smagorinsky model. This definition additionally provides a method to estimate the value of the model constant by comparing it to the Smagorinsky eddy viscosity formulation. Hence the model can be viewed as a Smagorinsky DES model with $k-\omega$ as the underlying RANS model.

Additionally, the length scale is redefined to ameliorate the issue of LLM without requiring the blending functions of IDDES. The absence of any blending functions in the current formulation would indicate that the near wall behaviour of the current model is more similar to DDES than IDDES. The open source code OpenFOAM was used for all the present computer simulations. Gaussian finite volume integration with central differencing for interpolation, was selected for spatial discretization of equations. Time integration was by the 2^{nd} order, backward difference method. The resulting matrix system was solved using the Pre-conditioned Bi-conjugate gradient algorithm, with the simplified, diagonal-based, incomplete-LU preconditioner. Solution for the matrix system at each time step was obtained by solving iteratively, by specifying an appropriate tolerance for the residual norm.

3.2 Model Formulation

The original DDES formulation of Spalart et al. (2006) introduces a shielding function f_d defined as

$$\begin{aligned} f_d &= 1 - \tanh\left([C_{d1} r_d]^{C_{d2}}\right), \qquad C_{d1} = 8, \quad C_{d2} = 3, \\ r_d &= \frac{k/\omega + \nu}{\kappa^2 d_w^2 \sqrt{U_{i,j} U_{i,j}}}, \end{aligned} \tag{3.1}$$

where k/ω is the RANS eddy viscosity, ν the molecular viscosity, κ the von Kármán constant, d_w the distance to the wall, and $U_{i,j}$ is the velocity gradient tensor. f_d is used to define the DDES length scale

$$l_{DDES} = l_{RANS} - f_d \max(0, l_{RANS} - l_{LES}), \tag{3.2}$$

$$l_{RANS} = \frac{\sqrt{k}}{\omega}, \tag{3.3}$$

$$l_{LES} = C_{DES} \Delta. \tag{3.4}$$

The eddy viscosity is defined in terms of the length scale as

$$\nu_T = l_{DDES}^2 \omega. \tag{3.5}$$

$f_d = 0$ gives $\nu_T = k/\omega$ and the model operates in RANS mode. $f_d = 1$ and $l_{LES} < l_{RANS}$ gives $\nu_T = (C_{DES}\Delta)^2\omega$ and the model is fully in eddy simulation mode.
This definition of ν_T is used in the turbulent kinetic energy production term, leaving all the other terms unaltered.

$$\frac{Dk}{Dt} = \boldsymbol{2\nu_T|S|^2} - C_\mu k\omega + \nabla \cdot [(\nu + \sigma_k(k/\omega))\nabla k], \tag{3.6}$$

$$\frac{D\omega}{Dt} = 2C_{\omega 1}|S|^2 - C_{\omega 2}\omega^2 + \nabla \cdot [(\nu + \sigma_\omega(k/\omega))\nabla \omega]. \tag{3.7}$$

The standard constants are invoked,

$$C_\mu = 0.09, \qquad \sigma_k = 0.5, \qquad \sigma_\omega = 0.5,$$

$$C_{\omega 1} = 5/9, \qquad C_{\omega 2} = 3/40.$$

Dropping the transport terms in the ω equation yields

$$\omega^2 = \frac{2C_{\omega 1}}{C_{\omega 2}}|S|^2 = \frac{400}{27}|S|^2.$$

Then equation (3.5) becomes

$$\nu_T = (C_{DES}\Delta)^2 \frac{20}{3\sqrt{3}}\sqrt{|S|^2}.$$

The constant C_{DES} can be estimated by equating this to $(C_s\Delta)^2\sqrt{2|S|^2}$, which is the eddy viscosity formulation used in the Smagorinsky LES model. Using $C_s \approx 0.2$ yields $C_{DES} \approx 0.12$. This value of C_{DES} was found to be satisfactory in validation studies.

In the original DDES formulation

$$\Delta = h_{max} \equiv \max[\Delta_x, \Delta_y, \Delta_z].$$

We have found that the LLM issue is alleviated by redefining Δ as

$$\Delta = f_d V^{1/3} + (1 - f_d)h_{max}, \tag{3.8}$$

where V is the cell volume. In the eddy simulation region $f_d = 1$ and this gives $V^{1/3}$ — as is used in LES. Switching from h_{max} near the wall to $V^{1/3}$ farther out reduces ℓ_{DDES} and hence the eddy viscosity. That allows the resolved eddies to develop at small scales. This is the definition of Δ used for all the cases presented herein.

3.3 Test Cases

3.3.1 Channel flow

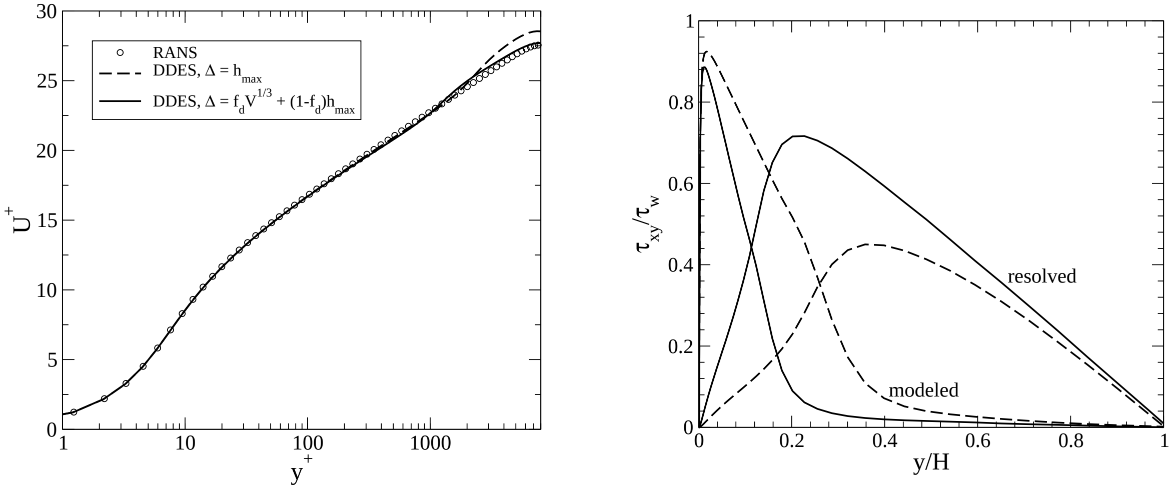

(a) Non-dimensionalized mean velocity profiles

(b) Modeled and resolved shear stress variation

Figure 3.1: Dashed line - $\Delta = h_{max}$; Solid line - $\Delta = f_d V^{1/3} + (1 - f_d)h_{max}$; H - channel half-width

As expected, using $\Delta = h_{max}$ shows the LLM issue (fig 3.1a). However, using equation (3.8) helps to alleviate the LLM and yields a velocity profile consistent with the RANS results. Additionally, as shown in fig (3.1b) a larger component of the reynolds stress is resolved by using equation (3.8).

3.3.2 Flow over a backward facing step

This is a key case since the model must be capable of immediately switching from RANS branch in the attached boundary layer pre-step to LES branch in the separated region post-step, which was found to be the case for the current DDES model. The experimental setup of Vogel and Eaton (1985) was simulated here. The mesh used had 1.1 million cells with 40 cells

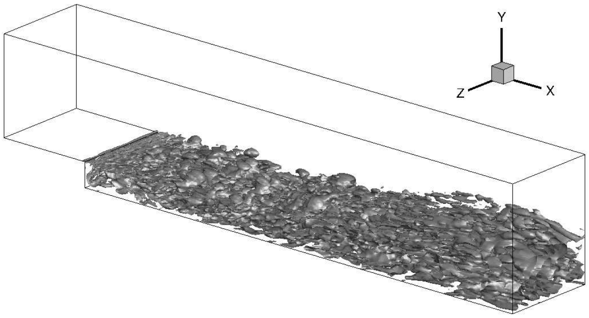

Figure 3.2: Iso-surface of Q-criterion = 2500[s^{-2}]

spaced uniformly along the spanwise direction. The unsteady flowfield after the flow separates from the step is apparent in figure 3.2 which shows the Q-criterion. Distribution of the post-step skin-friction coefficient along the bottom wall (fig. 3.3) shows very good agreement with the experimental data.

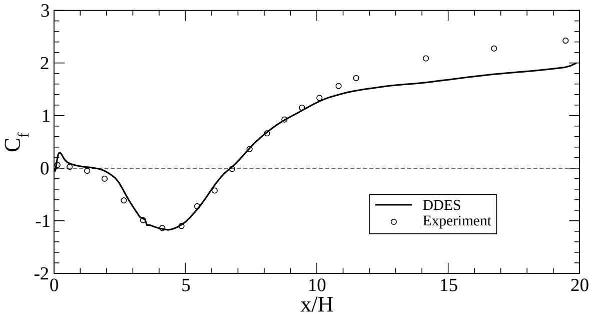

Figure 3.3: Post-step $C_f \times 1000$ distribution along the bottom wall

3.3.3 Flow over 2D periodic hills

This case consists of flow separation from a smooth surface unlike the backward-facing step. The geometry and flow configuration is as described by the LES setup of Froehlich et al. (2005). The computed skin-friction along the bottom wall has been compared with the LES data (fig 3.4). Overall the agreement is quite good except near the inlet where C_f has been slightly overpredicted. This can be attributed to the uniform grid spacing used in the mesh. A more recent LES study by Breuer et al. (2009) suggests using a finer spacing near the hill crests relative to the spacing near the troughs.

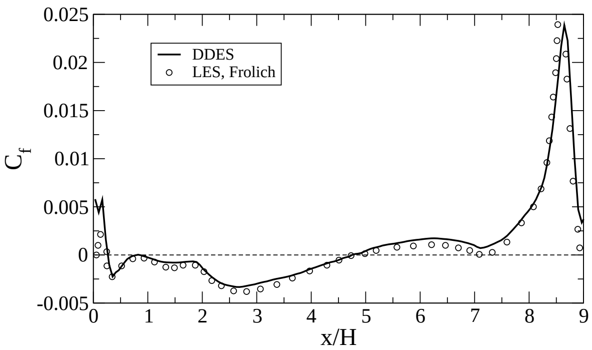

Figure 3.4: $C_f \times 1000$ distribution along the bottom wall

3.3.4 Flow through an air blast atomizer

The flow through a pure air-blast fuel injector is an instance of the type of geometries commonly encountered in practical engineering applications.

The geometry is described by Pack et al. (2013), where PIV measurements of air flow through the atomizer are compared to RANS predictions ($k - \omega$ SST and RNG $k - \epsilon$). The flow fields predicted by these models were in reasonable agreement with the data, but closer comparisons are desired.

For the present simulations, an unstructured, 12 million cell mesh was created.The mesh is primarily hexahedral. Grid points were clustered within and immediately following the nozzle passages, with 256 points along the circumference of the nozzle. CFD simulations were carried out using the current DDES model, the standard Smagorinsky LES model (with Van Driest damping) and the dynamic Smagorinsky LES model (Lilly (1992)), as implemented by Jeyapaul (2011). The flow configuration here corresponds to the 4% ΔP pressure configuration in Pack et al. (2013).

Fig (3.6) compares contours of the mean velocity magnitude obtained using both PIV and the current DDES model along an axial slice through the center plane of the nozzle (extending from 1mm to 51mm below the atomizer tip), while fig (3.7) shows the corresponding comparison along a radial plane located 12.5mm below the atomizer tip. The DDES model is able to properly resolve the 8 lobes (corresponding to 8 slots of air passages). This illustrates the overall robustness of the current DDES model.

Figure 3.8 shows the velocity profiles computed for the different CFD simulations, com-

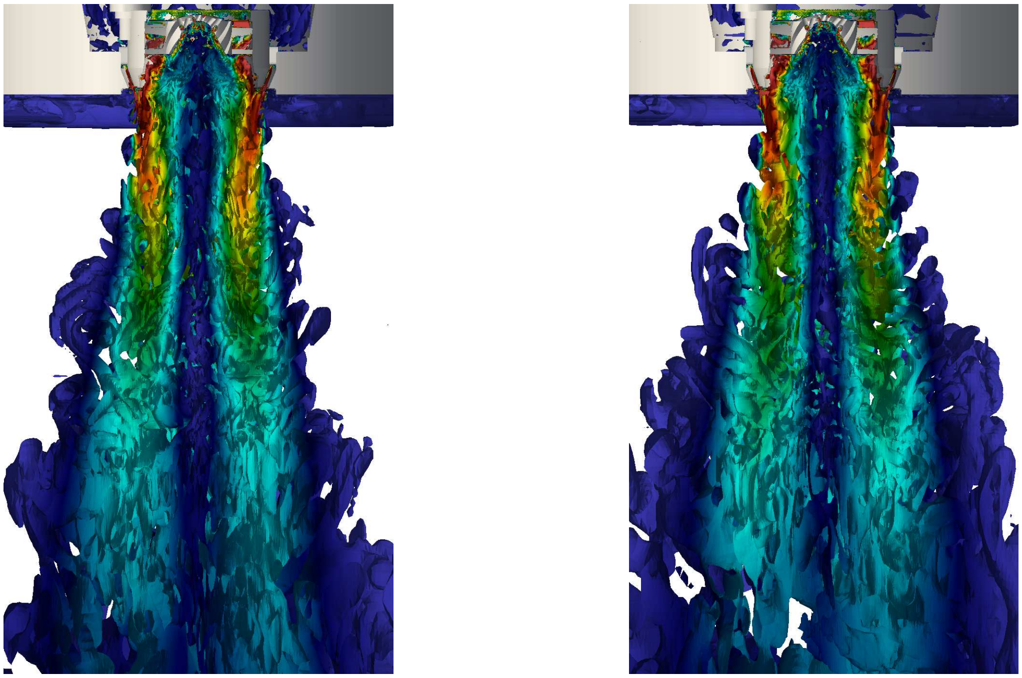

Figure 3.5: Iso-surface of Q-contours colored by velocity magnitude, comparing dynamic Smagorinsky LES (left) and current DDES (right).

pared with the PIV data. Clearly, the Smagorinsky LES predicts a lower velocity than DDES or dynamic Smagorinsky (fig. 3.8a). Table 1 shows the computed mass flow rates for the PIV

Table 3.1: Measured mass flow rates for PIV and CFD simulations

	$\dot{m}$ (kg/s)	Error %
PIV	0.010422	
DDES	0.010267	1.49
Smagorinsky LES	0.008456	18.9
dynamic Smagorinsky	0.010119	2.9
$k-\omega$ SST RANS	0.01022	1.9

and all the CFD simulations. The Smagorinsky LES produces a significantly lower mass flow, leading to the lower velocity predictions seen in figure 3.8. The poor prediction by Smagorinsky LES is likely an indirect effect of coarseness of the mesh in the internal passages, and the validity of the Van Driest damping function in these regions.

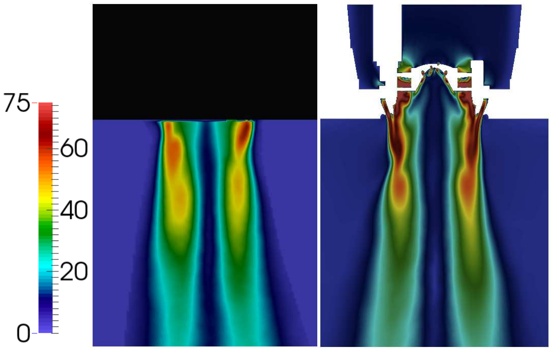

Figure 3.6: Contours of velocity magnitude along the axial plane of the atomizer obtained using PIV (left) and current DDES (right). (Top of the PIV plane is within $1mm$ from atomizer tip)

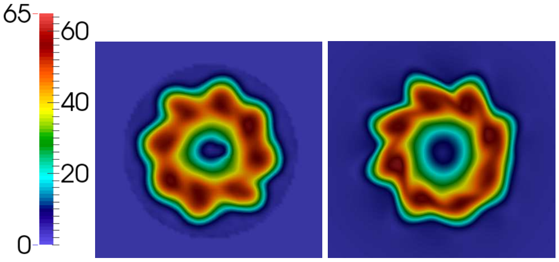

Figure 3.7: Contours of velocity magnitude along a radial plane located $12.5mm$ from the tip of the atomizer. Left - PIV, right - current DDES.

Although the prediction of the total velocity magnitude by DDES and dynamic Smagorinsky is close to the PIV data (fig. 3.8a), there is some error in the location of the peak velocity along the radial direction. This would be primarily due to the under-prediction of the radial velocity component (fig. 3.8c), leading to a "thicker" jet in the CFD simulations than in the experiment.

Hence overall, the DDES results agree with data in terms of flow structure and velocity magnitudes.

3.4 Implementation of Dynamic Procedure

For all the cases presented thus far, the current model formulation is able to produce results with adequate accuracy. It is well-known that the value of the Smagorinsky constant C_s varies

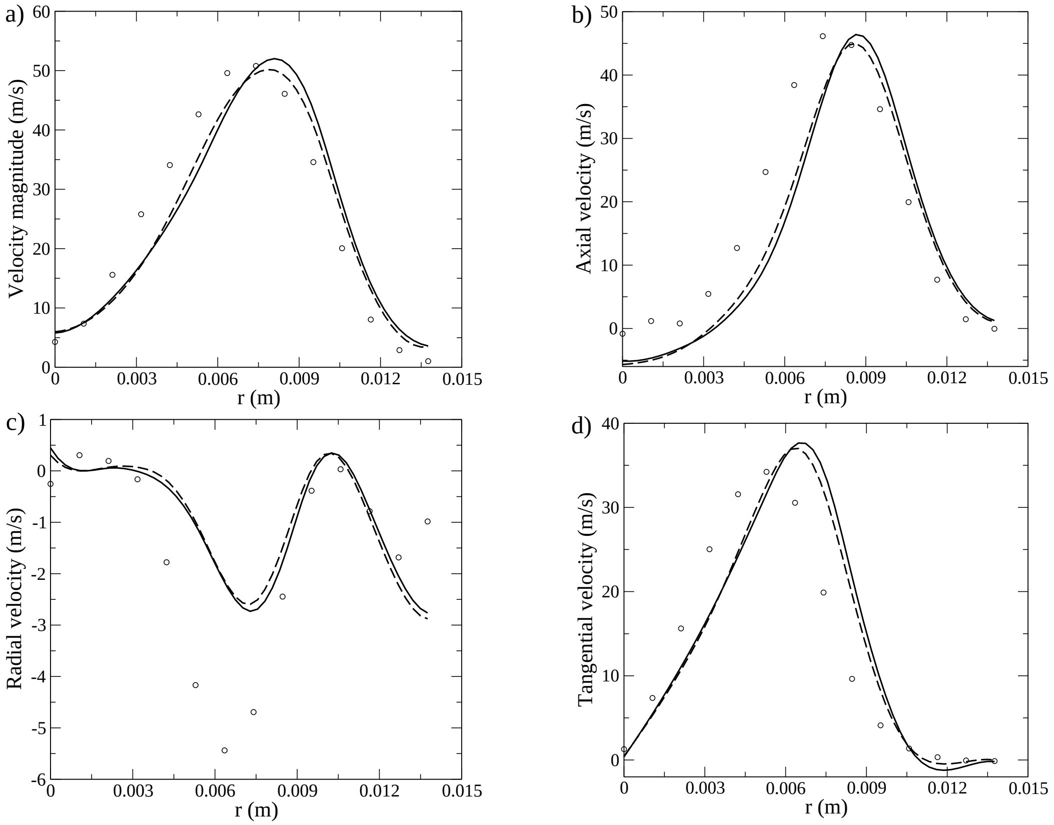

Figure 3.8: Velocity profiles along a radial plane 12.5mm downstream of atomizer tip. Circle - PIV, solid line - current DDES, dotted line - Smagorinsky LES, dashed line - dynamic Smagorinsky LES, dot-dashed line - $k-\omega$ SST RANS. (a) Total velocity magnitude, (b) Axial velocity component, (c) Radial velocity component, (d) Tangential velocity component.

from case to case (Germano et al. (1991)). This motivated the formulation of a dynamic procedure to compute C_s (Lilly (1992)). Since the current model constant C_{DES} is based on C_s, it is likely that the same weakness was also inherited, wherein different C_{DES} values might produce more accurate results for different cases. However, given the similarity of the current formulation to the Smagorinsky model, a dynamic procedure similar to that of Lilly (1992) can be implemented. This implementation will be shown in the next section, followed by results from a test case to highlight the improved accuracy obtained using the dynamic procedure.

3.4.1 Model formulation

The dynamic procedure of Lilly (1992) computes the value of C_s to be used in the Smagorinsky subgrid viscosity formula

$$\nu_{SGS} = (C_s \Delta)^2 |S|.$$

Likewise, the dynamic procedure can be used to compute the value of C_{DES} to be used in the eddy viscosity formula in the current model

$$\nu_T = (C_{DES} \Delta)^2 \omega.$$

This leads to

$$M_{ij} = \hat{\Delta}^2 \hat{\omega} \hat{S_{ij}} - \Delta^2 \widehat{\omega S_{ij}}, \qquad \hat{\Delta}/\Delta = 2, \tag{3.9}$$

$$\Rightarrow C_{DES}^2 = 0.5(L_{ij} M_{ij} / M_{ij}^2). \tag{3.10}$$

The definitions of L_{ij} and M_{ij} (except for using a different formulation for the eddy viscosity) are same as in Lilly (1992). The test filter is an average over neighboring cells, as is available in OpenFoam.

The value of the computed constant can become locally negative — this problem exists in LES as well. For our simulations we clipped C_{DES} to zero. So eqn. (3.10) is implemented as

$$C_{DES}^2 = \max(0.5(L_{ij} M_{ij} / M_{ij}^2), 0). \tag{3.11}$$

For DES, there is an additional issue related to the near-wall RANS region. Based on the model formulation described thus far, it would seem that the extent of the RANS region would remain unaffected since the shielding function f_d would make the model to follow RANS behaviour. However, f_d is a function of k (equations 3.1), which in turn depends on C_{DES} (due to its appearance in the production term of the k equation).

This is highlighted in figure 3.9a which shows fd profiles obtained from 2 simulations of channel flow using our original DDES model, with different values of C_{DES}. We observe that the extent of the shielded region reduces when C_{DES} is reduced, which stems from the reduced production of k. This means that on a coarse mesh, the spuriously low values of C_{DES} returned

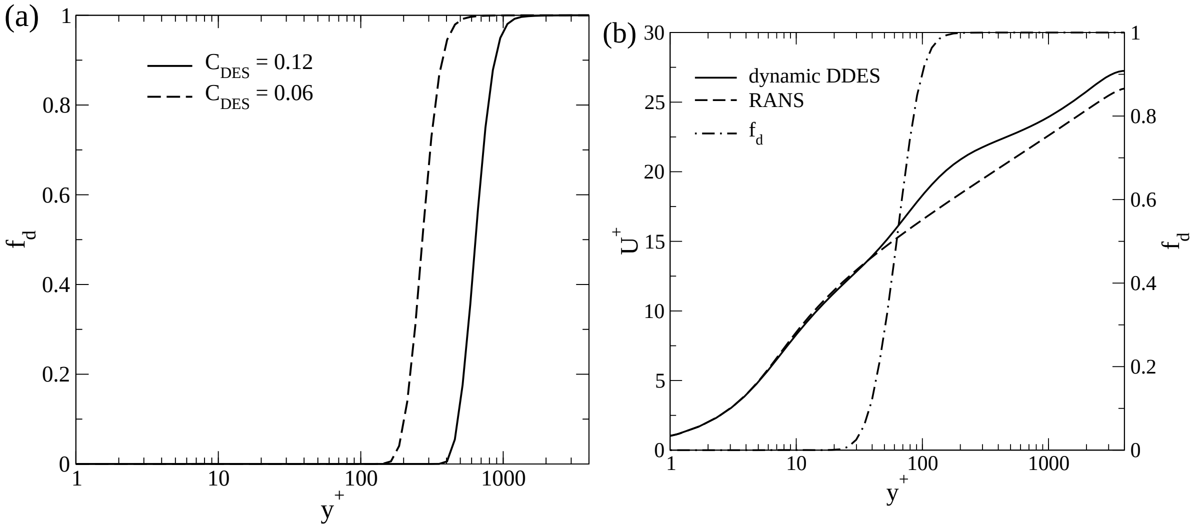

Figure 3.9: (a) Extent of the shielded region for different values of C_{DES} in channel flow ($Re_\tau = 4000$). (b) U^+ and f_d profiles obtained with dynamic procedure and clipping, but no check for mesh quality

by formula (3.11) would lead to a drastic reduction in the extent of the RANS region, leading to incorrect predictions of near-wall properties such as the wall shear stress, and subsequently, the mean velocity. This behaviour is highlighted in figure 3.9b, which shows profiles of f_d and U^+ obtained in a channel flow simulation using the dynamically evaluated constant C_{DES} (from equation 3.11). The mesh used here has a non-dimensional cell spacing of $\Delta x^+ = 400$ and $\Delta z^+ = 200$ with $\Delta y^+ < 1$ at the wall. For the same grid and flow conditions, using the original DDES model with constant C_{DES} was able to produce a good estimate for the mean velocity profile (Reddy et al. (2014)). Hence it is quite clear that using the dynamic procedure on coarse meshes can actually prove to be detrimental.

To ensure that the extent of the RANS region is not affected by the dynamically computed model constant, a simple albeit arbitrary modification was made as shown below:

$$C_{DES} = C^0_{DES} + (C_{dyn} - C^0_{DES}) \max(0, 10(f_d - 0.9)), \tag{3.12}$$

$$C^2_{dyn} = \max(0.5(L_{ij}M_{ij}/M^2_{ij}), 0), \text{where} \tag{3.13}$$

$$C^0_{DES} = 0.12.$$

The dynamically computed constant is now referred to as C^2_{dyn} as in equation (3.13). Instead of using it directly in the model, it is used in equation (3.12) to obtain the final local value of

C_{DES} to be used. For $f_d < 0.9$, equation (3.12) yields $C_{DES} = C^0_{DES}$ and the model functions as the original DDES model. For $f_d = 1$, $C_{DES} = C_{dyn}$ and the model starts using the dynamic procedure. Hence equation (3.12) ensures that the model is in RANS mode in the near-wall regions, and the dynamic procedure is active only in the eddy simulation branch.

3.4.2 Test case - flow through a 3D diffuser

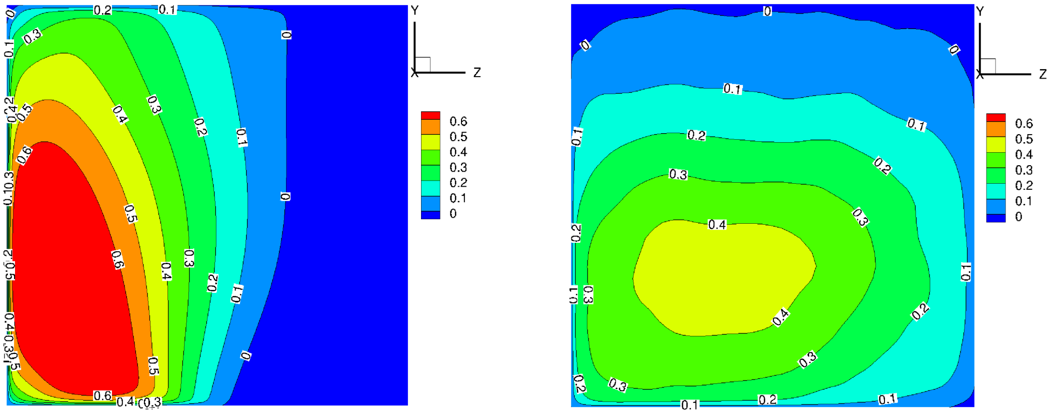

(a) $k - \omega$ RANS model - x/H = 15

(b) Model 1 - x/H = 15

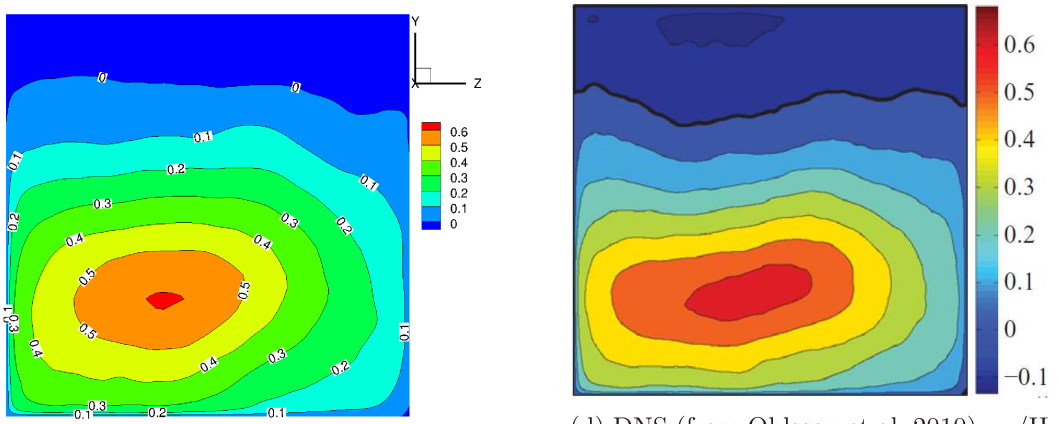

(c) Model 2 - x/H = 15

(d) DNS (from Ohlsson et al, 2010) - x/H = 15

Figure 3.10: Contours of normalized mean streamwise velocity $\bar{U}/U_b$

This case corresponds to the “diffuser 1” case of Cherry et al. (2008). The inflow to the diffuser is a fully developed flow with a Reynolds number of 10000 (based on the bulk velocity U_b and duct height H at the inflow of the diffuser). The mesh and inflow boundary condition are same as those in Jeyapaul (2011).

Three simulations for this geometry were carried out, each corresponding to a different turbulence model - $k-\omega$ RANS, the current DDES model with $C_{DES} = 0.12$ (referred to as "Model 1"), and the DDES model with dynamic computation of C_{DES} as in eqn. (3.12) (referred to as "Model 2").

Figure 3.10 shows contours of the normalized streamwise velocity at the end of the diffuser section (x/H = 15). The results from the RANS model (fig. 3.10a) are qualitatively incorrect, since it predicts separation along the side wall, as opposed to DNS of Ohlsson et al. (2010) shown in figure 3.10d, where separation occurs along the top wall. Model 1 (fig. 3.10b) however predicts separation along the top wall (although the extent of the separated region is lesser than in experiments or DNS). Thus Model 1 is able to produce results more accurate than RANS. However, quantitatively more accurate results are desired. Velocity profiles and separation contour along the centerplane obtained with Model 1 are compared with DNS data of Ohlsson et al. (2010) in figure 3.11, which shows significant differences.

Using Model 2 for this case improves the results significantly. Separation is predicted along the top wall (figure 3.10c), and the extent of the separated region is also more in line with DNS data. Figure 3.12 shows profiles of streamwise velocity and a separation contour, and is a significant improvement from Model 1 (fig. 3.11).

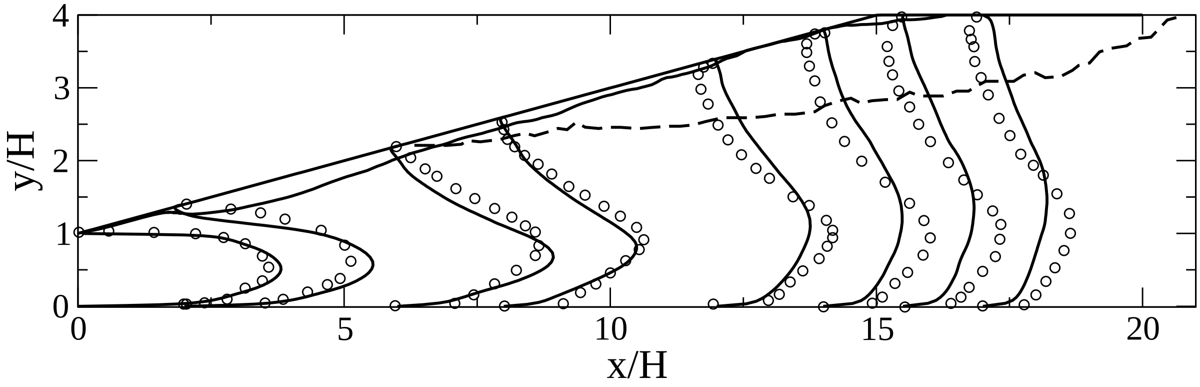

Figure 3.11: Profiles of mean streamwise velocity $(3\bar{U}/U_b + x/H)$ and separation contour along the midplane. Solid line - Model 1, Symbols and dashed line - DNS.

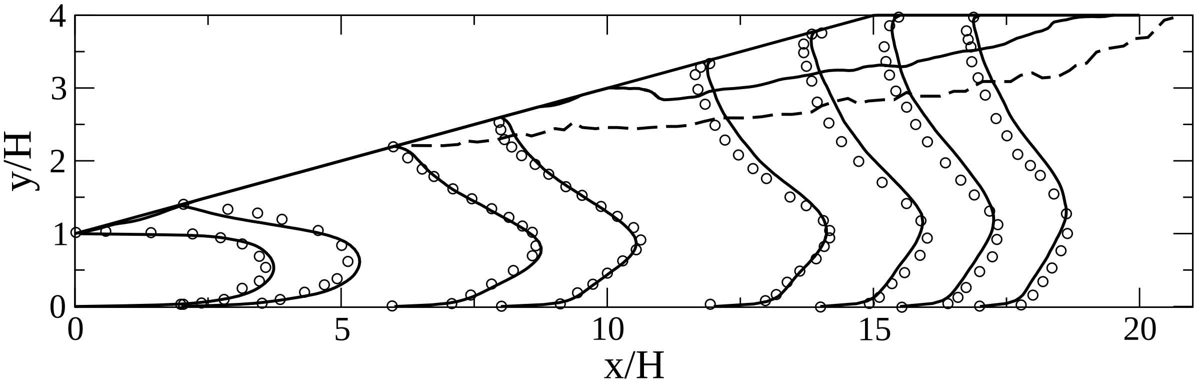

Figure 3.12: Profiles of mean streamwise velocity ($3\bar{U}/U_b + x/H$) and separation contour along the midplane. Solid line - Model 2, Symbols and dashed line - DNS.

3.5 Conclusions

A variation of the DDES formulation was developed with modified length scales to correct for LLM (as demonstrated for channel flow). The length scale was used to define the eddy viscosity, which limits the production term (rather than the dissipation term) of the k equation. Simulations of flows over a backward-facing step, and over periodic hills showed that the model is capable of handling separation. Results obtained using the DDES model for flow through an atomizer indicate that the model is robust enough to be applicable to complex 3D geometries. Since the value of the Smagorinsky constant C_s is known to vary with flow configuration, the value of C_{DES} in the current model also is likely to vary. Towards this end, a dynamic procedure similar to the dynamic Smagorinsky model was implemented to compute C_{DES} locally on the LES branch. Simulations of a three-dimensional diffuser suggest that the dynamic procedure improves the accuracy of the model.

The grid must be fine enough to resolve a significant portion of the inertial range, for the dynamic procedure to be valid. In this view, the grid requirements for the DDES model with dynamic computation of C_{DES} is likely more stringent than when using a constant C_{DES}. However, since we have the RANS branch active in the near-wall region, using a coarser near-wall cell spacing than a typical LES grid might be sufficient. The effect of the grid resolution on the performance of Model 2 needs to be studied further.

3.6 Acknowledgments

Computing resources were provided by Extreme Science and Engineering Discovery Environment (XSEDE), which is supported by National Science Foundation grant number OCI-1053575. Funding was provided by NASA grant NNX12AJ74A and by Pratt & Whitney.

CHAPTER 4. ON THE DYNAMIC COMPUTATION OF THE MODEL CONSTANT IN DELAYED DETACHED EDDY SIMULATION

Z. Yin, K. R. Reddy, P. A. Durbin, (2015)

Physics of Fluids (1994-Present), 27(2), 025105

The current work puts forth an implementation of a dynamic procedure to locally compute the value of the model constant C_{DES}, as used in the eddy simulation branch of Delayed Detached Eddy Simulation (DDES). Former DDES formulations (Spalart et al. (2006); Gritskevich et al. (2012)) are not conducive to the implementation of a dynamic procedure due to uncertainty as to what form the eddy viscosity expression takes in the eddy simulation branch. However, a recent, alternate formulation (Reddy et al. (2014)) casts the eddy viscosity in a form that is similar to the Smagorinsky, LES (Large Eddy Simulation) sub-grid viscosity. The resemblance to the Smagorinsky model allows the implementation of a dynamic procedure similar to that of Lilly (1992) A limiting function is proposed which constrains the computed value of C_{DES}, depending on the fineness of the grid and on the computed solution.

4.1 Introduction

Detached eddy simulation (DES) was put forth as a method to couple Reynolds averaged (RANS) models and eddy resolving simulation (Spalart et al. (1997)). It is an idea for using a single turbulence model in both the RANS and the eddy simulation branches. Some fundamental issues were identified with the original formulation, such as modeled stress depletion (Menter and Kuntz (2002)), and log-layer mismatch (Nikitin et al. (2000); Piomelli et al. (2003)). This led to modifications such as delayed DES (DDES) (Spalart et al. (2006)) and Improved DDES (IDDES) (Shur et al. (2008)).

These have led to an operational methodology. The successes to date argue for further advances. A natural desire would be to employ a dynamic model on the eddy simulation branch, analogous to the dynamic Smagorinsky model (DSM) of Lilly (1992). To some degree, this was explored previously (Bhushan and Walters (2012); Walters et al. (2013)) by using 2 different models — the Spalart-Allmaras RANS model and DSM — and interpolating between them. Yet another method is the use of a hybrid-filter (Rajamani and Kim (2010)), which leads to a set of filtered Navier-Stokes equations with additional terms. However, these are quite different from the present approach. DES utilizes a single turbulence model throughout the whole domain. We retain that feature. In most formulations, it is not obvious how a dynamic procedure can be implemented — the primary reason being uncertainty about the form of the eddy viscosity on the eddy simulation branch. This difficulty with DES models has been pointed out previously (Bhushan and Walters (2012)).

The uncertainty arises because the original DES models (Spalart et al. (2006)) were based on enhancing dissipation, using the grid spacing as the dissipation length when it became smaller than the RANS length scale. The same approach of enhancing dissipation was followed when DDES was adapted to the $k-\omega$ SST (Shear Stress Transport) RANS model (k is the turbulent kinetic energy, and ω the specific dissipation rate) by Gritskevich et al. (2012). Here again, it is not clear what the functional form of the eddy viscosity is in terms of the DDES/IDDES length scale.

We recently put forth an alternate formulation of DDES (Reddy et al. (2014)) based on the $k-\omega$ (or $k-\omega$ SST) RANS model, which uses the DDES length scale ℓ_{DDES} to define the eddy viscosity as $\nu_T = \ell^2_{DDES}\omega$. It follows that the length scale limiter can be interpreted as limiting the production term, rather than enhancing the dissipation term. This alternate formulation bears a similarity to the Smagorinsky model. Thus, an *a priori* estimate of the model constant $C_{DES} \approx 0.12$ was made from the Smagorinsky constant C_s. However, when the model was calibrated by channel flow simulations, a range of values of about $0.05 \lesssim C_{DES} \lesssim 0.15$ was found to be satisfactory.

It is known that the best value of the Smagorinsky constant C_s depends on the flow configuration (Germano et al. (1991)). The dynamic procedure allows it to adapt to the flow, and to the particular grid. This suggests that the leeway in the calibration of C_{DES} can be exploited in the same way. Because the eddy viscosity is specified directly in this alternate formulation (Reddy et al. (2014)), the dynamic procedure is immediately apparent.

The model formulation will be described in Sec. 4.2. The open source code OpenFOAM (Weller et al. (1998)) was used for all the present computer simulations. Gaussian finite volume integration with central differencing for interpolation, was selected for spatial discretization of equations. Time integration was by the 2^{nd} order, backward difference method. The resulting matrix system was solved using the Pre-conditioned Bi-conjugate gradient algorithm, with the simplified, diagonal-based, incomplete-LU (Lower Upper) preconditioner. Solution for the matrix system at each time step was obtained by solving iteratively, to a specified tolerance of the residual norm.

4.2 Model Formulation

The alternate DDES formulation (Reddy et al. (2014)) is reproduced here for convenience:

$$\begin{aligned} \ell_{DDES} &= \ell_{RANS} - f_d \max(0, \ell_{RANS} - \ell_{LES}), \\ \ell_{RANS} &= \frac{\sqrt{k}}{\omega}, \\ \ell_{LES} &= C_{DES}\Delta, \\ \Delta = f_d V^{1/3} + (1-f_d)h_{max}, &\quad C_{DES} = 0.12, \quad \nu_T = \ell_{DDES}^2\omega, \end{aligned} \tag{4.1}$$

where V is the cell volume, $h_{max} = \max(dx, dy, dz)$ is the maximum cell spacing and f_d is the DDES shielding function,

$$\begin{aligned} f_d &= 1 - \tanh\left([8r_d]^3\right), \\ r_d &= \frac{k/\omega + \nu}{\kappa^2 d_w^2 \sqrt{U_{i,j}U_{i,j}}}, \end{aligned} \tag{4.2}$$

where ν is the kinematic viscosity, κ the Von $K\acute{a}rm\acute{a}n$ constant, d_w the wall distance and $U_{i,j}$ the velocity gradient tensor.

Note, especially, that $\nu_T = \ell_{DDES}^2 \omega$. This ν_T defines the production term of the k equation in the $k-\omega$ RANS model (Wilcox (1993)), leaving all the other terms unaltered.

$$\begin{aligned} \frac{Dk}{Dt} &= \boldsymbol{2\nu_T|S|^2} - C_\mu k\omega + \nabla\cdot[(\nu + \sigma_k(k/\omega))\nabla k], \\ \frac{D\omega}{Dt} &= 2C_{\omega 1}|S|^2 - C_{\omega 2}\omega^2 + \nabla\cdot[(\nu + \sigma_\omega(k/\omega))\nabla \omega]. \end{aligned} \tag{4.3}$$

The standard constants are invoked,

$$C_\mu = 9/100, \quad \sigma_k = 1/2, \quad \sigma_\omega = 1/2, \quad C_{\omega 1} = 5/9, \quad C_{\omega 2} = 3/40.$$

For future reference, we will cite this formulation (Reddy et al. (2014)) as “Model 1”.

Thus on the eddy simulation branch ($f_d = 1$, $\ell_{LES} < \ell_{RANS}$), we have

$$\nu_T = (C_{DES}\Delta)^2\omega, \tag{4.4}$$

which is similar to the Smagorinsky sub-grid viscosity expression

$$\nu_{SGS} = (C_s\Delta)^2|S|. \tag{4.5}$$

In LES, the dynamic procedure evaluates a local value of C_s as follows:

$$C_s^2 = 0.5\frac{L_{ij}M_{ij}}{M_{ij}M_{ij}}, \tag{4.6}$$

$$L_{ij} = -\widehat{\overline{u_i u_j}} + \hat{\bar{u}}_i\hat{\bar{u}}_j, \tag{4.7}$$

$$M_{ij} = (\hat{\Delta}^2|\hat{\bar{S}}|\hat{\bar{S}}_{ij} - \Delta^2\widehat{|\bar{S}|\bar{S}_{ij}}). \tag{4.8}$$

The notations used in equations (4.7, 4.8) are the same as in Lilly (1992). The hat denotes explicit, test filtering where the test filter width is twice the grid scale. The test filtering is carried out via a spatial average of the face neighbour cells weighted by the surface area of the common face.

It is rather apparent that for the eddy viscosity definition in (4.4), this same dynamic procedure gives

$$C_{DES}^2 = 0.5\frac{L_{ij}M_{ij}}{M_{ij}M_{ij}}, \tag{4.9}$$

$$M_{ij} = (\hat{\Delta}^2\hat{\bar{\omega}}\hat{\bar{S}}_{ij} - \Delta^2\widehat{\bar{\omega}\bar{S}_{ij}}). \tag{4.10}$$

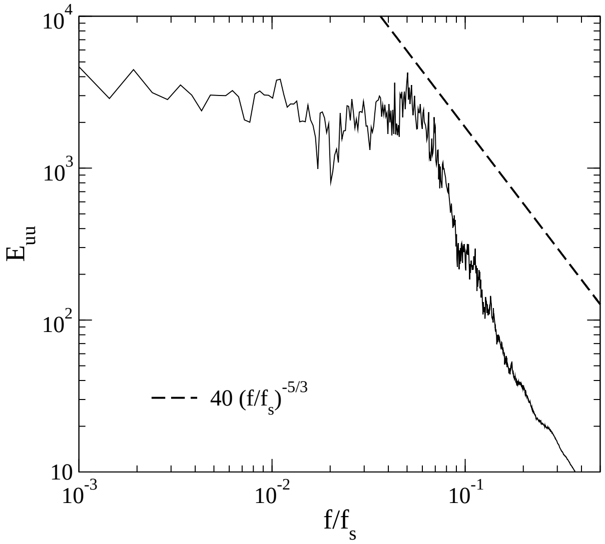

Figure 4.1: PSD measured in the post-separation shear layer region in the flow over a backward facing step. f_s is the sampling frequency.

Essentially, ω plays the role of the filtered rate of strain $|S|$. So the only change occurs in the definition of M_{ij} (eqn. 4.10) due to the difference in the eddy viscosity definition. In the first of equations (4.1), C_{DES} determines the switch from the RANS to LES length scales. By submitting this coefficient to the dynamic procedure, the switching criterion becomes adaptive.

The dynamic procedure can yield locally negative values of C_{DES}^2, which is not acceptable – this problem already exists in LES. It is resolved by clipping the right side of (4.9) at 0.

Indeed, there is yet another issue, related to the mesh resolution. In order for the test filter to be valid, a significant portion of the inertial range needs to be resolved. But the coarse meshes that sometimes are used in DES do not capture enough of the small scales. Figure 4.1 highlights this, where the power spectral density (PSD) of the streamwise velocity component u obtained in the simulation of a backward facing step is shown. The coarse mesh results in rather little inertial range and a rapid fall-off at high frequency. Then formula (4.9) yields spuriously low values of C_{DES}. In such circumstances, avoiding the dynamic procedure altogether might be best. For anything but these very coarse meshes there is a good prospect for dynamic DES. Indeed, if the mesh resolution is close to that of wall resolved LES, utilizing the dynamic procedure might be favorable, even in the near-wall region.

For DES, there is an additional issue related to the near-wall RANS region. Based on

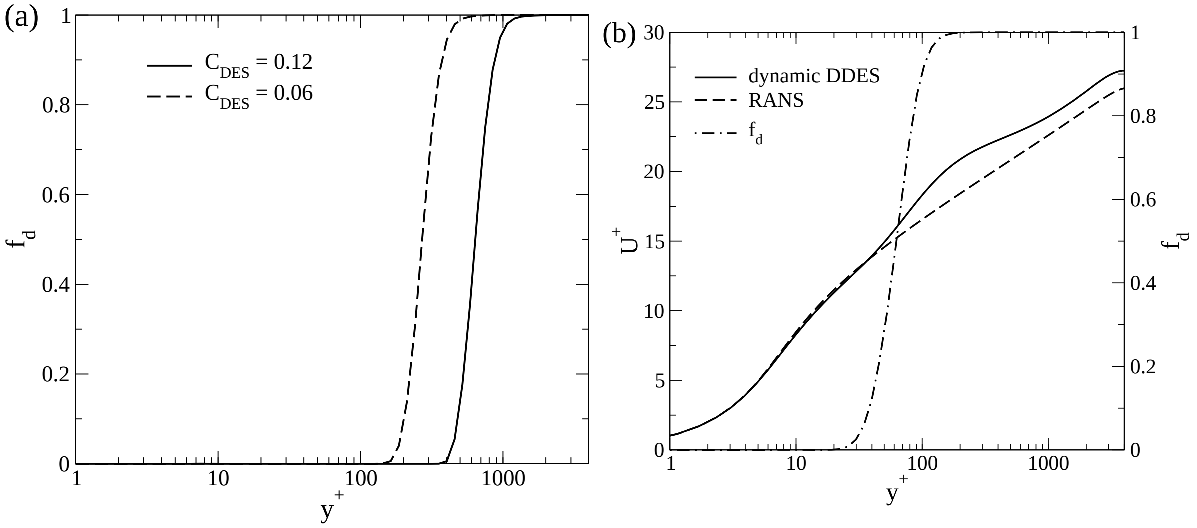

Figure 4.2: (a) Extent of the shielded region for different values of C_{DES} in channel flow ($Re_\tau = 4000$). (b) U^+ and f_d profiles obtained with dynamic procedure and clipping, but no check for mesh quality

the model formulation described thus far, it would seem that the extent of the RANS region would remain unaffected since the shielding function f_d would make the model to follow RANS behaviour. However, f_d is a function of k (via equations 4.2), which in turn depends on C_{DES} (due to it's appearance in the production term of the k equation).

This is highlighted in figure 4.2a which shows f_d profiles obtained from 2 simulations of channel flow using Model 1, with different values of C_{DES}. We observe that the extent of the shielded region reduces when C_{DES} is reduced, which stems from the reduced production of k. This means that on a coarse mesh, the spuriously low values of C_{DES} returned by formula (4.9) would lead to a drastic reduction in the extent of the RANS region, leading to incorrect predictions of near-wall properties such as the wall shear stress, and subsequently, the mean velocity. This behaviour is highlighted in figure 4.2b, which shows profiles of f_d and U^+ obtained in a channel flow simulation using the dynamically evaluated constant C_{DES} (from equation 4.9). Negative values for C^2_{DES} were clipped to zero. The mesh used here has a non-dimensional cell spacing of $\Delta x^+ = 400$ and $\Delta z^+ = 200$ with $\Delta y^+ < 1$ at the wall. For the same grid and flow conditions, Model 1 was able to produce a good estimate for the mean velocity profile (Reddy et al. (2014)). Hence it is quite clear that using the dynamic procedure on coarse meshes can actually prove to be detrimental.

To address these caveats, we introduce a limiting function which acts as a bound on the computed value of C_{DES}. It is described as follows:

$$
\begin{aligned}
C_{DES} &= \max(C_{lim}, C_{dyn}), && (4.11)\\
C_{dyn}^2 &= \max\left(0, 0.5\frac{L_{ij}M_{ij}}{M_{ij}M_{ij}}\right), && (4.12)\\
C_{lim} &= C_{DES}^0\left[1 - \tanh\left(\alpha\exp\left(\frac{-\beta h_{max}}{L_k}\right)\right)\right], && (4.13)\\
C_{DES}^0 &= 0.12, \quad L_k = \left(\frac{\nu^3}{\epsilon}\right)^{1/4}, \quad \alpha = 25, \quad \beta = 0.05, &&\\
\epsilon &= 2(C_{DES}^0 h_{max})^2\omega|S|^2 + C_\mu k\omega. && (4.14)
\end{aligned}
$$

Equation (4.12) is the same as equation (4.9), except that it is now clipped at 0, avoiding negative values for C_{dyn}^2. The right side of equation (4.9) is averaged over the face neighbor cells, weighted by the surface area of the common face, before it is clipped. No other averaging, such as along homogenous directions, or Lagrangian dynamic averaging (Meneveau et al. (1996)), is performed. As will be shown, the results obtained using such an approach yield satisfactory results, although it is possible that incorporation of some form of averaging might lead to additional robustness.

The idea behind equation (4.13) is to gauge the mesh resolution (Speziale (1998)) and subsequently, its suitability for invoking the dynamic procedure. The constants α and β were calibrated via channel flow simulations with various mesh resolutions.

The right side of equation (4.14) represents the contribution to the total turbulent kinetic energy dissipation of the sub-grid and the modeled component to ϵ. L_k is representative of the Kolmogorov length scale. If h_{max} represents the size of the smallest eddies being resolved, then $h_{max}/L_k \to 0$ represents a mesh resolution where a large portion of the inertial range has been resolved, and $h_{max}/L_k \to \infty$ represents a coarse mesh where using a constant C_{DES} might be more suitable. That constant value has been set to 0.12. Equation (4.13) interpolates between $C_{lim} = 0$ and $C_{lim} = 0.12$.

Figure 4.3 reflects this idea, where for a coarse mesh, $C_{DES} = C_{lim}$ and the model and the dynamic procedure cannot produce low values. For the other extreme, where the mesh is

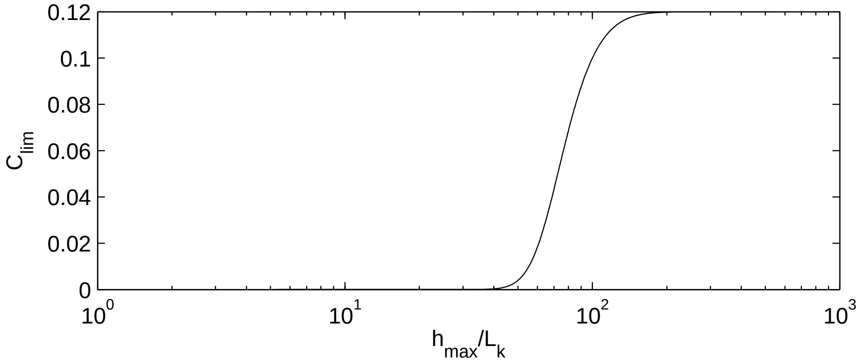

Figure 4.3: Variation of C_{lim} with h_{max}/L_k

fine enough to run LES even in the near-wall regions, the dynamic procedure would be utilized almost everywhere.

As pointed out in the Model 1 formulation (Reddy et al. (2014)), away from the wall, the average values of ω^2 and $|S|^2$ are proportional. In the near-wall region ω increases more rapidly than $|S|$ as $y \to 0$, because of its boundary condition, leading to large ϵ. Hence there will be a thin RANS region even for a wall-resolved, LES mesh, although the extent of the RANS region can be much smaller than that would be obtained with the native Model 1, or any other DDES formulation. Thus the limiting function takes advantage of the fineness of the mesh, by not imposing a mandatory, large near-wall RANS region. This behavior will be highlighted for some test cases.

The C_{DES} value obtained from equation (4.11) is used to evaluate ℓ_{LES} in equation (4.1), and subsequently, ν_T and the turbulent kinetic energy production. This completes the new dynamic DDES model formulation. The new model with the limiting function described above will be referred to as “Model 2” in the remaining portions of this article.

A comment needs to be made regarding the choice for the form of equation (4.14). The ϵ estimate is based on C^0_{DES} and h_{max}, rather than ν_T directly. This yields a conservative estimate, wherein a slightly larger ϵ is obtained, leading to a smaller value of L_k. That provides a more stringent requirement on the mesh resolution needed to achieve $h_{max}/L_k \to 0$. It acts as a safeguard against invoking the dynamic procedure on relatively coarse meshes.

4.3 Test Cases

4.3.1 Channel flow

Table 4.1: Grid resolution for channel flow cases with different Reynolds numbers

Re_τ	Δx^+	Δz^+
500	50	25
1200	120	60
2000	200	100
6000	600	300

Several channel flow simulations were carried out for a range of Reynolds numbers. All the channel flow cases were simulated using Model 2 and the results obtained are compared with DSM or $k-\omega$ RANS. For simulations with sufficient grid resolution, we expect a large portion of the domain to utilize the dynamic procedure. The grid and the extent of the computational domain is the same as in Reddy et al. (2014). The corresponding grid resolution in wall units for each Reynolds number are listed in Table 4.1. In all the cases, $\Delta y^+ < 1$ for the near-wall cells. The time step Δt is chosen to ensure that the maximum local CFL number ≈ 0.5.

Figure 4.4 shows the non-dimensionalized velocity profiles obtained for different values of Re_τ. The results show good agreement between the dynamic DDES model (Model 2) and DSM/RANS. The limiting value for C_{DES} reduces to 0 for the lower Re_τ cases (when the mesh in the eddying region is fine) and retains a larger value for the higher Re_τ cases (when the mesh is coarse). For $Re_\tau = 500$, the limiting function takes advantage of the mesh and allows the dynamic procedure to be utilized in the near wall region, with the entire log-layer located in the eddy simulation region. However, as pointed out in Sec. 4.2, we still have a thin RANS region close to the wall, due to ω growing more rapidly than $|S|$ as $y \to 0$. The large ω results in a large ϵ, which activates the limiting function, and the RANS branch replaces the eddy simulation branch.

The difference between the performance of Model 2 and Model 1 is highlighted in figure 4.5. Model 1 and Model 2 data correspond to a channel flow simulation with $Re_\tau = 500$, while the DNS data (Moser et al. (1999)) corresponds to $Re_\tau = 590$. Profiles of resolved u'^+, v'^+ and w'^+ are shown in figure 4.5a. The trend observed in the Model 1 predictions for this $Re_\tau = 500$

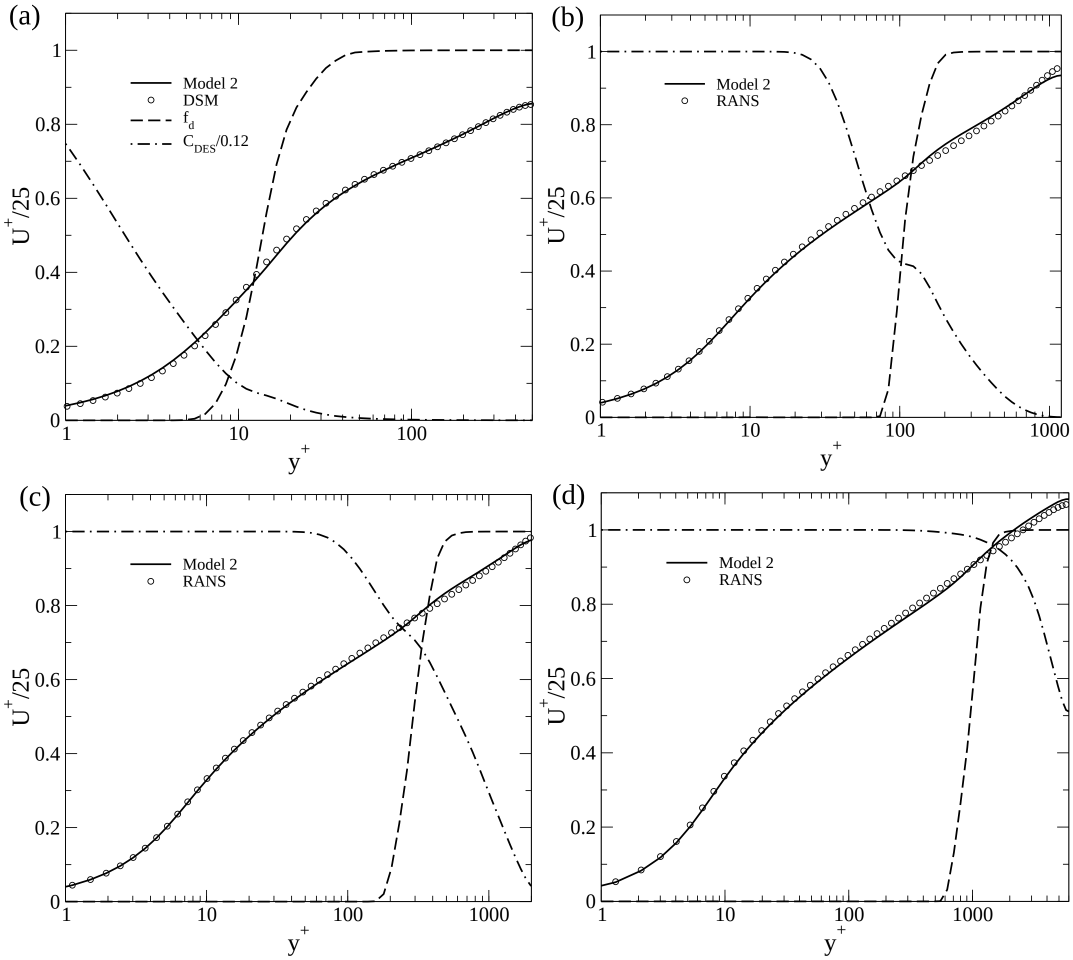

Figure 4.4: U^+ profiles for channel flow at different Re_τ. The dashed curve is f_d and the dash-dot curve is $C_{DES}/0.12$. Circles are RANS (same as DSM-LES). (a) $Re_\tau = 500$, (b) $Re_\tau = 1200$, (c) $Re_\tau = 2000$, (d) $Re_\tau = 6000$

case is similar to that observed for $Re_\tau = 2250$ (Reddy et al. (2014)). This is primarily due to the presence of a significant RANS region for Model 1 as shown in figure 4.5b, where the shielding function f_d is shown, along with k^+ — the non-dimensional total turbulent kinetic energy.

$$k^+ = (k_m + k_r)/u_\tau^2,$$

$$k_m = \text{ modeled component of } k,$$

$$k_r = 0.5(\overline{u'^2} + \overline{v'^2} + \overline{w'^2}) = \text{resolved component.}$$

Notice that the extent of the RANS region is similar for Model 1 with $Re_\tau = 500$ and $Re_\tau =$

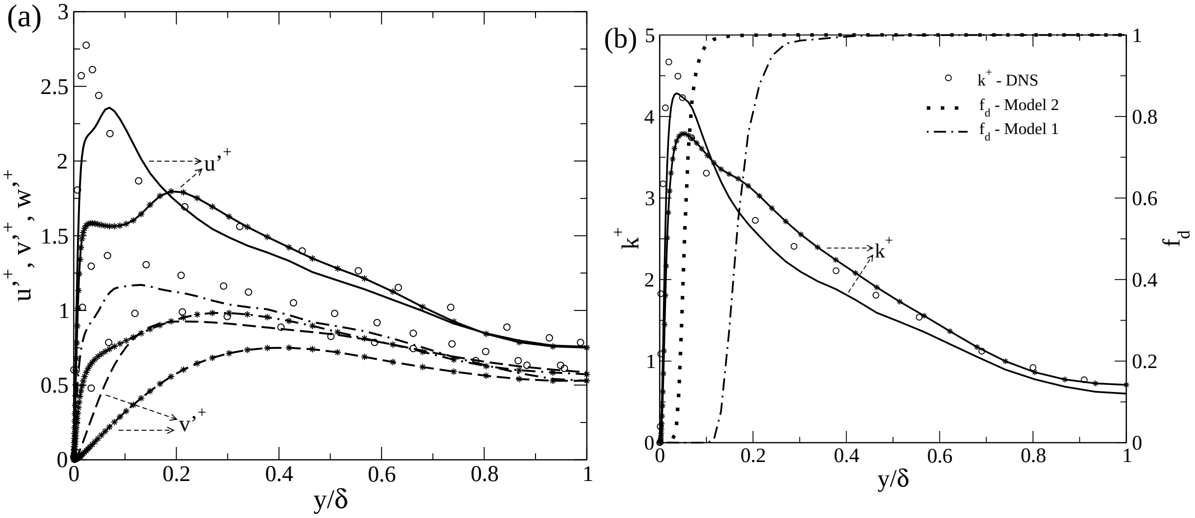

Figure 4.5: Circles - DNS data ($Re_\tau = 590$). Lines with '*' - Model 1, Lines without '*' - Model 2. Model 1 and Model 2 data correspond to $Re_\tau = 500$. (a) Profiles of resolved u'^+, v'^+ and w'^+, (b) Profiles of k^+ and f_d

2250, despite the fine mesh for the lower Re_τ. Model 2 however was able to "detect" that the mesh has sufficient resolution to employ the dynamic procedure. This leads to lower C_{DES}, and subsequently, lower k and ℓ_{LES} values, resulting in a smaller shielded region. Thus the eddy simulation branch is active over a larger region, which gives a better prediction of the velocity fluctuations and the turbulent kinetic energy.

4.3.2 Backward facing step

The flow over a backward facing step is an excellent case to test the performance of any hybrid RANS/LES method due to the abrupt change in flow features across the sharp edge. The model must be capable of switching from RANS to eddy simulation at the step, where the flow separates. The experimental setup of Vogel and Eaton (1985) was simulated. The Reynolds number at the inflow boundary is 28,000 based on the bulk velocity U_b and the step height H. Simulation details such as the grid used, the boundary conditions specified and the extent of the computational domain are the same as in Reddy et al. (2014).

Overall, a good agreement between the simulation and the experimental data is observed. Figure 4.6 shows the normalized mean streamwise velocity profiles and rms profiles at several

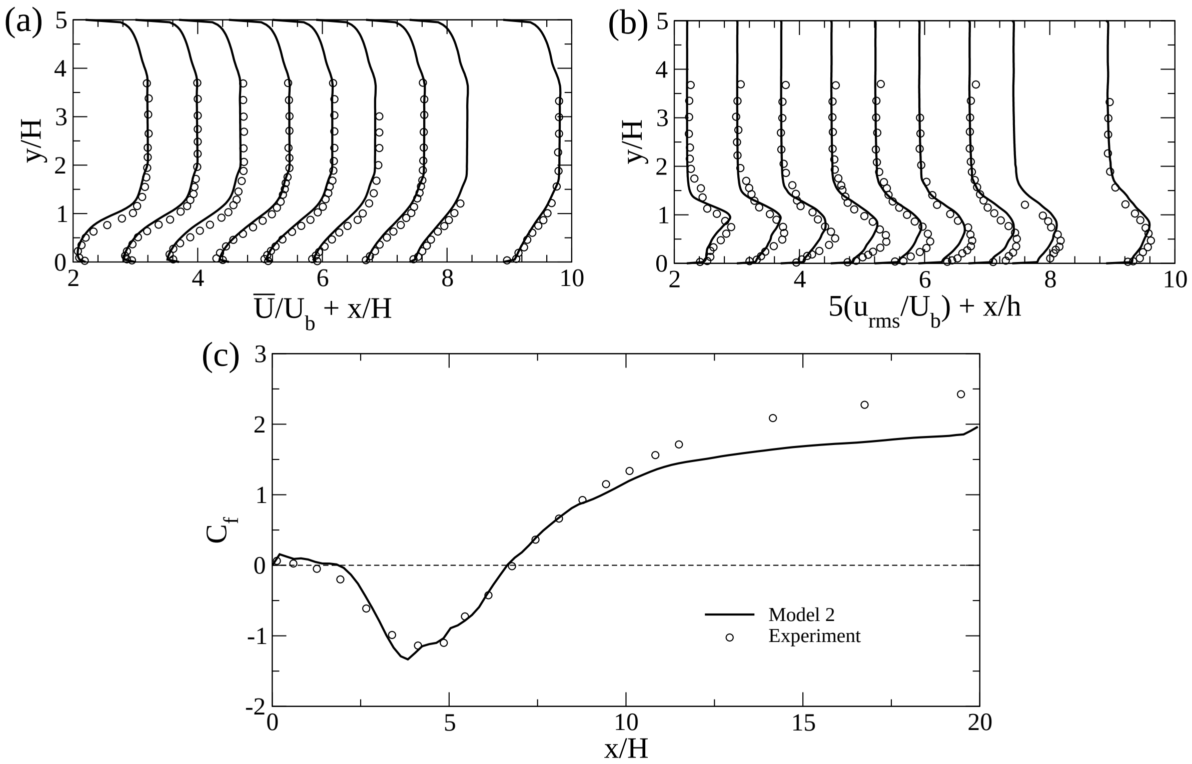

Figure 4.6: Flow over backward-facing step: Comparison with experimental data. (a) Normalized $\bar{U}$ profiles, (b) Normalized u_{rms} profiles, (c) Post-step $C_f \times 1000$ distribution along the bottom wall. Profiles taken at $x/H = 2.2, 3, 3.7, 4.5, 5.2, 5.9, 6.7, 7.4, 8.9$. Solid lines - Model 2 results, Symbols - Experimental data (Vogel and Eaton (1985))

streamwise locations, and the variation of the skin friction co-efficient C_f along the bottom wall. The C_f is computed from the wall shear stress obtained using a first order interpolation. The near-wall cells have $\Delta y^+ < 1$. Since the velocity varies linearly with the wall distance within the viscous sublayer ($y^+ \lesssim 5$), a first order interpolation is sufficient to accurately calculate the velocity gradient, and subsequently, the shear stress at the wall.

The grid used is relatively coarse ($\Delta x^+ \approx 200$ and $\Delta z^+ \approx 100$ away from the step), so we expect the limiting function to impose lower bounds on C_{DES}. Figure 4.7 shows contours of time-averaged C_{lim}. We observe that almost throughout the entire eddying region, $C_{lim} > 0.06 \Rightarrow C_{DES} > 0.06$.

C_{DES} hits the limiter at 0.12 where the flow separates from the step. Due to wall resolution requirements, the cell at the separation corner has very large aspect ratio, which deviates from typical LES grid resolution. Also, the rate of strain is large, which means that dissipation is

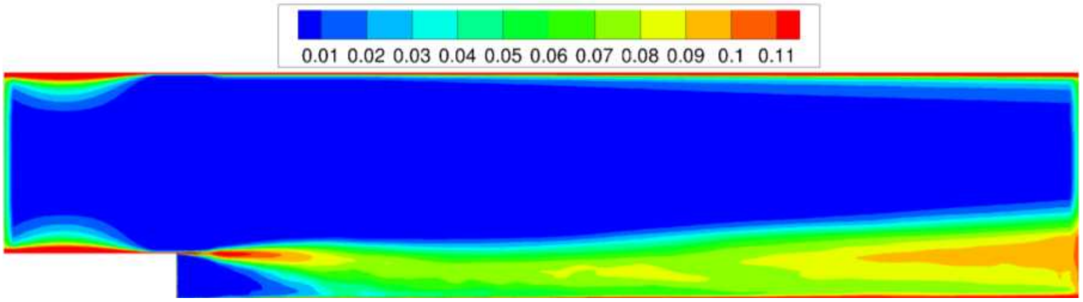

Figure 4.7: Time Averaged C_{lim} contours

high. As a result, the values of L_k are relatively low, causing the bound on the value of C_{DES} to be invoked.

4.3.3 Periodic hills

This case shows flow separation from a smooth surface, unlike the backward-facing step. The geometry and flow conditions are as described in Froehlich et al. (2005). The extent of the computational domain is $9H$ and $4.5H$ along the streamwise and spanwise directions respectively, where H is the hill height at the crest. The Reynolds number based on the hill height and the bulk velocity at the crest is $10,595$. The grid used has $106 \times 100 \times 90$ points in the streamwise, wall normal and spanwise directions respectively. Periodic boundary conditions are enforced along the streamwise and spanwise directions. The flow is driven by a pressure gradient source term which is adjusted to sustain the required bulk velocity at the inflow boundary. A maximum local CFL number < 0.5 is maintained throughout the entire domain.

Figure 4.8 compares the skin friction distribution along the bottom wall, mean streamwise velocity profiles and rms profiles from Model 2 to LES data. Overall, there is a good agreement. Additionally, figure 4.8a also shows the C_f prediction obtained from Model 1. We notice that Model 1 predicts a larger C_f than LES data near the inlet ($x/H = 0$), compared to the more accurate prediction of Model 2. The mean and rms velocity predictions of Model 1 are however very similar to that of Model 2 for the current grid, and hence those profiles have not been shown in order to avoid clutter.

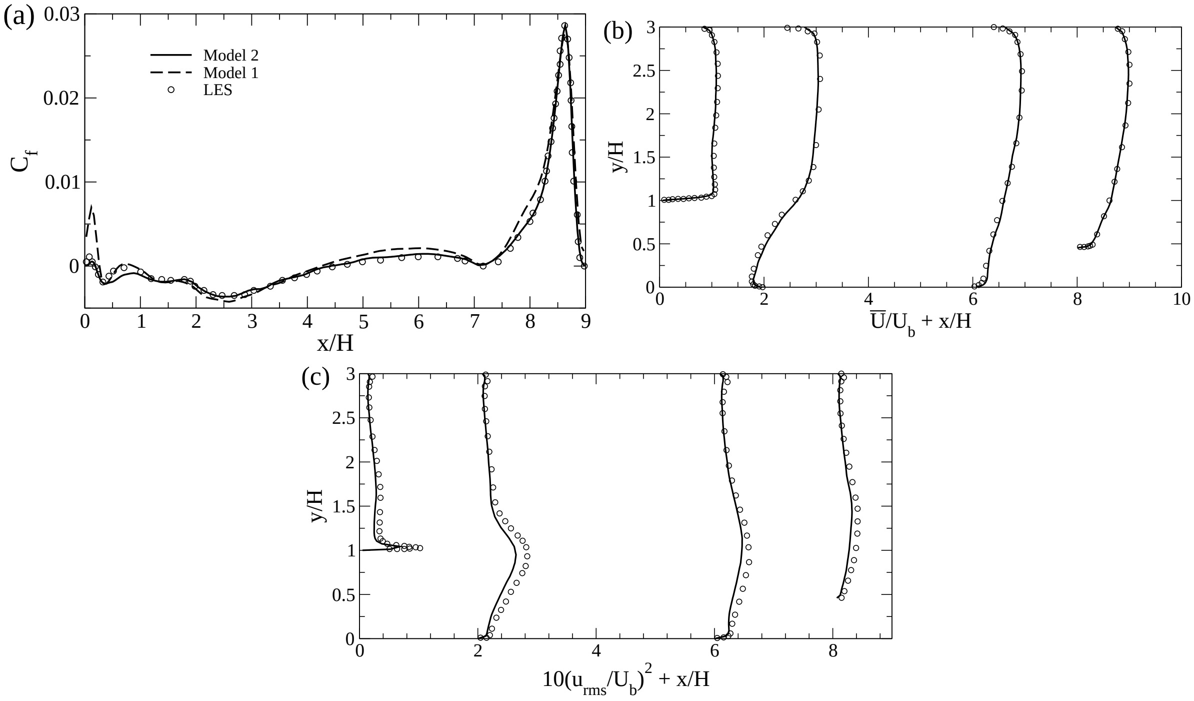

Figure 4.8: Flow over 2D periodic hills: (a) Variation of the skin-friction coefficient along the bottom wall, (b) Normalized mean velocity profiles, (c) Normalized u_{rms} profiles. Profiles taken at x/H = 0.05, 2, 6, 8

4.3.4 3D diffuser

As an example of a 3D geometry, the flow through a 3D diffuser was simulated. The geometry and flow conditions correspond to the "diffuser 1" of Cherry et al. (2008). The grid and boundary conditions are the same as in Jeyapaul (2011). The grid is nearly LES-quality. Three simulations were carried out for this geometry, each corresponding to a different turbulence model – the $k - \omega$ RANS model (Wilcox (1993)), Model 1 (Reddy et al. (2014)) and Model 2 (the current dynamic DDES model).

Figure 4.9 shows contours of the time-averaged streamwise velocity component obtained from all three simulations at the diffuser exit ($x/H = 15$, where H is the height of the inlet section). The RANS result (figure 4.9, top left) is qualitatively incorrect since it predicts separation along the side wall, as opposed to experiments (Cherry et al. (2008)) and DNS (Ohlsson et al. (2010)) where separation is along the top wall. Model 1 does predict separation along the top wall (figure 4.9, top right) – an improvement over RANS – but, the separation

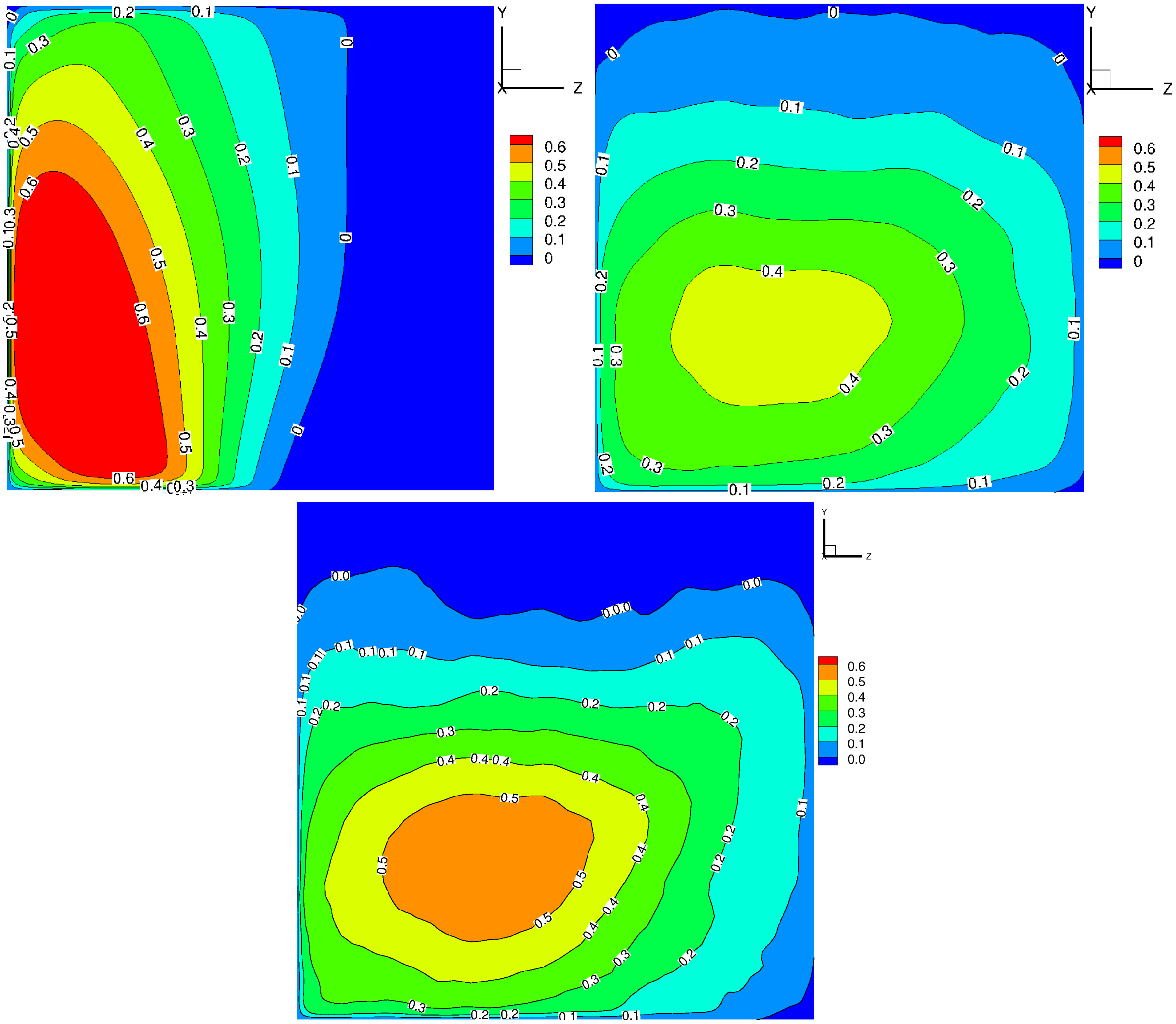

Figure 4.9: Contours of normalized mean streamwise velocity $\bar{U}/U_b$ along the diffuser exit plane ($x/H = 15$). Top left: $k - \omega$ RANS model, Top right: Model 1, Bottom: Model 2

region is much thinner than the DNS data. Figure 4.10 compares the separation contours and mean velocity profiles (at $x/H = 0, 2, 6, 8, 12, 14, 15.5, 17$) along the midplane obtained for Model 1 with DNS data (Ohlsson et al. (2010)), showing the deviation of Model 1 predictions from DNS.

Introducing the dynamic procedure improves the results appreciably. The bottom portion of figure 4.9 shows the mean velocity contours obtained using Model 2, and the corresponding separation contours and mean velocity profiles along the midplane are shown in figure 4.11. The agreement with DNS data is much better than with Model 1. The dynamic DDES model

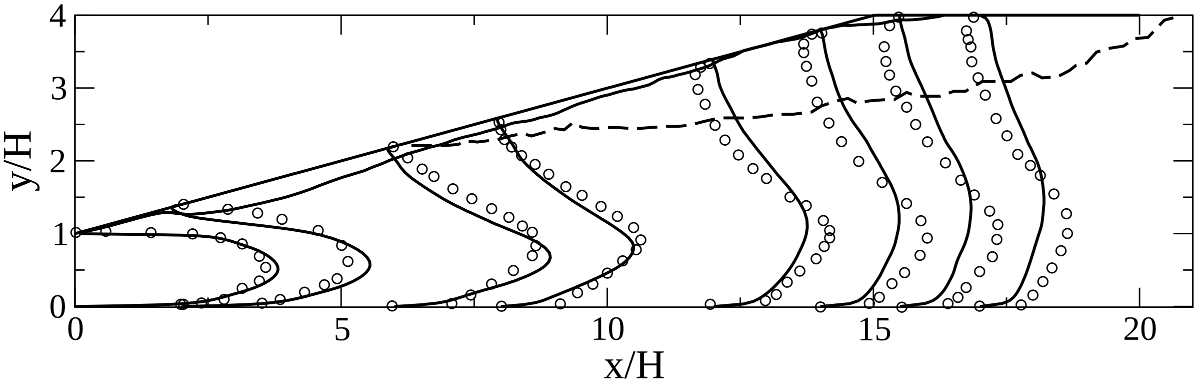

Figure 4.10: Profiles of mean streamwise velocity $(3\bar{U}/U_b + x/H)$ and separation contour along the midplane. Solid line - Model 1, Symbols and dashed line - DNS.

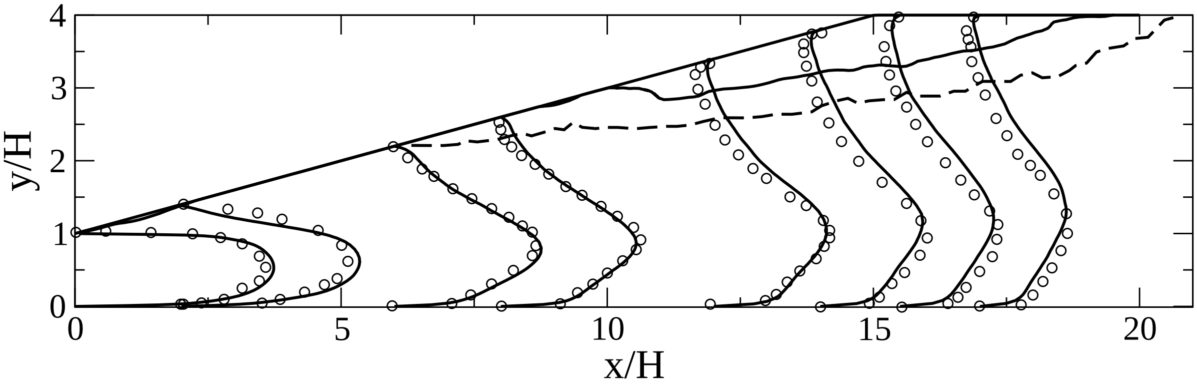

Figure 4.11: Profiles of mean streamwise velocity $(3\bar{U}/U_b + x/H)$ and separation contour along the midplane. Solid line - Model 2, Symbols and dashed line - DNS.

was able to take advantage of the grid resolution, utilizing the dynamic procedure almost everywhere in the domain, leading to a marked improvement in the prediction.

4.3.5 Rotating channel

The flow through a fully developed rotating turbulent channel was simulated as another illustration of the advantage of the dynamic procedure over a constant C_{DES}. In pure RANS mode, $k - \omega$ would require some kind of curvature correction to handle rotating flows (Arolla and Durbin (2013)). No such corrections are used here. This means that simulations based on Model 1 would likely be subject to errors due to the presence of a thick RANS region near the walls.

In the eddy-simulation region, rotation effects are captured by the Navier-Stokes equations. Thus, we expect to get better results using Model 2 since the RANS region will be smaller, provided the mesh is fine enough.

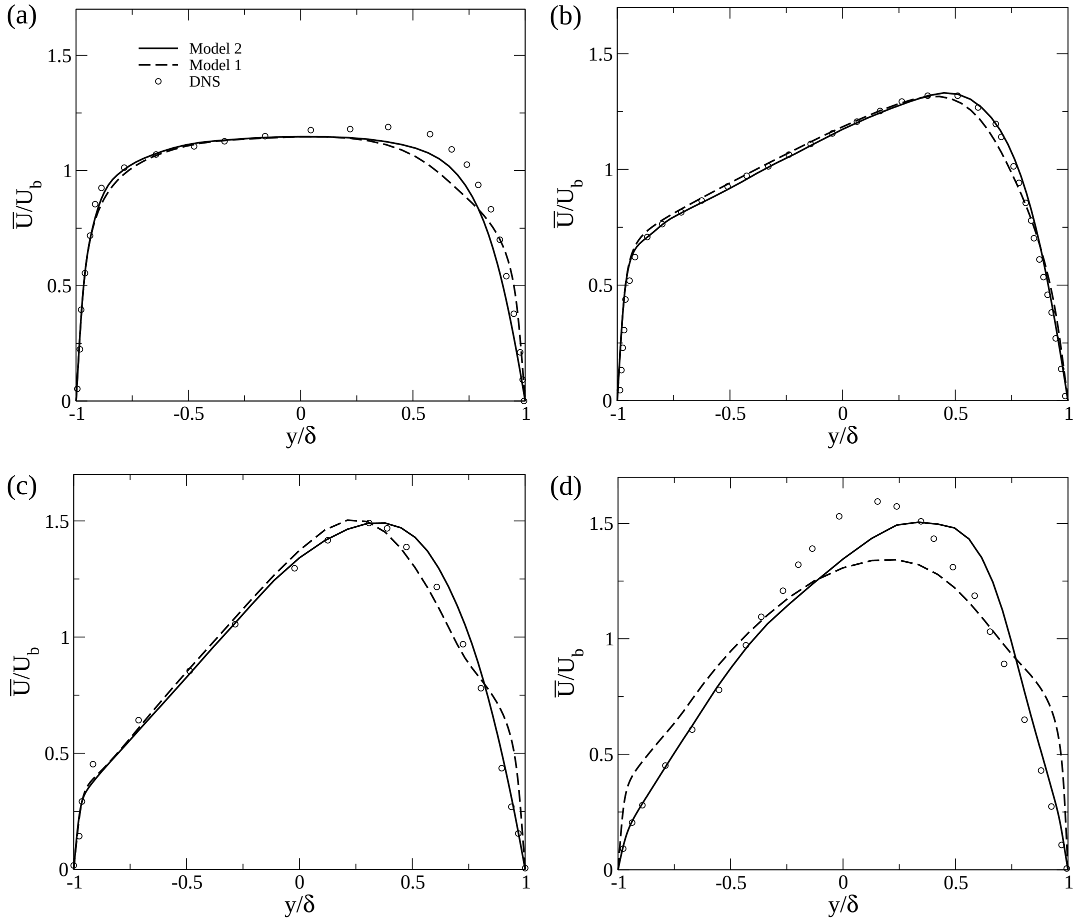

Figure 4.12: Mean velocity profiles normalized with the bulk velocity U_b for rotating channel flow at different Ro. (a) $Ro = 0.1$, (b) $Ro = 0.5$, (c) $Ro = 0.98$, (d) $Ro = 1.5$

The non-dimensional measure of rotation is the rotation number (Grundestam et al. (2008)), $Ro = 2\Omega\delta/U_b$, where U_b is the bulk velocity, δ the channel half-width and Ω the rate of coordinate system rotation. Four different simulations were carried out, corresponding to four different Ro values. These simulations correspond to previous DNS studies of Grundestam et al. (2008) ($Ro = 0.98, 1.5$) and Kristoffersen and Andersson (1993) ($Ro = 0.1, 0.5$).

In the DNS studies, a constant pressure gradient was prescribed, which forces constant total u_τ and Re_τ values. The bulk velocity, U_b and Re_b (Reynolds number based on the bulk velocity) then vary with Ro. In our simulations, U_b was specified, for each Ro, and the resulting u_τ and Re_τ values were computed.

Figure 4.12 shows mean velocity profiles obtained with both Model 1 and Model 2, compared with DNS data. Model 2 results are more in line with the data, especially near the right wall, at higher Ro, where the turbulence is suppressed by rotation.

Due to the asymmetry in the velocity profile, there are 2 different friction velocities, $u_{\tau u}$ and $u_{\tau s}$, corresponding to the unstable and stable sides (Grundestam et al. (2008)). An average friction velocity u_τ is defined as

$$u_\tau = [0.5(u_{\tau u}^2 + u_{\tau s}^2)]^{1/2}.$$

For the specified bulk velocity U_b, the predicted Re_τ values for Model 1 and Model 2 are

Table 4.2: Predicted Re_τ for different Ro values

Ro	Re_τ		
	DNS	Model 1	Model 2
0.1	194	229	196
0.5	194	206	199
0.98	180	215	179
1.5	180	330	187

shown in table 4.2, along with the reference DNS values. Model 2 predicts more accurate values for the wall shear stress than Model 1. The grid used for these cases has a non-dimensional cell spacing $\Delta x^+ = \Delta z^+ \approx 30$ for Model 2 (the corresponding numbers evaluated when using Model 1 ≈ 50 due to the larger predicted u_τ), with $\Delta y^+ < 1$ for the near wall cells in all the simulations. This leads to a smaller RANS region while using Model 2, and subsequently a smaller error stemming from the absence of any curvature correction terms.

At large Ro, we observe that Model 2 starts to deviate from the DNS results, especially on the right wall (figure 4.12d). That is the wall where rotation is stabilizing. A likely explanation for the discrepancy is that the RANS model does not include a curvature correction. Hence, as long as there is a thin RANS region, it cannot laminarize. Regions of negative production were observed (Grundestam et al. (2008)) for $Ro = 1.5$, and that certainly cannot be captured by the $k-\omega$ eddy viscosity model. For lower Ro values, the predictions are in good agreement with DNS.

4.3.6 Fundamental aero investigates the hill (FAITH) geometry

As an illustration of the model performance for a complex flow configuration, a simulation of the flow over a 3D axisymmetric hill was carried out. The geometry is the FAITH (Bell et al. (2012)). The variation of the hill height h with the radius r is

$$h = 3\cos\left(\frac{\pi r}{9}\right) + 3, \quad 0 \leq r \leq 9,$$

where r and h are in inches. The total radius of the hill is $R = 9''$, with the hill height at the centroid $H = 6''$. The Reynolds number based on H is $Re_H = 500,000$, with a mean inflow velocity $U_\infty = 50.3\ m/s$. More details regarding the experimental setup, and available data can be found in Bell et al. (2012) and Husen et al. (2014).

The extent of the computational domain used is $20H \times 5.3H \times 8H$ along the streamwise, wall normal and spanwise directions respectively. The hill is centered at $x/H = z/H = 0$. These dimensions correspond to the wind tunnel test section used in the experiments. A plug flow is specified at the inflow and the boundary layer develops along the streamwise direction. The length of the inlet section ensures that the required boundary layer thickness is obtained at $x/H = 0$ in the absence of the hill. The grid used has ≈ 3 million cells. At the hill, 130×130 cells are distributed uniformly along the streamwise and spanwise directions along it's diameter, with the cell spacing stretched out towards the inflow and outflow boundaries, and along the remaining spanwise portions. The maximum value of the local CFL number ≈ 0.5.

Figure 4.13 shows simulation results obtained using Model 2. Figure 4.13a shows contours of the magnitude of skin friction coefficient C_f over a square region around the hill (the circular edge of the hill is the incircle of the square), and is in good agreement with experimental data (Bell et al. (2012)). Normalized time-averaged streamwise velocity components are compared with experimental data in figure 4.13b.

Figure 4.14 shows contours of $\bar{U}$, k, u_{rms}, and $\overline{u'v'}$ along the spanwise centerplane on the lee side of the hill. Here, k represents the total turbulent kinetic energy, which is the sum of the

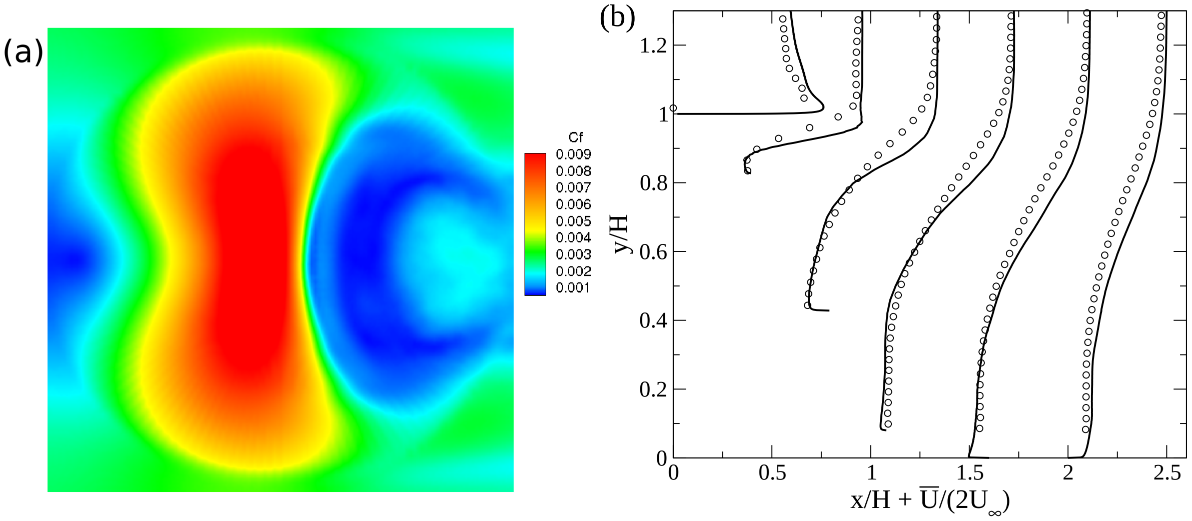

Figure 4.13: (a) Contours of magnitude of skin friction coefficient, (b) mean streamwise velocity profiles behind the hill at $x/H = 0, 0.4, 0.8, 1.2, 1.6, 2$

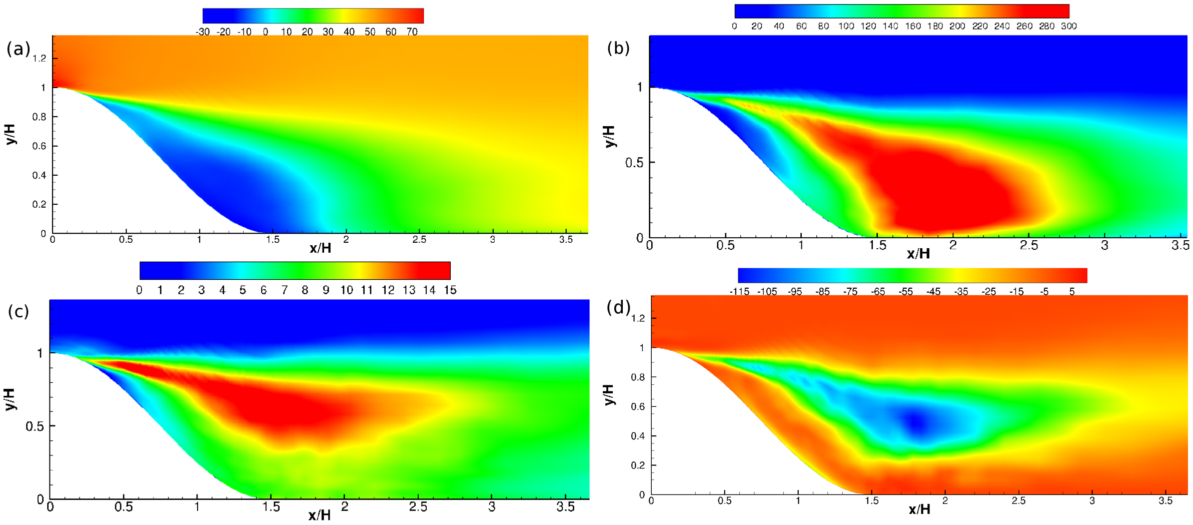

Figure 4.14: Contours of (a) mean streamwise velocity $\overline{U}$, (b) total turbulent kinetic energy k, (c) u_{rms}, and (d) $\overline{u'v'}$ in the $z/H = 0$ plane behind the hill

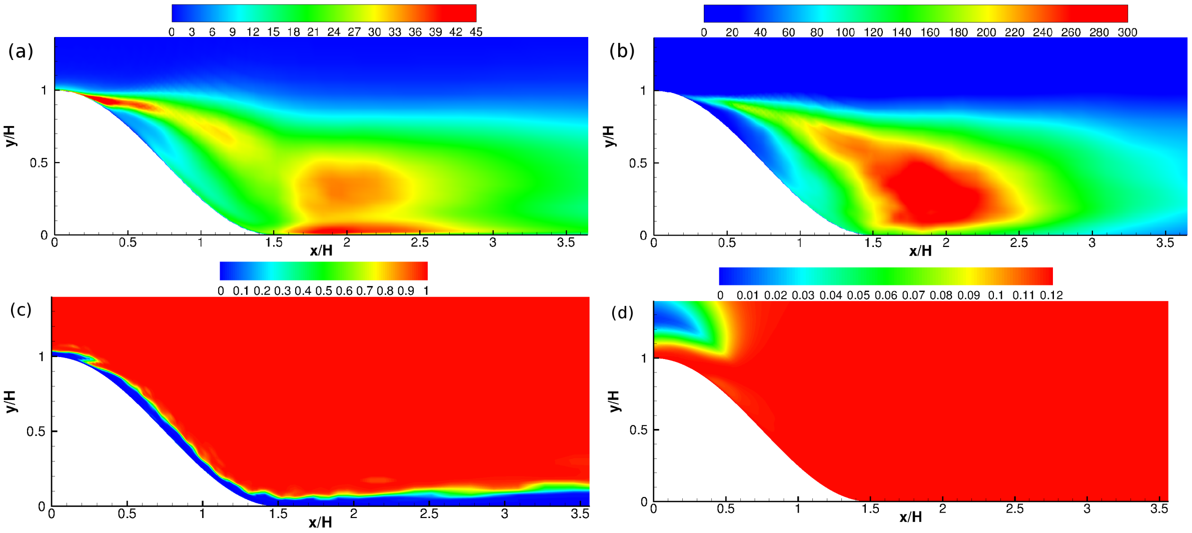

Figure 4.15: Contours of (a) k_m, (b) k_r, (c) f_d, and (d) C_{DES} in the $z/H = 0$ plane behind the hill

modeled and resolved components ($k_m + k_r$). Overall, the trends observed in the PIV (Particle Image Velocimetry) data (Bell et al. (2012)) are captured by the simulation. However, the peak values of k and u_{rms} are slightly overestimated.

One possible explanation for this would be the coarseness of the mesh used — $\Delta x^+ = \Delta z^+$ is large (as high as 1000 in some regions, depending on the local friction velocity u_τ). The fact that the mesh is coarse can also be inferred from figure 4.15d which shows that $C_{DES} = C^0_{DES} = 0.12$ over the entire region behind the hill, where we observe most of the relevant unsteady phenomena. Hence Model 2 essentially functions as Model 1 for simulations involving very coarse meshes. Figure 4.15c shows the extent of the RANS region ($f_d = 0$), and from figure 4.15a, we can observe that the magnitude of the modeled turbulent kinetic energy k_m in the LES region is comparable to that in the RANS region. This is another indication that the mesh being used is coarse. Better agreement with experimental data could likely be achieved by increasing the mesh resolution such that the dynamic procedure is employed in the eddy simulation regions.

4.4 Conclusion

The previously proposed, DDES formulation (Reddy et al. (2014)) opened the possibility to develop a dynamic DDES formulation. The model constant C_{DES} is computed locally via a well-established procedure. This requires a test filter that captures the small scales. Coarse grids are sometimes used for DES, and these small scales are not present. A limiting function was introduced in order to estimate the validity of utilizing the dynamic procedure on the given mesh. The function compares grid spacing to a Kolmogorov scale. Based on this, C_{DES} becomes a default value if the dynamic procedure is likely to fail. Simulations showed improved predictions when employing the dynamic procedure, rather than using a constant C_{DES}. That was especially true when simulations were carried out on LES-quality meshes.

The dynamic procedure yields superior performance over the constant coefficient model for 2 reasons. The first reason is similar to the case of LES: the coefficient adapts to how well the turbulence is resolved; if it is well resolved C_{DES} becomes very small. The second reason is peculiar to detached eddy simulation: using a locally computed C_{DES} in ℓ_{LES} causes the RANS region to become thinner when the mesh is fine. By maximizing the size of the eddy simulation region, the dynamic DDES model is able to reduce any drawbacks in the RANS model (such as the absence of curvature corrections while simulating rotating turbulent channel flow).

A key observation is how obvious it was to implement a dynamic procedure into our alternate DDES formulation (Reddy et al. (2014)). That is because it was designed to be similar to the Smagorinsky model. It is likely that other improvements/modifications made to the original Smagorinsky formulation can also be implemented. This could lead to additional robustness of this DES formulation, capable of handling a wide range of flow configurations.

4.5 Acknowledgements

Computing resources were provided by Extreme Science and Engineering Discovery Environment (XSEDE), which is supported by National Science Foundation grant number OCI-1053575. Funding was provided by NASA grant NNX12AJ74A and by Pratt & Whitney.

للاستشارات المنارة

CHAPTER 5. CONCLUSION

5.1 Summary of Results

In Chapter 2, a different approach of constructing a DDES model was explored. The RANS eddy viscosity formulation ν_T was modified such that it mimics the Smagorinsky subgrid viscosity expression. Thus

$$\nu_T = (C_{DES}\Delta)^2\omega, \tag{5.1}$$

in the eddy simulation branch. This new ν_T expression was then used to define the production term of the turbulent kinetic energy equation in the $k-\omega$ RANS model, while simultaneously being used in the momentum equation. That way, it retained its original meaning of a transfer of energy. This is the production-limited approach.

This is different from the previous DDES approach (Spalart et al. (2006); Gritskevich et al. (2012)), where the dissipation term was enhanced directly using ℓ_{DDES}. This can be termed as the dissipation-limited approach. A comparison of the production-limited and dissipation-limited approaches showed that they both produce similar results (figure 5.1). A modified length scale definition Δ was used to reduce the LLM observed in channel flows, without resorting to the complex IDDES formulation. Overall, the model performed well for canonical flows such as the backward-facing step and 2D periodic hills, and for complex flows such as the atomizer, the results of which were presented in Chapter 2. The key advantage of the production-limited approach is that an expression for the eddy viscosity in the eddy simulation branch is readily available.

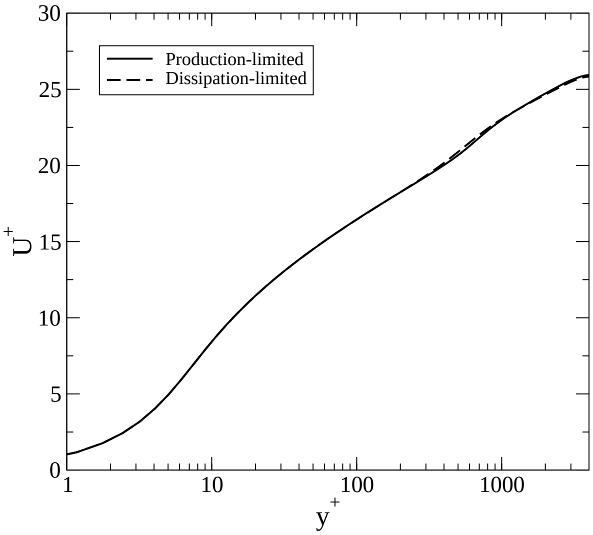

Figure 5.1: Comparison of U^+ in channel flow for production-limited and dissipation-limited DDES: $Re_\tau = 4000$

In Chapter 3, a dynamic procedure (similar to Lilly (1992)) to compute the local value of the model constant C_{DES} was implemented. This was possible due to the availability of a functional form for the eddy viscosity in terms of C_{DES}, in the new DDES model formulation described in Chapter 2. The resulting DDES formulation incorporated a dynamic LES model in the eddy simulation branch — something which was not possible with previous DDES approaches.

It was shown that the results obtained using this approach were significantly more accurate than those obtained with the original DDES model where a constant C_{DES} is used. This was observed in the simulation of the separated flow through a 3D diffuser. Figure 5.3 shows the mean streamwise velocity profiles and the separation contour obtained using the DDES model with a constant C_{DES}. There are significant deviations in the simulation data compared to DNS. A much better agreement was obtained by using the dynamically evaluated C_{DES}, as shown in figure 5.4. This was discussed in Chapter 3.

In Chapter 4 a limiting function was introduced which compared the grid scale to an approximate Kolmogorov scale to get an estimate of the mesh quality, based on which the C_{DES} value computed by the dynamic procedure was clipped. The limiting function made the

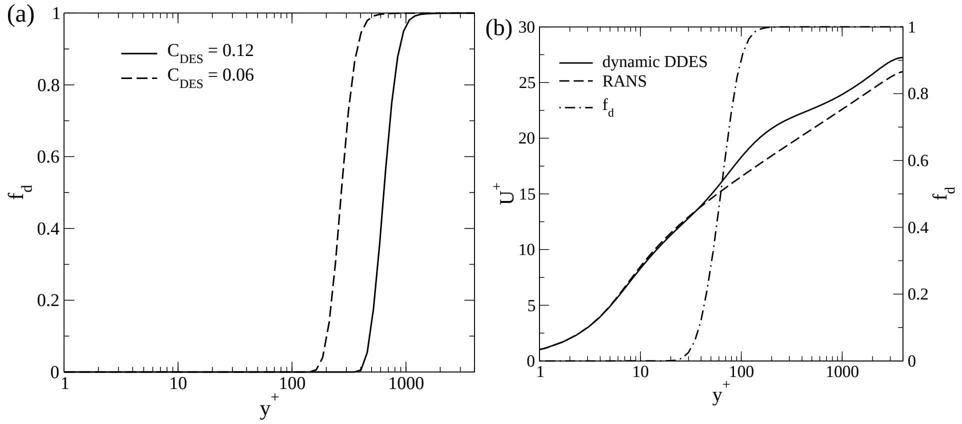

Figure 5.2: (a) Extent of the shielded region for different values of C_{DES} in channel flow ($Re_\tau = 4000$). (b) U^+ and f_d profiles obtained with dynamic procedure and clipping, but no check for mesh quality

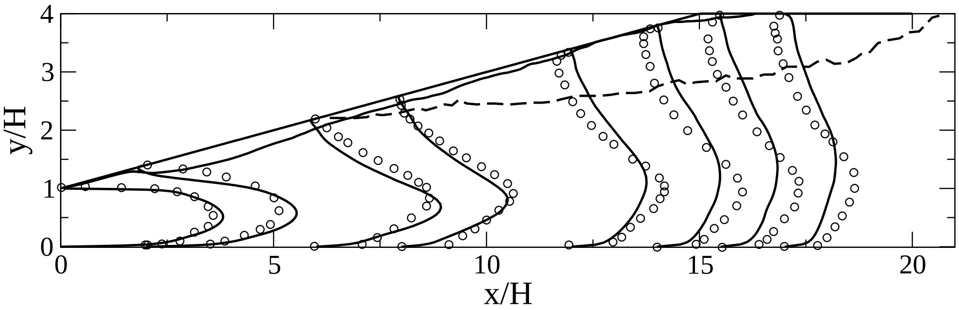

Figure 5.3: Profiles of mean streamwise velocity ($3\bar{U}/U_b + x/H$) and separation contour along the spanwise midplane. Solid line - Model 1, Symbols and dashed line - DNS of Ohlsson et al. (2010).

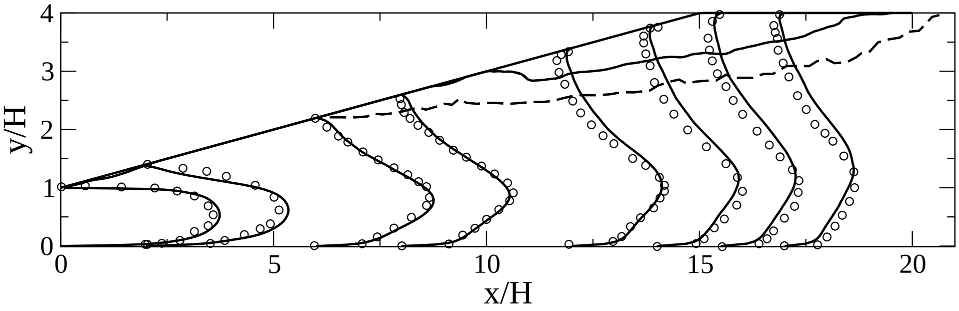

Figure 5.4: Profiles of mean streamwise velocity ($3\bar{U}/U_b + x/H$) and separation contour along the spanwise midplane. Solid line - Model 2, Symbols and dashed line - DNS of Ohlsson et al. (2010).

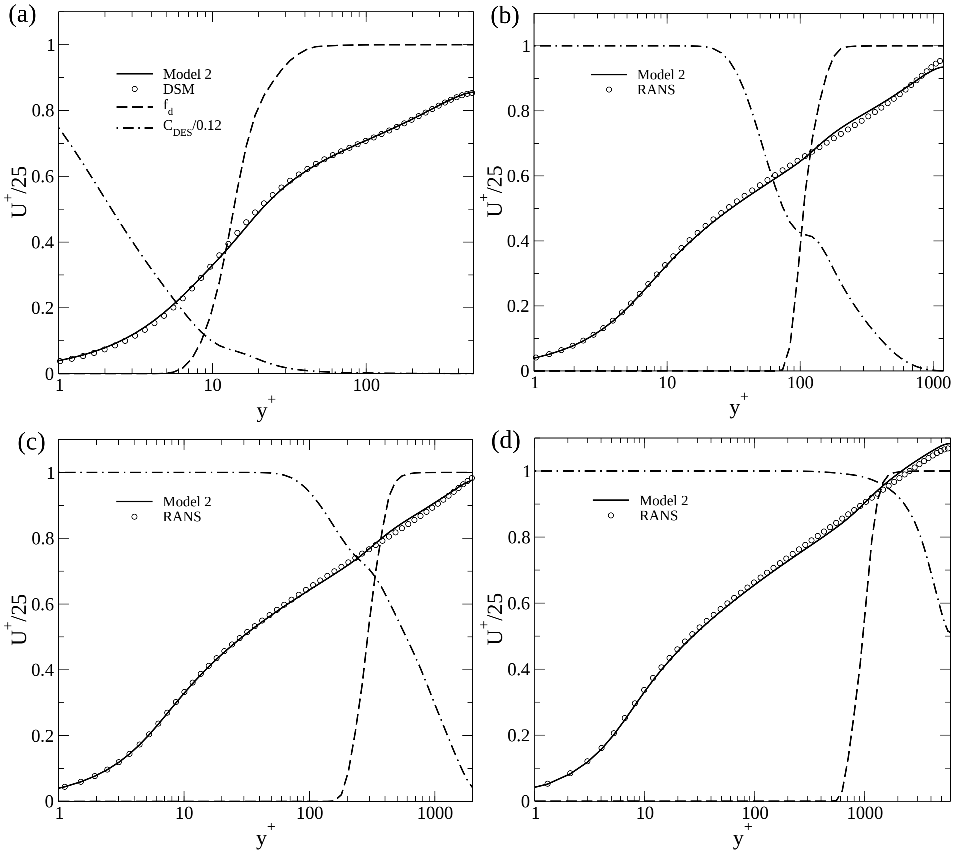

Figure 5.5: U^+ profiles for channel flow at different Re_τ. The dashed curve is f_d and the dash-dot curve is $C_{DES}/0.12$. Circles are RANS (same as DSM-LES). (a) $Re_\tau = 500$, (b) $Re_\tau = 1200$, (c) $Re_\tau = 2000$, (d) $Re_\tau = 6000$

dynamic DDES model more robust, by improving its performance on coarser grids (which are sometimes used in DES simulations). On coarse meshes, the model was shown to perform just like the original DDES formulation with a constant C_{DES} (figure 5.5d), whereas for a fine mesh, the model extended the eddy simulation branch into the near-wall region (figure 5.5a), which improved the accuracy of the computed solution. This can be seen in figure 5.6, which shows profiles of the non-dimensional resolved velocity fluctuations and turbulent kinetic energy. The automatic reduction in the extent of the RANS region on fine meshes also improved the overall performance of the model in cases where the base RANS model is deficient, such as the flow through a rotating channel, as shown in figure 5.7.

A key observation here is the ease with which the dynamic procedure was adapted to the DDES formulation. This is due to the similarity of the original DDES model (in Chapter 2) to

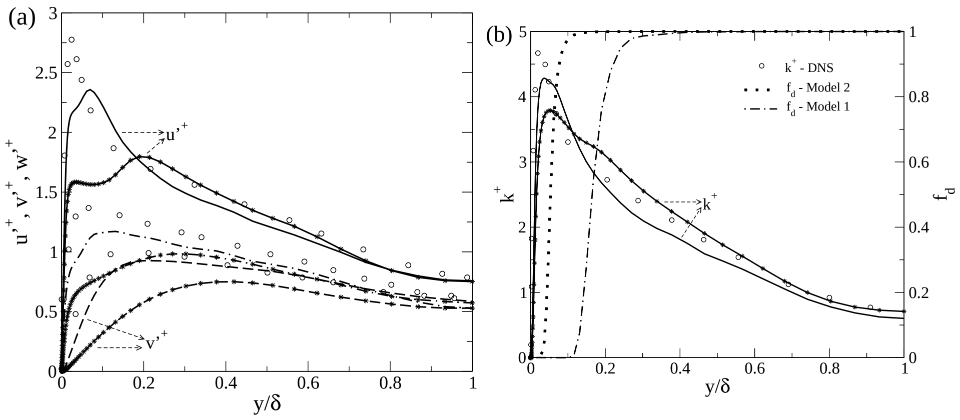

Figure 5.6: Circles - DNS data ($Re_\tau = 590$). Lines with '*' - Model 1, Lines without '*' - Model 2. Model 1 and Model 2 data correspond to $Re_\tau = 500$. (a) Profiles of resolved u'^+, v'^+ and w'^+, (b) Profiles of k^+ and f_d

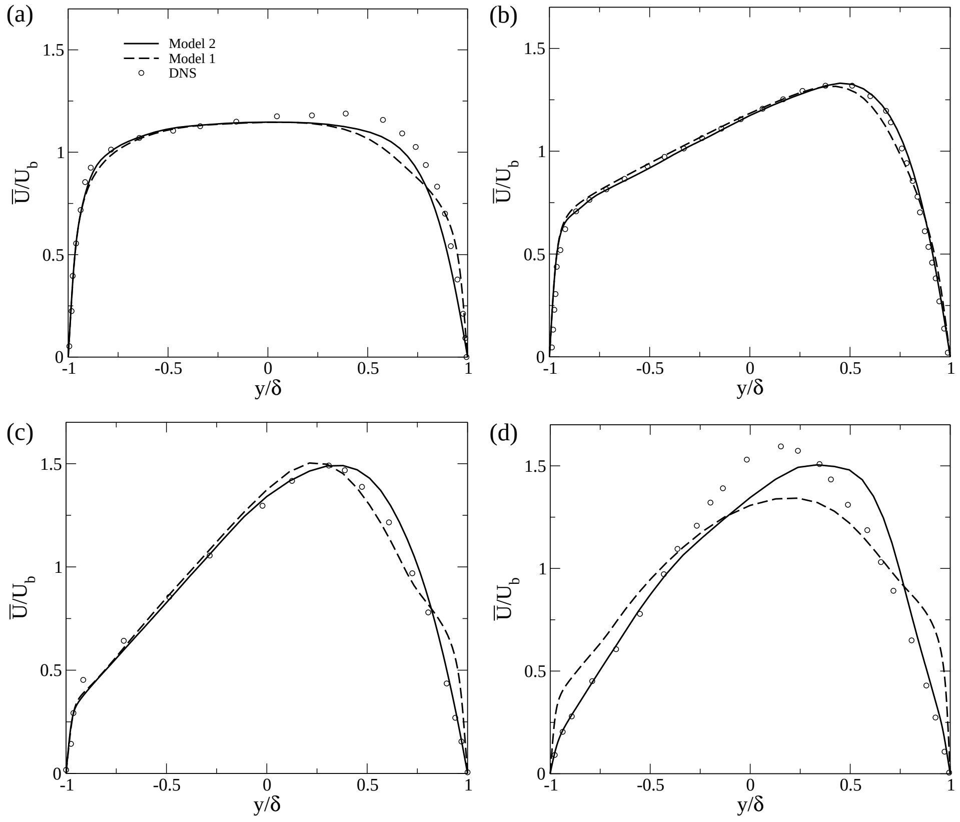

Figure 5.7: Mean velocity profiles normalized with the bulk velocity U_b for rotating channel flow at different Ro. (a) $Ro = 0.1$, (b) $Ro = 0.5$, (c) $Ro = 0.98$, (d) $Ro = 1.5$

the Smagorinsky LES model. Hence it is quite possible that other modifications/improvements made to the Smagorinsky LES model can also be implemented within this DES framework leading to additional robustness.

5.2 Prospects for Future Work

The DDES formulation introduced in Chapter 2, with the dynamic approach described in Chapter 4 was shown to perform well across several flow configurations including attached/separated flows in simple and complex geometries for a range of Reynolds numbers. However, there are several aspects of the model which warrant further research in order to make it applicable to more practical engineering challenges. These research directions could involve any of the following:

- All the cases presented in this dissertation assume an incompressible flow condition, and the model formulation followed this. A natural direction to explore is the reformulation of the model to handle compressible flows, especially high Mach number flows involving shock waves and shock wave - boundary layer interactions. The presence of shock waves would lead to complications related to the numerical scheme as well — the central difference scheme used in the dissertation is known to yield unbounded solutions in the presence of discontinuities. A modification to the base RANS model might also be necessary — Wilcox (2006) suggests using a modified $k - \omega$ RANS model which yields better results for high Mach number flows.

- A similar line of interest is the modeling of chemically reacting flows. Combustion is a tough challenge in turbulence modeling due to the appearance of several higher order terms which need to be modeled to obtain closure. A good starting point for modeling reacting flows using DDES could be to mimic the modeling techniques used in the compressible Smagorinsky LES model for reacting flows.

- Stratified flows can be considered a subset of compressible flows where the density variation occurs only along one direction. The study of such flows is of prime interest since the Earth's atmosphere and oceans would fall under this category, with common applications being climate modeling/weather forecasting and the simulation of ocean currents. Hence extending the applicability of the DDES model to stratified flows is a goal worth pursuing.

- Another, more fundamental, avenue worth exploring lies in the eddy viscosity formulation used. Here, ν_T was redefined to mimic the Smagorinsky subgrid viscosity. It might be possible to define ν_T such that it mimics the subgrid viscosity of a different LES model.
- The Smagorinsky LES model (used in the dissertation) uses implicit filtering, i.e. the grid acts as the filter. This means that for different grids, the computed solution would vary significantly since the filter is also changing. This leads to issues related to grid independence, which is present in the DES formulations (Spalart (2009)). Another approach in LES is the use of an explicit filter, where the grid and the filter are no longer linked. This would lead to a grid independent solution as the mesh is refined, with the subgrid viscosity no longer being a function of the grid spacing. Just like how the Smagorinsky subgrid viscosity was linked to the RANS eddy viscosity, it might be possible to relate the subgrid viscosity obtained using an explicit filter as well, which could potentially lead to a model formulation which exhibits a clear degree of grid convergence.
- A different base RANS model, other than the $k - \omega$ RANS model could also likely be used. However, this might only help if the other RANS model has a better near-wall behaviour than the $k - \omega$ RANS model.

APPENDIX A. DERIVATION OF THE MEAN AND TURBULENT KINETIC ENERGY EQUATIONS

The Mean Kinetic Energy (MKE) equation

The momentum equation describing the instantaneous velocity is

$$\frac{\partial U_i}{\partial t} + \frac{\partial U_i U_j}{\partial x_j} = -\frac{1}{\rho}\frac{\partial P}{\partial x_i} + \nu \frac{\partial^2 U_i}{\partial x_j^2}. \tag{A.1}$$

The corresponding Reynolds-averaged momentum equation is

$$\frac{\partial \overline{U}_i}{\partial t} + \frac{\partial \overline{U}_i \overline{U}_j}{\partial x_j} = -\frac{1}{\rho}\frac{\partial \overline{P}}{\partial x_i} + \nu \frac{\partial^2 \overline{U}_i}{\partial x_j^2} - \frac{\partial \overline{u_i u_j}}{\partial x_j}, \tag{A.2}$$

where the overbar represents the mean quantities. To reiterate, $U_i = \overline{U}_i + u_i$ and $P = \overline{P} + p$, with $\overline{u_i} = \bar{p} = 0$. Multiplying equation (A.2) by $\overline{U}_i$ yields

$$\begin{aligned} \overline{U}_i \frac{\partial \overline{U}_i}{\partial t} + \overline{U}_i \frac{\partial \overline{U}_i \overline{U}_j}{\partial x_j} &= -\frac{\overline{U}_i}{\rho}\frac{\partial \overline{P}}{\partial x_i} + \overline{U}_i \nu \frac{\partial^2 \overline{U}_i}{\partial x_j^2} - \overline{U}_i \frac{\partial \overline{u_i u_j}}{\partial x_j}, \\ \frac{\partial}{\partial t}\left(\frac{1}{2}\overline{U}_i\overline{U}_i\right) + \overline{U}_j \frac{\partial}{\partial x_j}\left(\frac{1}{2}\overline{U}_i\overline{U}_i\right) &= -\frac{1}{\rho}\frac{\partial \overline{U}_i\overline{P}}{\partial x_i} + \nu \frac{\partial^2}{\partial x_j^2}\left(\frac{1}{2}\overline{U}_i\overline{U}_i\right) - \nu \frac{\partial \overline{U}_i}{\partial x_j}\frac{\partial \overline{U}_i}{\partial x_j} - \frac{\partial \overline{U}_i\overline{u_i u_j}}{\partial x_j} + \overline{u_i u_j}\frac{\partial \overline{U}_i}{\partial x_j}, \\ \Rightarrow \frac{\overline{D}K}{Dt} &= \underbrace{\overline{u_i u_j}\frac{\partial \overline{U}_i}{\partial x_j}}_{\text{A}} - \underbrace{\nu \frac{\partial \overline{U}_i}{\partial x_j}\frac{\partial \overline{U}_i}{\partial x_j}}_{\text{B}} + \underbrace{\frac{\partial}{\partial x_j}\left(\nu \frac{\partial K}{\partial x_j} - \frac{\overline{U}_i\overline{P}}{\rho}\delta_{ij} - \overline{U}_i\overline{u_i u_j}\right)}_{\text{C}}, \end{aligned} \tag{A.3}$$

where $K = \frac{1}{2}\overline{U}_i\overline{U}_i$ is the mean kinetic energy.

Term B represents the square of the mean velocity gradient tensor and is always positive. Taking the negative sign in front into account, it represents the dissipation of the mean kinetic energy by molecular viscosity.

Term C is a divergence term, and simply serves to redistribute the MKE without producing or destroying it.

Term A is of prime interest in turbulence, and its significance will be more clear after the equation for the turbulent kinetic energy is derived.

The Turbulent Kinetic Energy (TKE) equation

An equation for the fluctuating velocity component can be derived from the instantaneous and mean momentum equations.

Equation (A.1) - (A.2)

$$
\begin{aligned}
\Rightarrow \frac{\partial u_i}{\partial t} + \frac{\partial}{\partial x_j}(U_i U_j - \bar{U}_i \bar{U}_j) &= -\frac{1}{\rho}\frac{\partial p}{\partial x_i} + \nu \frac{\partial^2 u_i}{\partial x_j^2} + \frac{\partial \overline{u_i u_j}}{\partial x_j}, \\
\frac{\partial u_i}{\partial t} + \frac{\partial}{\partial x_j}(u_i \bar{U}_j + u_j \bar{U}_i + u_i u_j) &= -\frac{1}{\rho}\frac{\partial p}{\partial x_i} + \nu \frac{\partial^2 u_i}{\partial x_j^2} + \frac{\partial \overline{u_i u_j}}{\partial x_j}, \\
\frac{\partial u_i}{\partial t} + \bar{U}_j \frac{\partial u_i}{\partial x_j} + u_j \frac{\partial \bar{U}_i}{\partial x_j} + u_j \frac{\partial u_i}{\partial x_j} &= -\frac{1}{\rho}\frac{\partial p}{\partial x_i} + \nu \frac{\partial^2 u_i}{\partial x_j^2} + \frac{\partial \overline{u_i u_j}}{\partial x_j}.
\end{aligned} \tag{A.4}
$$

Multiplying equation (A.4) by u_i and taking Reynolds average for the entire equation yields

$$
\begin{aligned}
\overline{u_i \frac{\partial u_i}{\partial t}} + \overline{u_i \bar{U}_j \frac{\partial u_i}{\partial x_j}} + \overline{u_i u_j \frac{\partial \bar{U}_i}{\partial x_j}} + \overline{u_i u_j \frac{\partial u_i}{\partial x_j}} &= -\overline{\frac{u_i}{\rho}\frac{\partial p}{\partial x_i}} + \overline{u_i \nu \frac{\partial^2 u_i}{\partial x_j^2}} + \overline{u_i \frac{\partial \overline{u_i u_j}}{\partial x_j}}, \\
\frac{\partial}{\partial t}\left(\frac{1}{2}\overline{u_i u_i}\right) + \bar{U}_j \frac{\partial}{\partial x_j}\left(\frac{1}{2}\overline{u_i u_i}\right) + \overline{u_i u_j}\frac{\partial \bar{U}_i}{\partial x_j} + \frac{\partial}{\partial x_j}\left(\frac{1}{2}\overline{u_i u_i u_j}\right) &= -\frac{1}{\rho}\frac{\partial \overline{u_i p}}{\partial x_i} + \nu \frac{\partial^2}{\partial x_j^2}\left(\frac{1}{2}\overline{u_i u_i}\right) \\
&\quad - \nu \overline{\frac{\partial u_i}{\partial x_j}\frac{\partial u_i}{\partial x_j}} + \bar{u}_i \frac{\partial \overline{u_i u_j}}{\partial x_j}.
\end{aligned}
$$

Substituting $k = \frac{1}{2}\overline{u_i u_i}$ and $\bar{u}_i = 0$, we get the final form of the TKE equation

$$
\frac{\bar{D}k}{Dt} = \underbrace{-\overline{u_i u_j}\frac{\partial \bar{U}_i}{\partial x_j}}_{\text{I}} \underbrace{- \nu \overline{\frac{\partial u_i}{\partial x_j}\frac{\partial u_i}{\partial x_j}}}_{\text{II}} \underbrace{- \frac{\partial}{\partial x_j}\left(\frac{1}{2}\overline{u_i u_i u_j}\right)}_{\text{III}} \underbrace{- \frac{\partial}{\partial x_i}\left(\frac{\overline{u_i p}}{\rho}\right)}_{\text{IV}} + \underbrace{\nu \frac{\partial^2 k}{\partial x_j^2}}_{\text{V}}. \tag{A.5}
$$

We notice that Term A in the MKE equation (A.3) and Term I in the TKE equation (A.5) are both the same, but with opposite sign. Term I is usually positive (taking the negative sign in front into account) and known as the **Production** term. This means that when Term I > 0, then Term A < 0. Hence it represents the transfer of energy from the mean flow to the smaller scales.

Term II: Since this term is the magnitude of the fluctuating velocity gradient tensor, it is always positive. Hence it acts like a sink to k (due to the negative sign in front). It is known as the **Dissipation** term. It represents the conversion of mechanical energy to internal energy (heat) via the dissipation of the small scales by viscosity. It is commonly denoted as ϵ.

Term III: This term neither produces nor dissipates energy. It simply transports energy (since it is a divergence term) and is known as the **Turbulent transport** term.

Term IV: Similar to term III, this is also a divergence term and represents the transport of k by pressure. It is the **Pressure diffusion** term.

Term V: This term acts in a similar manner to the viscous term in the momentum equation and is known as the **Viscous diffusion** term.

In the $k-\omega$ RANS model, the production term is closed by using the Boussinesq approximation, while the viscous diffusion term is already closed. However the dissipation, pressure diffusion and turbulent transport terms all need to be modeled somehow to attain closure. In the RANS formulation, the dissipation term is modeled as a separate term ($C_\mu k\omega$), while the pressure diffusion and turbulent transport terms are combined with the viscous diffusion term (since these 3 terms can be represented as a divergence, and hence, are similar) and modeled using the eddy viscosity and an appropriate constant (the final term on RHS of equation 1.15).

BIBLIOGRAPHY

Arolla, S. K. and Durbin, P. A. (2013). Modeling rotation and curvature effects within scalar eddy viscosity model framework. *International Journal of Heat and Fluid Flow*, 39:78–89.

Batten, P., Goldberg, U., and Chakravarthy, S. (2004). Interfacing statistical turbulence closures with Large-Eddy Simulation. *AIAA Journal*, 42:485–492.

Bell, J. H., Heineck, J. T., Zilliac, G., Mehta, R. D., and Long, K. R. (January 2012). Surface and flow field measurements on the FAITH hill model. In *50th AIAA Aerospace Sciences Meeting including the New Horizons Forum and Aerospace Exposition*, Nashville, TN. AIAA.

Bhushan, S. and Walters, D. K. (2012). A dynamic hybrid Reynolds-averaged Navier StokesLarge eddy simulation modeling framework. *Physics of Fluids (1994-present)*, 24:015103.

Breuer, M., Jovicic, N., and Mazaev, K. (2003). Comparison of DES, RANS and LES for the separated flow around a flat plate at high incidence. *International Journal for Numerical Methods in Fluids*, 41:357–388.

Breuer, M., Peller, N., Rapp, C., and Manhart, M. (2009). Flow over periodic hills - numerical and experimental study in a wide range of Reynolds numbers. *Computers and Fluids*, 38:433–457.

Cherry, E. M., Elkins, C. J., and Eaton, J. K. (2008). Geometric sensitivity of three-dimensional separated flows. *International Journal of Heat and Fluid Flow*, 29:803–811.

de Villiers, E. (2006). *The potential of large eddy simulation for the modeling of wall bounded flows*. PhD thesis, Imperial college of science, technology and medicine.

Deck, S. (2012). Recent improvements in the Zonal Detached Eddy Simulation (ZDES) formulation. *Theoretical and Computational Fluid Dynamics*, 26:523–550.

Esch, T. and Menter, F. R. (October 12-17, 2003). Heat transfer predictions based on two-equation turbulence models with advanced wall treatment. In *International Symposium on Turbulence, Heat and Mass transfer 4*, Antalya, Turkey. ICHMT.

Ferziger, J. H. and Peric, M. (2002). *Computational Methods for Fluid Dynamics*. Springer-Verlag.

Froehlich, J., Mellen, C. P., Rodi, W., Temmerman, L., and Leschziner, M. A. (2005). Highly resolved large-eddy simulation of separated flow in a channel with streamwise periodic constrictions. *Journal of Fluid Mechanics*, 526:19–66.

Germano, M., Piomelli, U., Moin, P., and Cabot, W. H. (1991). A dynamic subgrid-scale eddy viscosity model. *Physics of Fluids A: Fluid Dynamics (1989 - 1993)*, 3:1760–1765.

Greschner, B., Thiele, F., Jacob, M. C., and Casalino, D. (2008). Prediction of sound generated by a rod-airfoil configuration using EASM DES and the generalised lighthill/FW-H analogy. *Computers and Fluids*, 37:402–413.

Gritskevich, M. S., Garbaruk, A. V., Schultze, J., and Menter, F. R. (2012). Development of DDES and IDDES formulations for the $k-\omega$ Shear Stress Transport model. *Flow, Turbulence and Combustion*, 88:431–449.

Grundestam, O., Wallin, S., and Johansson, A. V. (2008). Direct numerical simulations of rotating turbulent channel flow. *Journal of Fluid Mechanics*, 598:177–199.

Hedges, L. S., Travin, A. K., and Spalart, P. R. (2002). Detached-eddy simulations over a simplified landing gear. *Journal of Fluids Engineering*, 124:413–423.

Hunt, J. C. R. (1990). The structure of velocity and pressure fields in turbulent flows over bluff bodies, hills and waves. *Journal of Wind Engineering and Industrial Aerodynamics*, 36:245–253.

Husen, N., Woodiga, S., Liu, T., and Sullivan, J. P. (January 2014). Global luminescent oil-film skin-friction meter generalized to three-dimensional geometry and applied to FAITH hill. In *AIAA SciTech, 52nd Aerospace Sciences Meeting*, National Harbor, MD. AIAA.

Issa, R. I. (1986). Solution of the implicitly discretized fluid flow equations by operator splitting. *Journal of Computational Physics*, 62:40–65.

Jeyapaul, E. (2011). *Turbulent flow separation in three-dimensional asymmetric diffusers*. PhD thesis, Iowa State University.

Jones, W. P. and Launder, B. E. (1972). The prediction of laminarization with a two-equation model of turbulence. *International Journal of Heat and Mass Transfer*, 15:301–314.

Kapadia, S., Roy, S., and Wurtzler, K. (January 6-9, 2003). Detached eddy simulation over a reference Ahmed car model. In *41st Aerospace Sciences Meeting and Exhibit*, Reno, NV. AIAA 2003-0857.

Krishnan, V., Squires, K. D., and Forsythe, J. R. (28 June - 1 July, 2004). Prediction of separated flow characteristics over a hump using RANS and DES. In *2nd AIAA Flow Control Conference*, Portland, OR. AIAA 2004-2224.

Kristoffersen, R. and Andersson, H. I. (1993). Direct simulations of low-Reynolds-number turbulent flow in a rotating channel. *Journal of fluid mechanics*, 256:163–197.

Launder, B. E. and Sharma, B. I. (1974). Application of the energy dissipation model of turbulence to the calculation of flow near a spinning disc. *Letters in Heat and Mass Transfer*, 1:131–138.

Lilly, D. K. (1992). A proposed modification of the Germano subgrid-scale closure method. *Physics of Fluids A*, 4:633–635.

Maddox, S., Squires, K. D., Wurtzler, K. E., and Forsythe, J. R. (2004). Detached-eddy simulation of the ground transportation system. In *McCallen, R. and Browand, F. and Ross, J. (eds.) "The Aerodynamics of Heavy Vehicles: Trucks, Buses, and Trains"*, pages 89–104. Springer, Berlin Heidelberg New York.

Meneveau, C., Lund, T. S., and Cabot, W. H. (1996). A Lagrangian dynamic subgrid-scale model of turbulence. *Journal of Fluid Mechanics*, 319:353–385.

Menter, F. R. (6-9 July, 1993). Zonal two equation k-ω turbulence models for aerodynamic flows. In *24th Fluid Dynamics Conference*, Orlando, FL. AIAA 93-2906.

Menter, F. R. and Egorov, Y. (2010). The scale-adaptive simulation method for unsteady turbulent flow predictions. Part I: Theory and model description. *Flow, Turbulence and Combustion*, 85:113–138.

Menter, F. R. and Kuntz, M. (2002). Adaptation of eddy-viscosity turbulence models to unsteady separated flow behind vehicles. In *McCallen, R. and Browand, F. and Ross, J. (eds.) "The Aerodynamics of Heavy Vehicles: Trucks, Buses, and Trains"*, pages 339–352. Springer, Berlin Heidelberg New York (2004).

Mockett, C., Greschner, B., Knacke, T., Perrin, R., Yan, J., and Thiele, F. (2008). Demonstration of improved DES methods for generic and industrial applications. In *Peng, S. H. and Haase, W. (eds.) "Advances in Hybrid RANS-LES Modelling"*, pages 222–231. Berlin: Springer.

Morton, S. (June 23-26, 2003). High Reynolds number DES simulations of vortex breakdown over a 70 degree delta wing. In *21st Applied Aerodynamics Conference*, Orlando, FL. AIAA 2003-4217.

Moser, R. D., Kim, J., and Mansour, N. N. (1999). Direct numerical simulation of turbulent channel flow up to $Re_\tau = 590$. *Physics of Fluids (1994-present)*, 11:943–945.

Nikitin, N., Nicoud, F., Wasistho, B., Squires, K. D., and Spalart, P. R. (2000). An approach to wall modeling in large-eddy simulations. *Physics of Fluids*, 12:1629–1632.

Nishino, T. and Roberts, G. T. (2008). Absolute and convective instabilities of two-dimensional bluff body wakes in ground effect. *European Journal of Mechanics - B/Fluids*, 27:539–551.

Nishino, T., Roberts, G. T., and Zhang, X. (2008). Unsteady RANS and detached-eddy simulations of flow around a circular cylinder in ground effect. *Journal of Fluids and Structures*, 24:18–33.

Ohlsson, J., Schlatter, P., Fischer, P. F., and Henningson, D. S. (2010). Direct numerical simulation of separated flow in a three-dimensional diffuser. *Journal of Fluid Mechanics*, 650:307–318.

Pack, S. D., Ryon, J. A., Zink, G. A., Dvorak, D. D., and Goeke, J. L. (May 2013). Spray diagnostics of a low NOx air blast atomizer for NASA ERA N+2 program. In 25th *annual conference on liquid atomization and spray systems*, Pittsburgh, PA. ILASS Americas.

Piomelli, U., Balaras, E., Pasinato, H., Squires, K. D., and Spalart, P. R. (2003). The inner-outer layer interface in large-eddy simulations with wall-layer models. *International Journal of Heat and Fluid Flow*, 24:538–550.

Pope, S. B. (2000). *Turbulent Flows*. Cambridge University Press.

Rajamani, B. and Kim, J. (2010). A hybrid-filter approach to turbulence simulation. *Flow, Turbulence and Combustion*, 85:421–441.

Reddy, K. R., Ryon, J. A., and Durbin, P. A. (2014). A DDES model with a Smagorinsky-type eddy viscosity formulation and log-layer mismatch correction. *International Journal of Heat and Fluid Flow*, 50:103–113.

Robinson, D. F., Harris, J. E., and Hassan, H. A. (1995). Unified turbulence closure model for axisymmetric and planar free shear flows. *AIAA Journal*, 33:2324–2331.

Rotta, J. C. (1951). Statistische theorie nichthomogener turbulenz. *Zeitschrift fur Physik*, 129:547–572.

Rotta, J. C. (1968). Über eine methode zur berechnung turbulenter scherströmungen. In *Aerodynamische Versuchsanstalt Göttingen*, Rep. 69 A14.

Roy, C. J., Brown, J. C., DeChant, L. J., and Barone, M. F. (28 June - 1 July, 2004). Unsteady turbulent flow simulations of the base of a generic tractor/trailer. In *34th AIAA Fluid Dynamics Conference and Exhibit*, Portland, OR. AIAA 2004-2255.

Schluter, J. U., Pitsch, H., and Moin, P. (2004). Large Eddy Simulation inflow conditions for coupling with Reynolds-averaged flow solvers. *AIAA Journal*, 42:478–484.

Shur, M. L., Spalart, P. R., Strelets, M. K., and Travin, A. K. (2008). A hybrid RANS-LES approach with delayed-DES and wall-modeled LES capabilities. *International Journal of Heat and Fluid Flow*, 29:1638–1649.

Spalart, P. R. (2000). Strategies for turbulence modelling and simulations. *International journal of Heat and Fluid Flow*, 21:252–263.

Spalart, P. R. (2009). Detached-Eddy Simulation. *Annual Review of Fluid Mechanics*, 41:181–202.

Spalart, P. R. and Allmaras, S. R. (1994). A one-equation turbulence model for aerodynamic flows. *Recherche Aerospatiale*, 1:5–21.

Spalart, P. R., Deck, S., Shur, M. L., Squires, K. D., Strelets, M. K., and Travin, A. K. (2006). A new version of detached-eddy simulation, resistant to ambiguous grid densities. *Theoretical and Computational Fluid Dynamics*, 20:181–195.

Spalart, P. R., Hedges, L., Shur, M., and Travin, A. K. (2003). Simulation of active flow control on a stalled airfoil. *Flow, Turbulence and Combustion*, 71:361–373.

Spalart, P. R., Jou, W. H., Strelets, M. K., and Allmaras, S. R. (Aug 1997). Comments on the feasibility of LES for wings, and on a hybrid RANS/LES approach. In *Proceedings of first AFOSR international conference on DNS/LES*, pages 4–8, Ruston, Louisiana. Greyden Press.

Spalart, P. R. and Squires, K. D. (2004). The status of detached-eddy simulation for bluff bodies. In *McCallen, R. and Browand, F. and Ross, J. (eds.) "The Aerodynamics of Heavy Vehicles: Trucks, Buses, and Trains"*, pages 29–45. Springer, Berlin Heidelberg New York.

Speziale, C. G. (1998). Turbulence modeling for time-dependent RANS and VLES: a review. *AIAA Journal*, 36:173–184.

Speziale, C. G., Abid, R., and Anderson, E. C. (1990). A critical evaluation of two-equation models for near wall turbulence. *AIAA Paper 90-1481*.

Sreenivas, K., Pankajakshan, R., Nichols, D. S., Mitchell, B. C. J., Taylor, L. K., and Whitfield, D. L. (9-12 January, 2006). Aerodynamic simulation of heavy trucks with rotating wheels. In *44th AIAA Aerospace Sciences Meeting and Exhibit*, Reno, NV. AIAA 2006-1394.

Strelets, M. (2001). Detached eddy simulation of massively separated flows. In *39th Aerospace Sciences Meeting and Exhibit*, pages 1–18, Reno, NV. AIAA-2001-0879.

Vogel, J. C. and Eaton, J. K. (1985). Combined heat transfer and fluid dynamic measurements downstream of a backward-facing step. *Journal of Heat and Mass Transfer*, 107:922–929.

Walters, D. K., Bhushan, S., Alam, M. F., and Thompson, D. S. (2013). Investigation of a dynamic hybrid RANS/LES modelling methodology for finite-volume CFD simulations. *Flow, Turbulence and Combustion*, 91:643–667.

Warming, R. F. and Beam, R. M. (1976). Upwind second order differencing schemes and applications in aerodynamic flows. *AIAA Journal*, 14:1241–1249.

Weller, H. G., Tabor, G., Jasak, H., and Fureby, C. (1998). A tensorial approach to computational continuum mechanics using object-oriented techniques. *Computers in Physics*, 12:620–631.

Wilcox, D. C. (1993). *Turbulence Modeling for CFD*. DCW Industries.

Wilcox, D. C. (2006). *Turbulence Modeling for CFD*. DCW Industries.

Zeierman, S. and Wolfshtein, M. (1986). Turbulent time scale for turbulent flow calculations. *AIAA Journal*, 24:1606–1610.